Study on the Nano-structured Materials for Energy Storage System

by

Si Hyoung Oh

A thesis

presented to the University of Waterloo

in fulfillment of the

thesis requirement for the degree of

Doctor of Philosophy

in

Chemistry

Waterloo, Ontario, Canada, 2011

© Si Hyoung Oh 2011

AUTHOR'S DECLARATION

I hereby declare that I am the sole author of this thesis. This is a true copy of the thesis, including any required final revisions, as accepted by my examiners.

I understand that my thesis may be made electronically available to the public.

Si Hyoung Oh

Abstract

The Li-oxygen cell is an emerging energy storage system which has a great promise in the near future for its high energy density and use of free oxygen available from the air. This energy system is attractive since it has nine times higher energy density than conventional lithium-ion cells based on $LiCoO_2$ and graphite. However, this deceptively simple system poses many challenges which must be overcome before it could be considered for any practical application. Firstly, the formation of the insulating and insoluble reaction product, lithium peroxide, requires the highly porous, yet electronically well percolated cathode structure for the reasonable performance. Secondly, the decomposition of lithium peroxide usually involves the huge anodic overpotential which requires the development of highly efficient catalyst. Thirdly, a proper electrolyte system should be developed which is resistant to both the superoxide attack during the discharge reaction and the highly oxidizing environment during the charge process where both oxygen radicals and catalysts are present. Lastly, protection of the lithium anode is necessary, otherwise oxygen radicals in the solvent will react with lithium metal spontaneously, which eventually increases the impedance and more importantly depletes lithium metal from the anode.

This thesis is primarily focused on the development of highly efficient catalysts for oxygen reduction and oxygen evolution reactions for the rechargeable Li-oxygen battery. To this end, a highly porous and electrically networked cathode film was manufactured by utilizing common plasticizers as pore forming agents and a Li-oxygen testing cells were developed using Swagelok® fittings. The Li-oxygen cell test in two different electrolyte systems shows that the reactivity of electrolyte system to superoxide radicals is a key

parameter to determine the nature of reaction product. For LiBOB/PC system, both LIBOB and PC are actively decomposed by superoxide radicals to produce lithium oxalate and lithium carbonate as main discharge products. In the case of $LiPF_6$/TEGDME system, both salt and solvent are stable and thus ideal discharge product, lithium peroxide is obtained. Lead ruthenate and bismuth ruthenate with the extended pyrochlore structure show an excellent catalytic activity by increasing discharge capacity and lowering the anodic overpotential considerably during charge process in both electrolyte systems. They reduce the decomposition of electrolyte system and the extent of carbon corrosion, which accounts for more efficient cycling. The excellent catalytic activity of these pyrochlores originates from their intrinsic oxygen vacancies, electronic conductivity and many surface active sites afforded by its morphology. The performance of this catalyst was further increased through gold deposition on the pyrochlore surface, resulting in much increased discharge capacity. The pyrochlore coated carbon was proposed as a type of catalyst for an efficient way to reduce the amount of catalyst and enhance homogenous mixing with other components. The investigation on the lithium peroxide decomposition mechanism shows that carbon corrosion which occurs at around 4.0 V by lithium peroxide makes further decomposition difficult without a catalyst. In the presence of catalyst, almost full decomposition of lithium peroxide occurs with a lowered decomposition potential even though carbon corrosion still occurs. This gives a hint that the generation of a nano-porous structure and the homogenous distribution of catalyst over these pores are very important, as well as use of a highly efficient catalyst for lowering activation overpotentials. In conclusion, although there are still many obstacles present, as listed above, for the commercial application of Li-oxygen

cell, these hurdles are surmountable in the near future by intensive research and the results shown in this thesis can be a cornerstone for further research.

Supercapacitors based on metal oxide are new energy storage devices for ultrafast charging and discharging with decent energy density over hundreds of thousands of cycles for many commercial electronic devices and power tools. The surface redox nature of these reactions requires the creation of high surface area for better utilization and performance. Hydrous ruthenium dioxide is one of the most attractive supercapacitor materials owing to its high pseudo-capacitance and metallic character, which facilitate fast electron movement. In this thesis, a simple process involving soft liquid crystal templating using cationic surfactant and gentle heat-treatment in the mild temperature was developed to prepare mesoporous ruthenium oxide with a quasi-crystalline wall character, which has a high surface area and controlled water contents in the structure. The electrochemical testing results exhibited a promising performance of high gravimetric capacitance and a good rate capability facilitated by high surface area as well as porous structure.

Acknowledgements

I would like to express my deepest gratitude to my supervisor Professor Linda F. Nazar. I cannot thank her enough. Her tireless passion and absolute devotion to science has inspired me a lot all the way through my entire graduate years. It was because of her that I became aware of all the scientific logic and scientific communication skills. With her guidance, supports and encouragements I could make my way through the difficult times.

I would like to thank my Ph.D. advisory committee members, Professor Holger Kleinke, Professor Pavle Radovanovic, and Professor Jacek Lipkowski from University of Guelph for their instructive and valuable advice on my research during my study. I also would like to express my gratitude to Professor Viola Birss from University of Calgary, Professor Eric Prouzet, and Professor Zhongwei Chen for serving on my defense committee.

I would like to extend my sincere thanks to all former and current lab members for their invaluable help and priceless collaboration during my graduate years. I am deeply indebted to all Li-air cell group members for my successful completion of PhD degree. I would like to thank Dr. Neil Coombs in University of Toronto for his TEM work.

Finally, I would like to say very special thanks to my family… my wife, my son, my daughter and my Mom & Dad for their unconditional love, supports and encouragements. Without you, nothing would have been possible.

Si Hyoung Oh, 2011

Table of Contents

List of Figures

List of Tables

I. Introduction

1.1 Renewable energy sources and energy storage problems

As the end of the fossil fuel era is nearing, the search for alternative energy sources has attracted worldwide attention for decades. The invention of the first commercial steam engine by Thomas Newcomen in 1712 [1] sparkled a fossil-fuel-based economy for the last several centuries, eventually catalyzing ever-increasing consumption and depletion of fossil fuels available from all over the world. As one grave consequence, the accumulation of the greenhouse gas in the atmosphere from the burning of fossil fuel for centuries not only has given rise to local climate change, which disturbs subtle ecological balance and threatens the survival of endangered species, but has sometimes brought catastrophic natural disasters like flood, drought and heat waves around the globe [2]. The early melting of ice platforms in Western Hudson Bay in springtime, from which polar bears hunt seals, has put them in malnutrition and starvation before they store enough fat reserve to survive the period of scare food from late summer to early fall [3]. As a consequence, the subpopulation of bears in this area shows a significant decline recently [4].

Realizing the huge impact of energy resources on the environment, and thus, the future of earth, people now turn to search for renewable and sustainable energy sources like wind power, solar energy, geothermal energy, hydropower, biomass and bio-fuel, and nuclear powers. Along with increasing concerns over the environment, a strong government support and intensified international regulations on environment and greenhouse gas emission like Kyoto protocol (1997) have further driven the technological development and

commercial applications of the renewable energy powers. During the last decade, the worldwide renewable energy capacity increased at an enormous rate annually, and it is predicted that the growth of renewable energy market will be further accelerated in the future.

Wind power uses wind energy to propel turbines to generate electricity. The earth is unevenly heated by the Sun (i.e. between poles and equator or day and night) and the difference in heat capacity between land and sea, along with uneven heating, causes global atmospheric convection in troposphere. Large scale wind power plants are being built in high hills and off shores around the world, where the strong wind blows constantly through the year [5]. Many elaborate probabilistic models are employed for the precise evaluation of the frequency and the direction of the wind at the candidate site [6]. Wind power is a clean, renewable energy source and produces no greenhouse gas emissions during operation. Small scale wind power stations are ideal for providing electricity to the isolated areas while large scale plants are connected to the commercial power grid. However, intermittency of wind generates some problems with electricity storage when it is considered for large scale power generation. Also, a good selection of site is critical for the economic aspect to compensate the large initial installment cost [7].

Solar power systems convert sunlight into electricity directly by photovoltaic cells or indirectly through concentrated solar powers (CSP) system [8]. In photovoltaic cells, sunlight is converted into electric current by photovoltaic effect using semiconductors like varied types of silicon (monocrystalline, polycrystalline, amorphous), CdTe, GaAs, copper indium gallium selenide (CIGS) and so on [9], where electrons in valence band are excited into the conduction band generating electric potential upon irradiation [10]. This is considered as the reverse process which occurs in light emitting diode (LED). Currently,

there are many photovoltaic power plants under commercial operation, including the world's largest Sarnia photovoltaic power plant near Sania, Ontario. CSP systems utilize lens or mirrors and tracking system to focus a wide area of sunlight into a concentrated beam to create heat, which can drive heat engines and thus generates electricity [11]. The common beam concentration technologies include parabolic trough, dish stirlings, concentrating linear fresnel reflector and solar power tower. Although solar power generates virtually no pollution and no fuel cost, a critical problem with this power sources is still the high initial installment cost.

Geothermal power systems utilize the thermal energy from the underground, where temperature increases by 25 - 30 ^{o}C per km depth in most of world away from the tectonic plate boundaries [12]. It is believed that the origin of the heat flow from underground is mostly due to the decay of natural radioisotopes such as U^{238}, U^{235}, Th^{232} and K^{40} within mantles, and minor residual heat from planetary accretion. In the typical binary cycle power station, the hot water from underground delivers heat to the secondary loop where a low boiling point fluid vaporizes to drive the turbine [13]. Although geothermal energy requires no fuel, construction (drilling) is very costly and there are environmental issues related with toxic gases and chemicals like CO_2 [14], H_2S, CH_4, Hg, As and Sb [15] from underground.

Nuclear power utilizes the energy released when heavier nucleus like U^{235}, Pu^{239} splits into lighter nuclei by interaction with thermal neutrons (nuclear fission) or lighter nuclei like D^2, T^3 join together to create single heavier nucleus (nuclear fusion) in such device like tokamak [16]. This occurs as the sum of nuclear binding energy from the mass defect of the resultant nuclei is larger than the original nucleus (nuclei). As Fe^{56} has the maximum binding energy per nucleon, a heavier nucleus than Fe^{56} can produce energy by

nuclear fission, and lighter nuclei joins together to generate energy by nuclear fusion. As the magnitude of nuclear binding energy is many orders larger than the chemical binding energy, the energy released from these nuclear reactions is much larger (~200 MeV per fission of U^{235}). Natural nuclear fusion process powers all active stars in the sky [17]. A dwarf star in main sequence like Sun delivers its energy by forming one alpha particle from joining four protons releasing two positrons and two neutrinos while a massive red supergiant star like Betelgeuse (α Ori.), which is almost in the final stage of its life, generates heat from the creation of heavier nucleus, where its internal core has already exhausted hydrogen fuel and starts to fuse heavier elements. The core of Betelgeuse will end up with iron because it cannot form heavier atoms than iron while still producing heat. However, the realization of nuclear fusion power on earth (thus creation of artificial sun) is yet far from being any practical consideration although vigorous research projects are under way around the world like ITER, KSTAR. The huge activation energy barrier exists from the repulsive electrostatic interactions [18] between nuclei before they approach close enough for an attractive (short-ranged) nuclear strong force to bind them together and thus at least 120 million Kevin is needed to overcome the coulombic activation for simple deuterium-tritium process (in reality, however, much less temperature is required due to quantum mechanical effect).

On the other hand, nuclear fission technology has been well developed for the last half century, and many nuclear power plants are already in commercial operation around the world. However, the use of nuclear energy as an alternative energy source of the future is under firing debates due to concerns over its environmental effect, safety issues (Three Mile Island (1979), Chernobyl (1986), Fukushima (2011) accidents) as well as nuclear proliferation. Most of nuclear reactors use U^{235} as a fuel, which has a high fission cross-

section with thermal neutrons and generates many prompt neutrons upon disintegration (2.6 per fission) for sustaining chain reaction [19]. However, U^{235} exists only 0.72 % among several uranium isotopes in nature, and an excessive consumption of which may result in the early depletion of uranium sources even before oil. As the nuclear spent fuel radiates high radioactivity and needs to be isolated for hundreds of thousands of years from the general public, the exact economic and safety evaluation over such a long period is actually beyond any kind of prediction. The spent nuclear fuel also contains about 1 % Pu^{239} which is transmuted from U^{238} through neutron absorption and subsequent two β^- decays. Therefore a strict monitoring on the transportation and storage of spent fuel is essential for the nuclear non-proliferation by international organization.

In many power stations using renewable energy sources, especially in solar energy and wind power, the intermittency of power source is one of key obstacles for the large-scale production. The produced energy should be stored in the storage device or transmitted to the place where it is needed. One of the popular conventional methods is heating molten salt up to high temperature where conventional heat engine can be used to generate electricity on demand [20]. Molten salt is ideal as it is cheap but has a high heat capacity to hold the heat for long. However, the recent dramatic advance in battery and supercapacitor technologies make it possible for these chemical storage devices to be applied, even for a large-scale storage of electricity from intermittent energy sources. Furthermore, the environmental concerns over greenhouse gas emission from fossil-fuel-based transportation methods lead to the development and the commercialization of the hybrid electric vehicle (HEV) and electric vehicle (EV) where rechargeable energy storage system with high energy density and high power plays a key role. The recent advance in Li-ion battery and supercapacitor technology

is mainly contributed by the development of new novel energy storage materials and application of nano-technology to the existing materials [21-23].

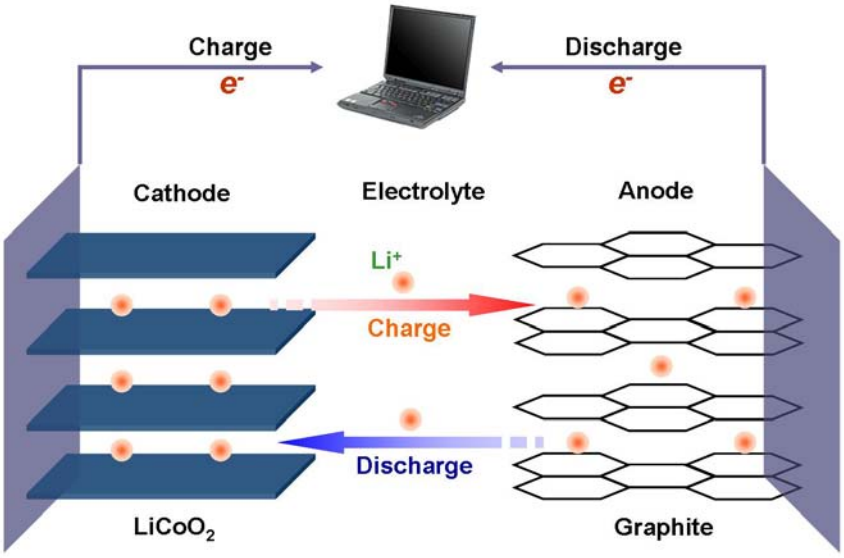

Figure 1.1 Schematic for charge and discharge processes in a commercial Li-ion battery with $LiCoO_2$ as cathode and graphite as an anode. Li ion moves back and forth upon charge discharge resulting in the oxidation or reduction of electrodes**.**

Li-ion batteries came into the commercial market firstly by Sony Co. in 1991, where they employed two layered intercalation compounds, $LiCoO_2$ with rock salt structure [24,25] as cathode and graphite as anode material, and Li ions move back and forth between two electrodes upon charge and discharge to create high voltage of 3.7 V (**Figure 1.1**). The use of graphite on anode effectively resolved the inherent safety problem related with lithium metal anode [26,27]. They quickly conquered portable electronic consumer's market as dominant power sources for commercial electronics such as cellular phones, digital cameras, camcorders and laptop computers because their high energy density makes the battery pack lighter and smaller. However, the advent of HEV and EV, as well as backup storage for renewable energy power stations, like solar cell and wind power, require more advanced

battery systems. These should meet a variety of specific requirements in terms of energy density, power level, safety and cost, leading to the intensive research searching for advanced cathode and anode materials.

As a more advanced cathode, spinel $LiMn_2O_4$ has attracted an immediate attention because of its substantially lower material cost and improved safety with a high plateau voltage of 4.1 V while the spinel structure allows three dimensional diffusion of lithium ions [28,29]. However, it has turned out that this material is subject to fading in long-term cycling, especially at elevated temperature [30,31]. These materials also suffer from a low rate capability due to its intrinsic low electrical conductivity. The layered transition metal oxides such as $LiNi_{1/2}Mn_{1/2}O_2$ [32,33] and $LiNi_{1/3}Co_{1/3}Mn_{1/3}$ [34,35] enjoy higher discharge capacities as the full utilization of oxidation / reduction of nickel component from Ni^{2+} to Ni^{4+} is possible while maintaining layered structure. However, the preparation of reliable mixed transition metal co-hydroxide for mass production adds additional material cost, and the cation mixing between lithium and transition metal sites as well as the formation of nickel oxide on the surface lead to the impedance increase and eventual capacity fading. The high-voltage spinel $LiNi_{0.5}Mn_{1.5}O_4$ [36,37] has a higher operating voltage about 4.7 V vs. Li/Li^+, which means higher energy density and potentially higher power level. But, it actually exhibits lower rate capability as $LiMn_2O_4$ does, and furthermore, the development of reliable electrolyte system in the high potential needs to be solved beforehand. In the meantime, the cathode materials based on the polyanionic group such as phosphate [38-42], fluorophosphates [43-45], silicates [46,47], fluorosulfate [48,49] with mineral olivine or tavorite structure were proposed as candidates of promising cathode materials. The cathode material $LiMPO_4$ (M = Fe, Mn, Co) with olivine structure gained little attention when it was

first published in 1997 [38,39] because of its intrinsic insulating electrical conductivity and one dimensional lithium diffusion path, although it exhibited much improved safety characteristics compared with conventional transition metal oxides. However, soon it was discovered that the fabrication of nano-sized particles and the formation of electronically well percolated network around the particle such as nano-sized carbon coating can dramatically improve the performance of this material [40-42]. Ironically, its superb high rate capability enables this material to be considered for power sources like power tools, HEV and EV. However, the increased material processing cost and low tap density inherent in nano-sized material are major downsides.

For the advanced anodes, many studies have focused on developing high capacity material exceeding the capacity of graphite (372 mAh/g) while maintaining relatively low potential against Li/Li^+ and good cycleability. Materials like silicon, tin, germanium and aluminum can form series of lithium-rich phases electrochemically upon contact with lithium ions at low potential [50-52]. In the case of silicon, the lithium-richest phase is $Li_{22}Si_5$, where the theoretical capacity from this compound amounts to as much as 4200 mAh/g. It is well known however, that a large amount of lithium insertion/de-insertion into/out of these alloying hosts accompanies a huge volumetric change (~ several hundred percent) raising an immense mechanical stress and strain [53,54]. The repeated cycling eventually results in the pulverization of original particles and loss of electrical contact causing a significant impedance growth and low utilization. To relieve these problems, many studies focus on the control of geometrical structure such as formation of nano-sized particle, thin film [55], nano-pillar structure [56] to provide as much free surface as possible to release the stress. Another useful approach is alloying the host material with transition

metals to provide a buffering region for the volume expansion and limit the amount of lithium to be inserted into [57-60]. Still another approach was made by embedding the nano-sized host in the conductive matrix like carbon, where conductive matrix facilitates electron conduction as well as relieves the stress caused by volume expansion and contraction of hosting material [61-64].

Some transition metal oxides such as CoO, NiO, FeO and Cu_2O can undergo electrochemical conversion reaction with lithium ions into its elemental form and lithium oxide (Li_2O) at low potential when it is prepared as nano-particle form, which exhibits a high capacity around 700 mAh/g [65]. Similar conversion reactions occur in many other transition metal compounds like metal fluorides, phosphides, sulfides nitrides and phosphates and many studies have been done for possible applications as anode materials for Li-ion battery. However, despite the relatively high gravimetric capacity of theses materials, the high electrochemical overpotentials, which are intrinsic to conversion reactions should be overcome before any practical application can be realized.

The energy storage device which allows extremely fast charging or discharging and which is not achievable by conventional battery systems is necessary in a variety of situations in lots of commercial applications. For example, the acceleration in the hybrid electric vehicle (HEV), emergency power supply like uninterruptible power sources (UPS), the flashlight of digital camera, motor startup for large-size engines and power tools like electric saw or drill requires a large amount of energy to be discharged in a short period of time i.e. even within a few seconds. On the other hand, the energy storage for the regenerative braking system in HEV, power sources for electric vehicles and power tools requires a quick recharging of the battery. The ideal energy storage device developed for

these purposes is a supercapacitor, where it usually works with high capacity battery system to cope with instant peak power demand from the electronics. The recent remarkable advance in supercapacitor technologies in the electric double layer capacitors (EDLC, **Figure 1.2**) [66-70] and metal oxide pseudocapacitors [71,72] not only enables the sufficient power levels to deal with instant peak power surge, but allows these to be considered as an alternative energy storage device for replacing conventional battery system [73].

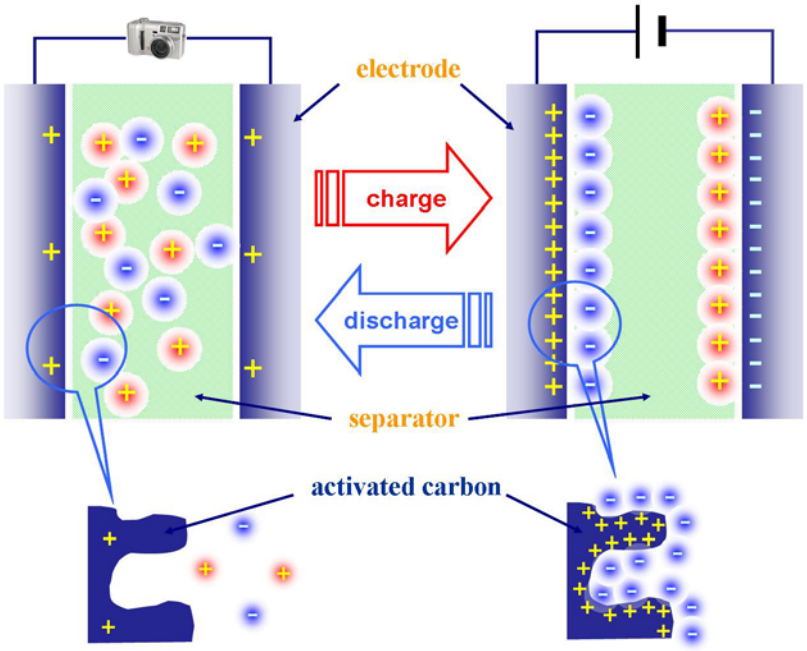

Figure 1.2 Schematic for EDLC with high-surface-area activated carbon. The surface charge stored in electrical double layers enables ultra-fast charging/discharging.

1.2 Introduction to Li-oxygen cell

The rust on the surface of iron-based alloy is usually a consequence of atmospheric corrosion triggered by oxygen attack from the humid air over a long period of time (**Figure**

1.3a) [74]. Oxygen gas is generally a very strong oxidizing agent due to its high electronegativity (3.44 in Pauling scale) [75,76] so that most of metallic species in the water are not stable under the presence of dissolved oxygen [74]. However, the very early attack to the pristine metal surface develops a very thin passive oxide layer, and it is this film which hinders further degradation of the surface by delaying oxygen diffusion through the film and diminishing the direct contact of intact surface with water. The intentional film by elaborate anodic polarization is sometimes useful tool to prevent further oxidation for some metals [74].

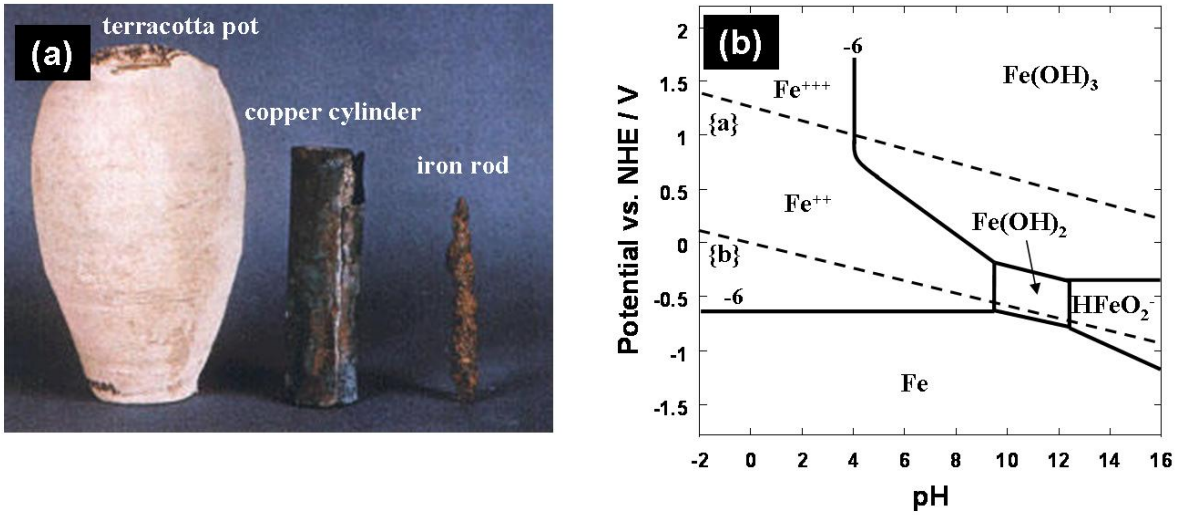

Figure 1.3 (a) Baghdad 'battery', disputable 'first' battery manufactured in the early centuries AD discovered in Iraq[77] and (b) simplified Pourbaix diagram for iron.[74] Iron is not stable in contact with water, especially under the presence of dissolved oxygen. The long exposure to the humid air for thousands of years leads to the thick rust on iron rod as well as patina on copper cylinder of the ancient artifact.

The Pourbaix diagram [78] generally provides a comprehensive guideline to predict how metallic species will behave in the caustic solution with different pH and variant oxidizing (potential) conditions (**Figure 1.3b**). This corrosion phenomenon, together with related environmentally assisted cracking (EAC), is notorious for the huge economic loss every year

in many piping and sewage systems around the world [79-81]. This corrosion phenomenon is basically a redox chemical process [74] where two electrochemically active species with different reduction potentials are in contact with each other through the electrolyte, and it is thermodynamically favorable as Gibbs free energy of formation, ΔG^o of resultant metal oxide or hydroxide is much lower (larger negative value) than the summation of its components i.e. metal and oxygen [82]. The early observers of this 'bad' but valuable effect also found a useful application of this thermodynamic energy, ΔG by dividing overall reactions into two separate electrochemical half cell reactions and arrange them to occur in two different places; i.e. cathode and anode in a well controlled manner to create the electromotive force, E between two electrodes [83].

$$\Delta G = - \ nFE \qquad (1\text{-}1)$$

This led to the development of a lot of metal-air energy storage systems like zinc-air [84,85], iron-air and aluminum-air cells [86,87]. These energy systems are usually composed of an active metal anode where oxidation of metal is readily occurring, and a high surface-area carbon cathode where oxygen gas is reduced to hydroxide ions by a catalyst in mostly alkaline electrolyte media. The oxygen reduction kinetics is generally much better in the alkaline solution [85,88]. The schematic zinc-air cell configuration is described in **Figure 1.4**, which shows porous carbon membrane cathode, zinc metal anode, and an aqueous KOH electrolyte system. Simplified electrode reactions possibly occurring at cathode and anode of metal-air cells are described in **Reaction 1-2** ~ **1-6**.

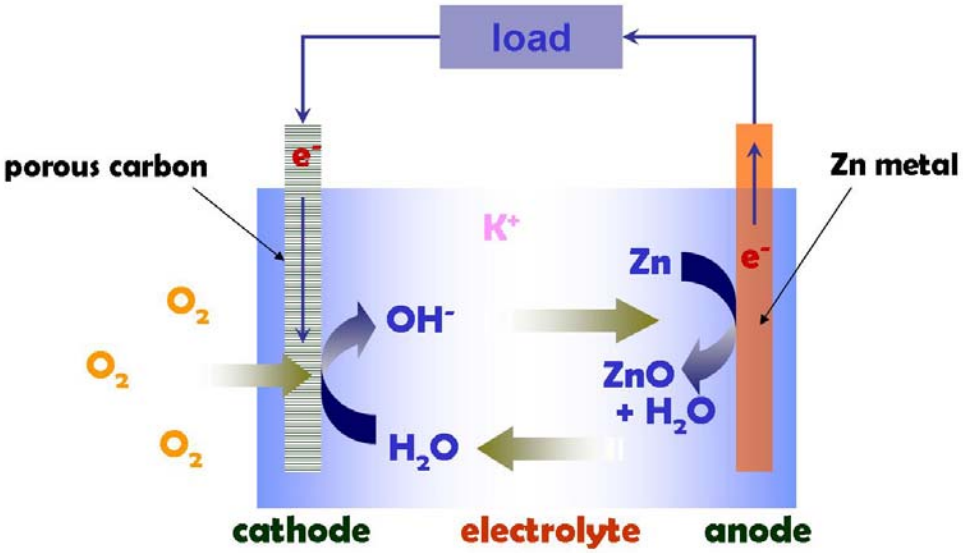

Figure 1.4 Schematic of Zn-air cell reactions with porous carbon cathode, zinc metal anode and alkaline electrolyte solution.

cathodic reaction: $O_2 + 2H_2O + 4e^- \rightarrow 4OH^-$ (1-2)

anodic reaction: $M + zOH^- \rightarrow M(OH)_z + ze^-$ *or* (1-3)

$$M + zOH^- \rightarrow MO_{z/2} + (z/2)H_2O + ze^- \quad (1\text{-}4)$$

overall reaction: $zO_2 + 4M + 2zH_2O \rightarrow 4M(OH)_z$ *or* (1-5)

$$zO_2 + 4M \rightarrow 4MO_{z/2} \quad (1\text{-}6)$$

During the discharge process, the hydroxide ions diffuse to the anode to form metal hydroxide or oxide while electrons flow in the external circuit to provide useful energy. In practice, the reduction of oxygen on the cathode is not so kinetically favorable, even at 200 ^oC, so it requires the presence of a catalyst [88]. The direct reduction of oxygen into hydroxide ions involve four electrons at the same time, and without a catalyst, it can occur only at the expense of huge cathodic overpotential. The introduction of some catalyst involves the formation of peroxide as an intermediate species and it lowers the activation

energy related with reduction of oxygen markedly. The past research on this area focused on either the identification of the detailed reduction mechanism of various catalysts or the development of new cheap yet efficient catalysts for this reaction, other than the conventional expensive precious metals like platinum, gold and iridium. In addition, in many cases, the existence of some parasitic reactions, i.e. hydrogen evolution on the anode which results in self-discharge, causes mixed potential problems [87]. The cell never reaches theoretical voltage. Nonetheless, despite these problems, metal-air cell has huge advantages over other battery systems in terms of economical and energy density aspects because the cathode 'active' material is provided freely and without any limit from the ambient atmosphere increasing overall energy density based on the initial weight considerably. Providing the anode metal continuously, these systems can be considered as another type of fuel cell [85]. The use of light alkali or alkaline earth metallic species with low reduction potential like lithium, sodium, magnesium as anode material is attractive because these materials can generate higher operating voltage in theory, i.e. higher power, as well as higher gravimetric capacity compared with transition metal anodes [89-91]. However, it always comes with the problem of developing a new electrolyte system, which has a wider voltage window and better stability against metallic anodes than conventional aqueous systems and is free from other detrimental side reactions.

In 1996, K. M Abraham et al. [92] conveniently overcame this problem by simply replacing the conventional 'reactive' aqueous electrolyte with a well-developed lithium battery electrolyte and reported the first working Li-air (oxygen) cell (**Figure 1.5**). They used a plasticized polymer electrolyte based on $LiPF_6$ in polyacrylonitrile (PAN) with ethylene carbonate and propylene carbonate (plasticizers). For this system, contrary to

conventional metal-air system based on aqueous electrolyte where the diffusion from cathode to anode of hydroxide ion is greatly facilitated by water, the transference number of metal cation (Li^+) in Li-oxygen cell is close to unity (= 1), which means mostly cation carries charges from anode to cathode. The reaction product precipitated on the cathode side was identified as lithium peroxide by RAMAN spectroscopy [92-94]. Therefore the half cell and the overall reactions involved with this cell can be written as follows.

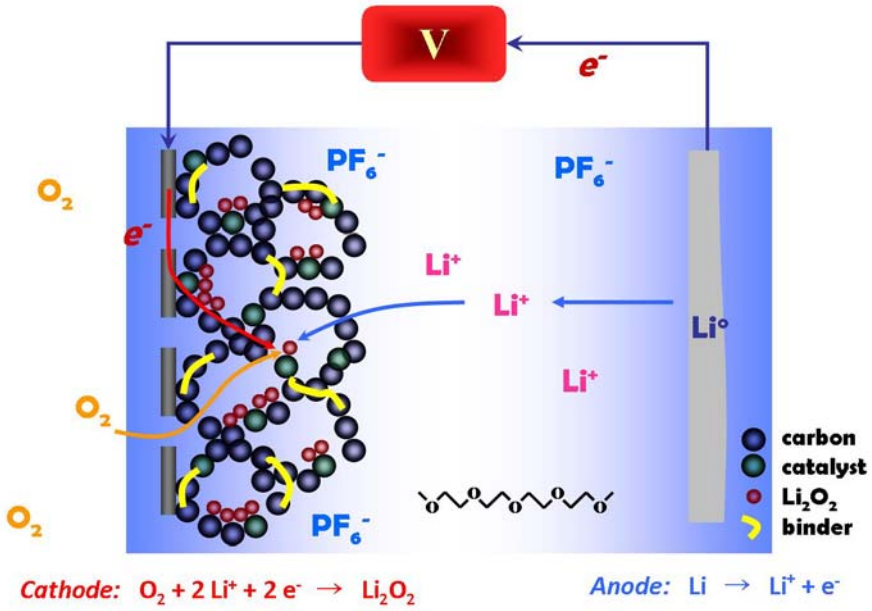

Figure 1.5 Schematic of Li-oxygen battery. Cathode is made up of porous carbon to accommodate reaction product and catalyst to lower the overpotential.

cathodic reaction: $O_2 + 2Li^+ + 2e^- \rightarrow Li_2O_2$ (1-7)

anodic reaction: $2Li \rightarrow 2Li^+ + 2e^-$ (1-8)

overall reaction: $O_2 + 2Li \rightarrow Li_2O_2$ ΔG^o = -570.954 kJ/mol [95] (1-9)

The standard electrode potential calculated from the change in the standard Gibbs free energy of formation from the overall reaction is 2.959 V. From a theoretical point of view,

several other discharge products like lithium oxide (Li_2O) or lithium superoxide (LiO_2) may exist at the same time as the following two reactions are also plausible with similar standard electrode potentials [92,95].

$$O_2 + 4Li \rightarrow 2Li_2O \qquad \Delta G^o = -562.102 \text{ kJ/mol} \qquad E^o = 2.913 \text{ V} \qquad (1\text{-}10)$$

$$O_2 + Li \rightarrow LiO_2 \qquad \Delta G^o = -292.88 \text{ kJ/mol} \qquad E^o = 3.035 \text{ V} \qquad (1\text{-}11)$$

These reactions suggest several important factors in designing high-performance Li-air cell electrodes, especially in the construction of the cathode. The cathodic reaction shows that three phases (gas, liquid, solid) are involved in the reaction as reactants or products. The porous carbon structure is required to accommodate the insoluble reaction products on the cathodic side as well as to facilitate oxygen diffusion to the reaction site through the cathode film. The accumulation and pore congestion by the reaction product may result in retardation in diffusion of oxygen and lithium ions to the reaction site, which can generate a significant activation and concentration polarization at the end stage of the discharge reaction [93,96]. In addition, this porous carbon network should be well percolated enough to provide electrons to the reaction site smoothly to lower the overall impedance. The homogenous distribution of nano-sized catalyst is also required to maximize the performance. These requirements for cathode design pose major engineering challenges. The existence of catalyst is important especially when a rechargeable cell is considered as it plays an important role in lowering the activation overpotential for charge process [97,98]. Many catalysts including the ones used in other metal-air systems were adopted and applied for these purposes [99,100]. The mechanistic details concerning the reduction of oxygen on the

glassy carbon surface in organic solvent were investigated with tetrabutylammonium (TBA) salt like $TBAPF_6$ and $TBAClO_4$ using cyclic voltammetry and rotating disc electrode techniques [88,101]. These studies suggest that the initial form of oxygen reduction is superoxide (O_2^-), and then this superoxide is further reduced to peroxide (O_2^{2-}) with each reaction following a one-electron electrochemical process.

$$O_2 + TBA^+ + e^- \rightarrow TBAO_2 \quad (1\text{-}12)$$

$$TBAO_2 + TBA^+ + e^- \rightarrow TBA_2O_2 \quad (1\text{-}13)$$

In the above reactions, superoxide form, $TBAO_2$ is soluble in most electrolyte systems and it is thermodynamically stable. It can be reversibly decomposed back to TBA ions and oxygen molecules through a one electron process. On the other hand, when superoxide is further reduced to peroxide (**Reaction 1-13**), the peroxide decomposition reaction is possible only at the expense of high anodic polarization, which means reaction involved in **Reaction 1-13** is quite irreversible. When the cation is replaced by lithium ions in similar study, they observed that lithium superoxide is formed initially in a similar manner (**Reaction 1-14**) [102,103]. However, lithium superoxide (LiO_2) is not thermodynamically stable so that it readily decomposes to lithium peroxide either by one-electron electrochemical process (**Reaction 1-15**) or chemical route (**Reaction 1-16**).

$$O_2 + Li^+ + e^- \rightarrow 2LiO_2 \quad (1\text{-}14)$$

$$LiO_2 + Li^+ + e^- \rightarrow Li_2O_2 \quad (1\text{-}15)$$

$$2LiO_2 \rightarrow Li_2O_2 + O_2 \quad (1\text{-}16)$$

The backward reaction involves the decomposition of lithium peroxide and thus, is quite irreversible. However, they claimed [102] that although the reduction of oxygen in the presence of lithium ions (**Reaction 1-15, 16**) is irreversible, the electrolyte property such as the solvent donor number (DN) influences on the 'degree' of irreversibility by forming a quasi-stable Li ion-solvent complex. This Li ion-solvent complex behaves more or less like a Lewis soft-acid and it is easy to combine with superoxide ion which is a Lewis soft-base among reduced species. The stability of Li-solvent complex superoxide depends on the strength of the bond between lithium ion and solvent. The more stable are these superoxide species, the more reversible the reduction reactions become.

On the anode side, the oxidation and reduction reaction of lithium proceeds quite reversibly being different from the conventional metal/air system where metal oxide or hydroxide is quite reluctant to get reduced back to metallic state upon charge [104]. However, oxygen from the atmosphere or partially reduced oxygen radicals (i.e. superoxide radicals) may diffuse to anode and directly react with lithium metal to form a thick film of electrically insulating lithium oxide unless it is properly protected. This may lead to development of huge impedance as well as mixed potential problems on the anode especially in long-term experiments. In addition, as the amount of metallic lithium available from the anode is continuously decreased, the capacity fading is inevitable after several cycles. In case it is considered for a rechargeable cell, the inherent dendrite formation on the surface during the charge process raises safety concerns just like in other forms of Li-ion cells where metallic lithium is used on the anode side [26,27]. Besides, a high surface area of the dendritic structure is more susceptible to the attack from active oxygen species. Several

studies are focused on the protection of lithium anode by sealing with water-stable Li-ion conducting membrane (LISICON) in alkaline [105-108] and neutral [109,110] aqueous solution. In this case, the lithium anode is completely isolated from the surrounding water and dissolved oxygen acts as a 'fuel'. The whole system can be regarded as semi-fuel cell because in principle, the reaction can proceed until all lithium is consumed from the anode.

The oxygen solubility and diffusivity in the electrolyte solvent were intensively studied by J. Reed et al. [111,112] as these two parameters are undoubtedly important for the cell performance, especially in terms of discharge rate capability. Recently, the stability of the electrolyte system, especially when a solvent based on organic cyclic carbonate like propylene carbonate is used, has become one of the major controversial issues as these solvents are observed to be unstable under presence of superoxide radicals during the discharge process [113-115]. This leads to the decomposition of electrolyte during the discharge process and the formation of lithium organic complex (lithium alkyl carbonate) or lithium carbonate as a major discharge product as evidenced by infrared spectra measurement on the discharge product. These organic products can be decomposed upon charge to generate CO_2 studied by in-situ differential electrochemical mass spectroscopy (DEMS) [115]. These cells may be cycled several times, but eventually, the continuous decomposition and consumption of electrolyte lead to the unpredictable malfunction of the cell. The quality of air or oxygen used is unequivocally an important factor as the humidity can deteriorate the electrolyte system causing a lot of harmful side effects or it can directly react with lithium on the anode side [116]. H_2O may react with the reaction product to convert it into lithium hydroxide releasing oxygen gas. Lithium hydroxide can be further convert to lithium carbonate by capturing carbon dioxide from the air [117,118].

$$Li_2O_2 + H_2O \rightarrow 2LiOH + 0.5O_2 \quad (1\text{-}17)$$

$$LiOH + CO_2 \rightarrow Li_2CO_3 + H_2O \quad (1\text{-}18)$$

1.3 Capacity of Li-oxygen cell

There have been several disputes over how to define the cathodic capacity of Li-oxygen cells in terms of battery aspect [71,92,119,120]. This arises mainly because the Li-oxygen cell has some features both from the battery and the fuel cell at the same time; i.e. in Li-oxygen cell, the actual 'active' material, oxygen, is not loaded on the cathode structure initially, but is provided afterwards from the atmosphere. In other battery systems, the capacity of cathode often represents the 'efficiency' or the actual capacity of cathode active material attained during the electrochemical measurement in many cases, keeping in mind that the specific capacity itself is limited by its theoretical capacity (ideal capacity predicted from the electrochemical reaction). They will show the different capacities depending on the integrity of cathode material or the hardness of testing conditions, for example, C-rate. The theoretical capacity of the cathode active material for Li-oxygen cell, oxygen, can be calculated assuming following ideal electrochemical reaction occurs [92].

$$O_2 + 2Li^+ + 2e^- \rightarrow Li_2O_2 \quad (1\text{-}19)$$

The capacity of oxygen from the above reaction is 1675.16 mAh g^{-1}. Sometimes, it is useful to know the capacity of cathode material based on the discharge product, in that case, lithium

peroxide Li_2O_2. The capacity of lithium peroxide from the above reaction is calculated to be 1168.31 mAh g^{-1}. But in reality, it is hard to measure the real capacity produced from 1 gram of oxygen or how much oxygen is delivered to the reaction site to produce given capacity because oxygen is provided infinitely from the atmosphere (loading rate of cathode cannot be defined). Therefore, the definition of capacity based on oxygen or lithium peroxide is not so useful.

A more meaningful definition can be driven when we consider the actual factors to contribute the termination of Li-oxygen cell discharge reaction. The termination of the electrochemical reaction on the cathode is not directly related with the amount of oxygen available from the atmosphere, but it is strongly governed by the number of surface sites for the cathodic reactions and the porosity of cathode structure because these factors determine the activation and concentration polarization at the end stage of discharge process caused by excessive deposition of lithium peroxide [96,119,120]. The surface sites for the reaction and the porosity are usually provided with a high-surface-area amorphous carbon on the cathode. Therefore, it is convenient and useful to express the capacity in terms of the amount of carbon present on the cathode. As the number of surface site and actual porosity may be different depending on the type of carbon and geometric structure of the cathode even with the same amount of carbon, the proper choice of carbon and manufacturing good cathode structure is of high importance. The capacity of Li-oxygen cell in this thesis is primarily expressed by this type of capacity. Assuming the above reaction and following this definition, when 1 g of lithium peroxide is deposited on the surface of 1 g of carbon, this capacity corresponds to 1168.31 mAh per gram of carbon. In other words when 1 g of oxygen reacts on the surface of 1 g of carbon, the capacity is 1675.16 mAh per gram of carbon.

Another type of capacity which has a practical importance can be defined by calculating the capacity based on the total mass of cathode materials including carbon, catalyst and binder as well as oxygen deposited on the cathode in the form of lithium peroxide. In a practical sense, the capacity based on total mass or overall volume of battery will count. The amount of lithium is not included because it comes from the anode side and otherwise it will be counted twice when we calculate the total capacity of the whole battery. The limiting value for the capacity based on the total electrode mass is 1675.16 mAh g^{-1} when the capacity based on carbon amount takes on extremely high value [121]. The relationship between these two quantities can be described by the following equation.

$$Y = A\left[1 - \frac{1}{1 + r(x / A)}\right] \tag{1-20}$$

where Y : capacity based on the total mass of cathode

A : 1675.16 mAh g^{-1}

r : carbon abundance in electrode = carbon / (carbon + catalyst + binder)

x : capacity per gram of carbon

Figure 1.6 shows the relationship between capacity based on the amount of carbon (x-axis) and total electrode mass (y-axis). As carbon-based capacity reaches around 10,000 mAh/g, the capacity based on total electrode mass is saturated around 1000 mAh/g in case carbon occupies around 30 % of electrode mass.

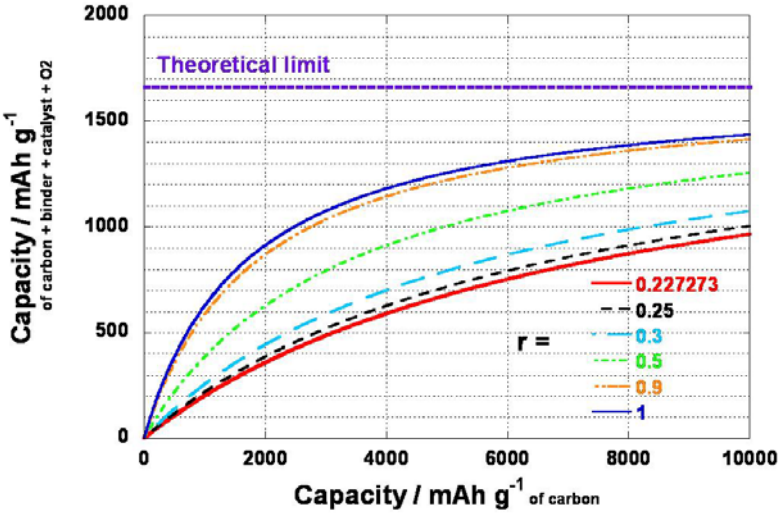

Figure 1.6 Chart for relationship between capacity of Li-oxygen cell based on total mass of electrode and capacity in terms of carbon mass. It critically depends on parameter r, the carbon ratio out of total electrode mass.

1.4 Catalyst and rechargeability

It is well known that both oxygen reduction reaction (ORR) and oxygen evolution reaction (OER) in aqueous solution are irreversible with large cathodic and anodic overpotentials so that each reaction requires the existence of each proper catalyst for reasonable performance; i.e. the activation overpotential of 0.30 ~ 0.45 V for ORR is common at typical current densities for metal-air cell even with catalyst [85,88]. The reduction of oxygen in the aqueous solution occurs usually by following two routes i.e. the direct four electron process and two electron process via peroxide formation. These processes in alkaline solution can be expressed as follows.

$$O_2 + 2H_2O + 4e^- \rightarrow 4OH^- \qquad E^o = 0.401 \text{ V vs. NHE} \qquad (1\text{-}21)$$

$O_2 + H_2O + 2e^- \rightarrow HO_2^- + OH^-$ $E^o = -0.065$ V vs. NHE (1-22)

The peroxide (HO_2^-) formed from **Reaction 1-22** is subject to either further reduction or dismutation reaction to produce hydroxide ion.

$HO_2^- + H_2O + 2e^- \rightarrow 3OH^-$ $E^o = +0.867$ V vs. NHE (1-23)

$2HO_2^- \rightarrow 2OH^- + O_2$ (1-24)

The oxygen reduction on porous carbon proceeds usually via the peroxide route, but a catalyst for peroxide elimination (**Reaction 1-24**) like manganese dioxide is necessary to maintain the peroxide concentration level as low as possible since the reduction potential of **Reaction 1-22** depends on the concentration of peroxide.

$$E = E^o - \frac{RT}{2F} \ln \frac{a_{HO_2^-} a_{OH^-}}{p_{O_2} a_{H_2O}} \quad (1\text{-}25)$$

While keeping the concentration of peroxide as low as possible, the potential via peroxide formation approaches the theoretical value for the four-electron process. On many catalysts like graphite, glassy carbon, most transition metal (Au, Hg, Ni, Co etc.), transition metal oxides and transition metal macro-cycles, the reduction process involves the formation of peroxide [85,88]. On the other hand, the reduction by catalysts like platinum, platinum alloys, silver and palladium proceeds through both direct four-electron and indirect two-electron processes [85,88].

The study on the oxygen reduction in aprotic solvent revealed that the primary reduced species in organic solvent is superoxide, O_2^- with tetraalkylammonium salt in the absence of strong Lewis or Brönsted acids [88,101]. This turned out to be a reversible one-electron process occurring in outer Helmholtz plane (OHP) regardless of the electrode surface. The reduction process becomes more complex and irreversible when a strong Lewis acid like alkaline metal ions or protons exist [101-103].

The rechargeability of the Li-oxygen cell was briefly addressed even in the very first paper by K. M. Abraham et al [92] and later J. Reed et al [111]. They used transition metal (cobalt) or metal oxide (λ-MnO_2) catalyst and showed that this cell is rechargeable up to a certain degree although much of their work was primarily focused on the simple discharge characteristics. The effect of catalytic activity on discharge-charge profile for Li-oxygen cell is described in **Figure 1.7**. The lowering of huge anodic overpotential has a key importance to avoid the carbon corrosion and reduce the electrolyte oxidation since this will have an enormous impact on subsequent cycling behavior of the cell. An enhanced kinetics or a different oxygen reduction mechanism (i.e. electrochemical reduction (**Reaction 1-15**) vs. chemical disproportionation (**Reaction 1-16**)) by catalyst from the amorphous carbon may produce the additional discharge capacity.

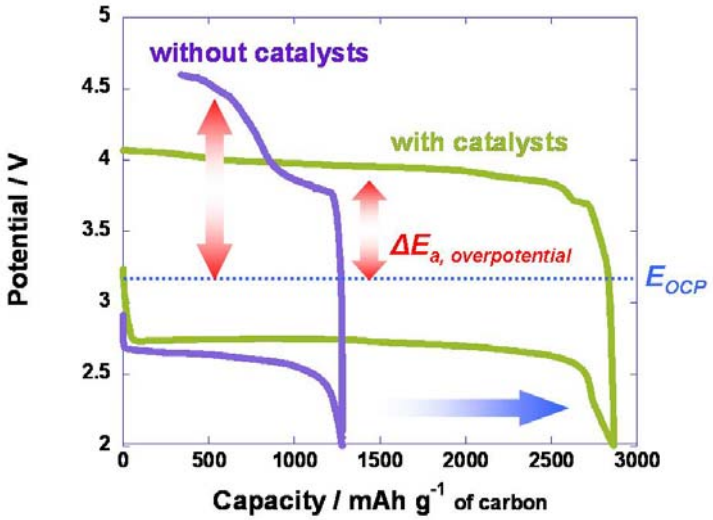

Figure 1.7 The effect of catalysts on the electrochemistry of Li-oxygen cell. The huge anodic polarization is reduced and the discharge capacity increases by the action of catalyst.

This issue was extensively re-addressed in several papers by P. G. Bruce et al. in 2006 - 2008 [99,100,121], where the oxygen reduction/evolution catalytic properties of various types of transition metal oxide, especially focused on the series of manganese dioxide with two different morphologies (bulk vs. nanowire) were examined. According to their data [121], alpha type manganese dioxide (α-MnO_2) nanowire with cryptomelane structure (**Figure 3.23**), which has one dimensional 2 × 2 tunnels made of edge- and corner-sharing MnO_6 octahedra along the wire axis was the best in the cell performance. They speculate that Li ions and oxygen molecules can incorporate into this tunneling structure, which somehow gives a better catalytic effect than the others. For example, 1 × 1 tunnels in β-MnO_2 are too small for efficient oxygen diffusion through it, and they do not have a good oxygen catalytic activity. The multivalent properties of manganese and inherent oxygen deficient structure of its oxide are also considered an important factor to determine the catalytic effect because they provide redox centers and surface sites for oxygen reduction / evolution reactions [122]. The effect of an intentional defective structure of these oxides on hydrogen peroxide

decomposition was investigated, showing a defective structure indeed performed better [114,123,124]. The high catalytic surface area from the nanowire and porous interwoven morphology of catalyst and carbon not only produced a high discharge capacity, but more importantly lowered charging potential dramatically.

Some reports insist that the basicity of solvent can influence the rechargeability of oxygen reduction by means of stabilizing the first reduced species, superoxide by forming quasi-stable $[Li(solvent)_n] - O_2$ [102]. According to Pearson acid base theory (HSAB theory), relatively soft Lewis base, superoxide can be stabilized by combining with a soft acid like TBA^+ ions [125-127]. When hard acid like Li ion is present in the solution, peroxide is a preferred form as peroxide is relatively a hard base. However, in case lithium ion forms a stable complex with solvent molecules (solvation), where the intensity of bonding is governed by the donor number (DN) of the solvent, it may behave like a soft acid [128]. They can stabilize superoxide ion through forming a quasi-stable lithium organic superoxide assembly. As oxygen reduction with TBA salt shows a reversible one-electron process by stable superoxide formation, these quasi-stable lithium organic superoxides may simulate a quasi-reversible behavior. From these observations, we see that the choice of right electrolyte system is one of the key elements in Li-oxygen cell.

1.5 Carbon corrosion and rechargeability

The carbon-support corrosion is a well-known phenomenon and one of the major issues in polymer electrolyte membrane (PEM) fuel cells [129,130]. During the startup or stop cycles, the presence of air on the anode side causes the reduction of oxygen to occur on

the local anode area (electrons are furnished by the hydrogen oxidation in different anode region), where necessary protons are provided from the adjacent cathode side. Sometimes this depletion of protons leads to the increase in the local cathode potential up to a point where carbon corrosion or oxygen evolution can occur.

$$C + 2H_2O \rightarrow 4H^+ + CO_2 + 4e^- \quad (1\text{-}26)$$

The rapid degradation of cathode by repetitive start-up and shutdown processes eventually leads to the catastrophic performance losses. Many system or material solutions are proposed to overcome this problem. Carbon corrosion can be mitigated by the use of fully graphitized carbon support or by using catalyst on the anode which has no catalytic activity towards oxygen reduction.

While the cathode part in fuel cell system is never intentionally subject to the anodic condition during the operation, on the contrary, the amorphous carbon on the cathode side in rechargeable Li-oxygen cell is exposed to the anodic condition in the oxygen-saturated electrolyte all the way through the charge process. As a result, it is natural that carbon corrosion occurs when the potential on the carbon electrode passes over anodic potential for carbon oxidation. However, as lithium peroxide exists on the carbon surface, which is deposited during the previous discharge step, the electrochemical surface modification by these peroxide species can occur ahead of a full-scaled oxidation by oxygen molecules. In the aqueous solution, the chemical surface modification by oxidizing agent, for example, hydrogen peroxide is one of the most common methods to generate hydrophilic surface structure with lots of oxygen containing functional groups on carbon [131,132]. The

resulting carbon surface usually includes many functional groups with acidic character such as carboxyl groups, lactone, phenol and lactol groups or with basic character such as chromene structure and quinone groups [131-134]. The surface modification of carbon by lithium peroxide may result in similar oxygen containing surface groups. These surface groups generally lower the electronic conductivity of carbon leading to the increase in the overall electrical impedance of the electrode. It is reasonable to assume that once functionalized, any further decomposition of Li_2O_2 on that surface carbon site (whether it is further carbon oxidation or oxygen evolution) is improbable because of the increased electrical impedance and chemical bond formation of dangling bonds with surface groups. As the number of surface carbon sites for the functionalization is limited, the amount of Li_2O_2 which can be decomposed for the functionalization on the carbon surface is limited, and it depends on the surface area or surface structure of carbon (degree of graphitization, etc). If the oxidized surface carbon could be reduced to the original state at the expense of peroxide decomposition / oxygen evolution, surface carbon might have a catalytic behavior and all Li_2O_2 existent on cathode would be decomposed. However, this reaction is difficult and any Li_2O_2 left will remain un-decomposed without catalyst. The subsequent catalytic activity of carbon for ORR will depend on the degree of recovery to fresh carbon surface upon reduction at the voltage range of interest. As a consequence, the rechargeability of Li-air cell will be severely limited by the property of carbon without the presence of proper catalyst.

1.6 Pyrochlores as bifunctional catalyst

Pyrochlore is a mineral name for the yellowish-brown niobium-containing mixed metal oxide, $(Na,Ca)_2(Nb,Ti)_2O_6(OH,F)$ with cubic space group Fd3-m (a = 10.366 Å) [135]. The name comes from the Greek words pyr- for 'fire' and chloros for 'green', which alludes that this mineral turns green upon ignition. But it is also generic term for the pyrochlore crystal structure with a chemical formula $A_2B_2X_6Z_{1-\delta}$ [136]. The A site is typically occupied by 8-coordinated cation with a large radius of ~1.0 Å like Na^+, Ca^{2+}, Sr^{2+}, Pb^{2+}, Sn^{2+}, Sb^{3+}, Y, U^{4+} or less frequently Ag, Mn, Ba^{2+}, Fe^{2+}, Bi^{3+}, Ce, Sc or Th, but it can be a vacancy or H_2O. The B is a 6-coordinated cation with high field-strength like Ta, Nb, Ti, Sb^{5+}, W, V^{5+}, Sn^{4+}, Zr, Hf, Fe^{3+}. The X site is typically taken up by anion like O, OH^- and F. The Z is an anion such as OH^-, F, O but it can be a vacancy, H_2O or mono-valent cation with a very large size (>> 1 Å) like K, Cs, and Rb. For instance, $Sb_2O_5{\cdot}4H_2O$ has a pyrochlore structure with A = H_3O^+, B = Sb, X = O and Z = H_2O [137]. Some pyrochlore materials with a composition of $A_2B_2O_{7-\delta}$ (A = Pb or Bi, B = Ru or Ir) exhibit the characteristics of metallic oxide [138-144], where single crystal electronic conductivity exhibits as high as 4.3×10^3 S/cm at 300 K in case of $Pb_2Ru_2O_{6.5}$ [142]. Structure of these pyrochlores is conveniently viewed as a composite of two interwoven substructures with a composition of $A_2B_2O_6O'_{1-\delta}$, where corner-shared noble metal-oxygen octahedra (BO_6) generate a cage-like B_2O_6 framework, which provides a conduction path for the electrons, while A element is linearly connected with special oxygen (O') in a manner like A-O'-A creating corner-shared $O'A_4$ tetrahedral structure within a cage (**Figure 1.8a**). This special oxygen can be absent partially or completely, which gives rise to oxygen non-stoichiometry within the structure (**Figure 1.8b**). Although generally these pyrochlore structures belong to cubic space group Fd3-m, in the case of $Pb_2Ru_2O_{6.5}$ where a half of the special oxygen is systematically absent, the ordered

vacancy structure gives additional symmetric features, and a new space group is assigned to be P-43m.

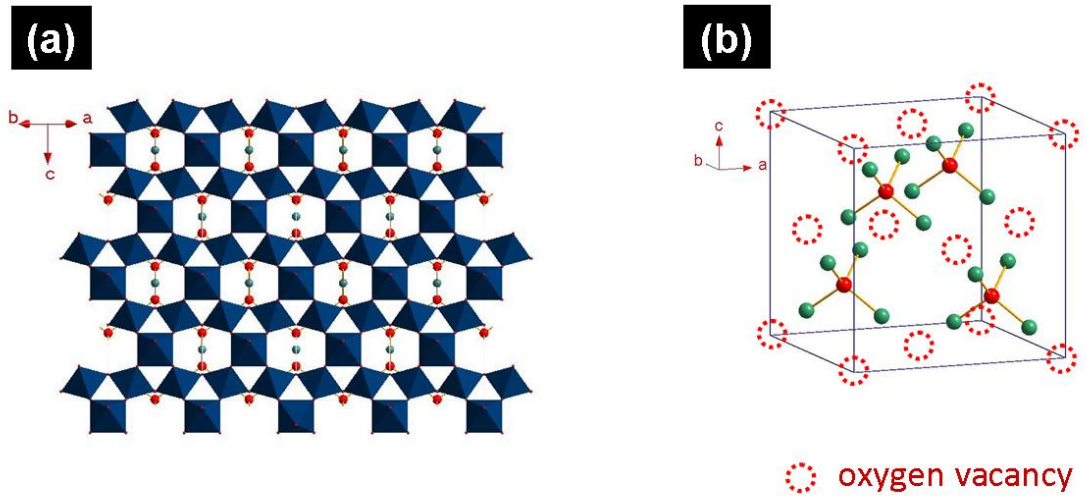

Figure 1.8 (a) Crystal structure of lead ruthenate pyrochlore, $Pb_2Ru_2O_{6.5}$ viewing from [110] direction, and (b) oxygen vacancy structure in –A–O'–A–.

It is also well known that a part of the noble metal in the B-site can be replaced by the A-site cation generating so-called expanded pyrochlore with a composition of $A_2[B_{2-x}A_x]O_{7-\delta}$, where x can be ranged from 0 to 1 [138,139,141]. The structure of these mixed oxides still sits on space group Fd-3m, and it is usually prepared from low-temperature solution-based methods, which lead to the formation of nano-crystallites with high surface area. Although partial substitution leads to the substantial decrease in the electronic conductivity [141], these oxides showed an excellent performance as a bifunctional catalyst for oxygen reduction/evolution in strong alkaline media [139]. Conventionally, lead or bismuth ruthenate pyrochlores were considered for oxygen reduction / evolution reaction catalysts in strong alkaline solution (i.e. zinc-air cell) [85], oxygen reduction catalyst for solid oxide fuel cells [145,146], or direct methanol fuel cells [147]. The oxygen reduction / evolution

capability is believed to originate from the multi-valent characteristics of transition metals, ruthenium or lead oxide and oxygen vacancies.

Some of these mechanistic details of ORR or OER on the pyrochlore catalyst in aqueous solution were investigated in several previous reports [85,137,139,148]. The ORR proceeds predominantly via a displacement of deprotonated water (OH^-) at O′ sites by an adsorbed superoxide ion ($O_2^-{}_{ads}$) and subsequent reaction with water molecule to produce hydroxide ions in the case where the solution pH is near or greater than **pzzp** (point of zero zeta potential) [137]. However, this reaction scheme becomes less plausible as the solution pH goes far lower than **pzzp** where oxygen vacancy site in O′ is filled with water molecule.

$$O_2 + e^- \rightarrow O_2^-{}_{ads} \quad (1\text{-}27)$$

$$Pb^{2+}OH^- + O_2^-{}_{ads} \rightarrow Pb^{2+}O_2^- + OH^- \quad (1\text{-}28)$$

$$Pb^{2+}O_2^- + 2H_2O + 3e^- \rightarrow Pb^{2+}OH^- + 3OH^- \quad (1\text{-}29)$$

Here, $Pb^{2+}X^-$ represents a surface site on pyrochlore catalyst, where oxygen vacancy is filled with X^- anion. In the case of the ruthenium pyrochlore, as protonation of Ru_2O_6 framework is possible when pH is less than 2 and OH groups are not too tightly bound, oxygen reduction can proceed even in the acidic solution via following exchange reaction [137].

$$Ru^{3+}OH^- + O_2^-{}_{ads} \rightarrow Ru^{3+}O_2^- + OH^- \quad (1\text{-}30)$$

Here $Ru^{3+}OH^-$ represents a surface site, where one of surface oxygen atoms around RuO_6 octahedra is protonated and $Ru^{3+}O_2^-$ denotes surface protonated oxygen around Ru^{3+} is

replaced by superoxide. The detailed mechanism of above reaction involves the formation of peroxide as an intermediate. Therefore, in the aqueous solution, ORR is catalyzed by ruthenate pyrochlore in wide pH range. The OER by pyrochlore in acidic solution occurs on the surface of the deprotonated surface oxygen of Ru_2O_6 framework ($Ru^{5+}O^{2-}$) anodic to the redox potential for Ru^{4+}/Ru^{5+} couple [137,149].

$$Ru^{4+}OH^- \rightarrow Ru^{5+}O^{2-} + H^+ + e^- \quad (1\text{-}31)$$

$$Ru^{5+}O^{2-} \leftrightarrow Ru^{4+}O^- \quad (1\text{-}32)$$

$$Ru^{4+}O^- + H_2O \rightarrow Ru^{4+}OOH^- + H^+ + e^- \quad (1\text{-}33)$$

$$2Ru^{4+}OOH^- \rightarrow 2Ru^{4+}OH^- + O_2\uparrow \quad (1\text{-}34)$$

At higher pH, the reaction proceeds in a similar way, but it also involves surface oxygens of the Ru_2O_6 framework together with water molecules or deprotonated water (OH^-) on the vacancy sites in O′ [137,149].

$$Ru^{4+}O^{2-} + Pb^{2+}OH_2 \rightarrow Ru^{5+}O^{2-} + Pb^{2+}OH^- + H^+ + e^- \quad (1\text{-}35)$$

$$Ru^{5+}O^{2-} \leftrightarrow Ru^{4+}O^- \quad (1\text{-}36)$$

$$Ru^{4+}O^- + H_2O + Pb^{2+}OH^- \rightarrow Ru^{4+}O_2^{2-} + Pb^{2+}OH_2 + H^+ + e^- \quad (1\text{-}37)$$

$$Ru^{4+}O_2^{2-} \rightarrow Ru^{4+}O^{2-} + (1/2)O_2\uparrow \quad (1\text{-}38)$$

This bifunctional feature suggests that metallic lead or bismuth ruthenate pyrochlore with oxygen vacancies could be viewed as an interesting candidate as a catalyst for the Li-oxygen cell. In the Li-oxygen cell, oxygen gas from the ambient atmosphere is reduced to

superoxide and subsequently decomposed to peroxide chemically or electrochemically during the discharge process. In contrast to fuel cell applications where only oxygen reduction activity counts, the catalytic behavior towards oxygen evolution is one of the major challenges in rechargeable Li-oxygen cell because it is well known that the decomposition of solid peroxide product involves a huge anodic polarization during the charge process [97,121]. As the fundamental features of ORR or OER processes shares many similarities between aqueous and organic electrolytes, the catalytic properties on the pyrochlore catalyst in the organic solvents must be closely related with the vacancies in special oxygen (O′) positions and Ru^{4+}/Ru^{5+} redox couples. In aqueous solutions, the oxygen vacancy sites on the pyrochlore structure are usually occupied by water molecules but in the organic solvent it is reasonable to assume that vacancies in O′ sites remain unoccupied ($Pb^{2+}\square$). From the analogy with aqueous solution, the peroxide formation with the following route is proposed under the presence of lead ruthenate pyrochlore catalyst. At first, oxygen molecules in the outer Helmholtz plane (OHP) near the catalyst surface experience a reversible one-electron reduction process to become superoxide, and eventually enter into the vacancy site in the special oxygen position. This superoxide at the vacancy site ($Pb^{2+}O_2^-$) further reduces to peroxide to produce lithium peroxide on the catalyst surface.

$$O_2 + e^- \rightarrow O_2^-{}_{ads} \quad (1\text{-}39)$$

$$Pb^{2+}\square + O_2^-{}_{ads} \rightarrow Pb^{2+}O_2^- \quad (1\text{-}40)$$

$$Pb^{2+}O_2^- + 2Li^+ + e^- \rightarrow Pb^{2+}\square + Li_2O_2 \quad (1\text{-}41)$$

Similarly, the oxygen evolution with the pyrochlore catalyst can occur on the surface oxygen of RuO_6 framework by Ru^{4+}/Ru^{5+} redox couple with following reaction scheme. Initially, peroxide diffuses to catalyst surface and occupies the vacancy site at the special oxygen position. The peroxide in the vacancy site is then transferred and bound to Ru^{5+}. Subsequently it reduces to become superoxide by the action of the Ru^{4+}/Ru^{5+} redox couple. The oxygen evolves from further decomposition of superoxide.

$$Pb^{2+}\square + Li_2O_2 \rightarrow Pb^{2+}O_2^{2-} + 2Li^+ \quad (1\text{-}42)$$

$$Ru^{4+}O^{2-} + Pb^{2+}O_2^{2-} \rightarrow Ru^{5+}O_2^{2-} + Pb^{2+}O^{2-} + e^- \quad (1\text{-}43)$$

$$Ru^{5+}O_2^{2-} \leftrightarrow Ru^{4+}O_2^- \quad (1\text{-}44)$$

$$Ru^{4+}O_2^- + Pb^{2+}O^{2-} \rightarrow Ru^{4+}O^{2-} + Pb^{2+}\square + O_2\uparrow + e^- \quad (1\text{-}45)$$

For lead ruthenate pyrochlore, the initial Ru^{5+} cation on the B-site [138] may facilitate the initial oxidation process. In case of expanded pyrochlore, some of the B sites are occupied by A site cations with high oxidation state like Pb^{4+}, or Bi^{5+}. Thus, the increased catalytic activity of these compounds is probably related with the multi-valent character of these metal ions.

1.7 Selection of electrolyte system for catalyst evaluation

Although the electrolyte system for Li-oxygen cell is actively under development, the criteria for a good electrolyte system have not been well established yet. The properties of conventional electrolyte systems have not been extensively investigated under either the

direct contact with oxygen radical or humidity from the air [150]. First of all, the stability of electrolyte in the presence of oxygen radicals is one of the most important properties. It is well known that the reduction of oxygen in the aprotic solvent creates superoxide anion (radical), $O_2^{\cdot -}$ [88,101]. Therefore, the resistivity against electrolyte reduction from the attack of these superoxide radicals is of a crucial importance. For example, propylene carbonate is reported to undergo the ring opening to become a linear carbonate by the action of superoxide radicals [115].

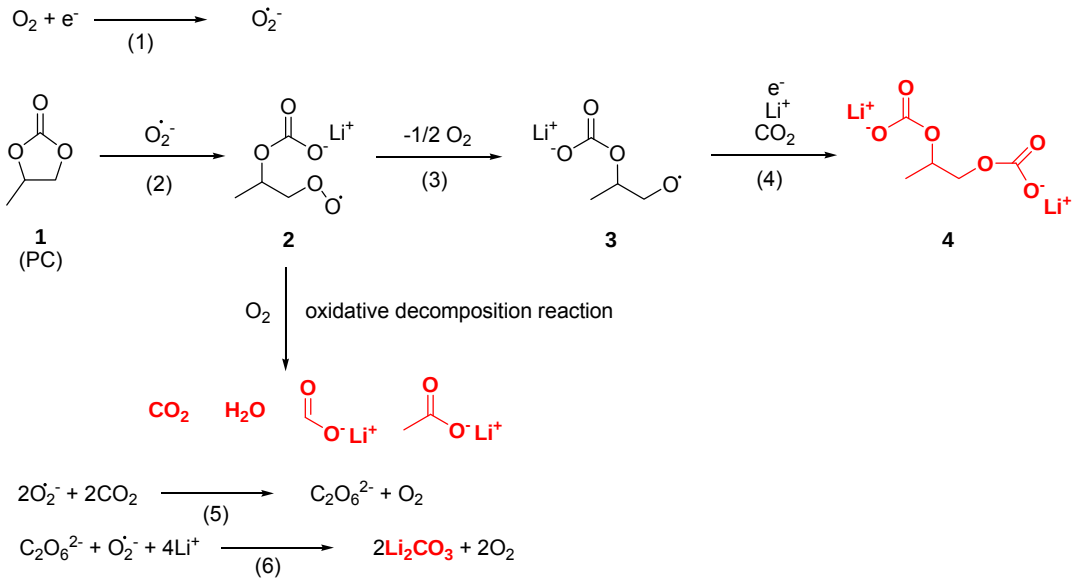

Figure 1.9 Mechanism for PC decomposition by superoxide radicals by P. G. Bruce et al.[151] PC ring opening by nucleophilic addition of superoxide on CH_2 group and subsequent reactions result in lithium propyl dicarbonate, lithium formate, lithium acetate, lithium carbonate, H_2O and CO_2 as reaction products.

Figure 1.9 shows the diagram for PC decomposition process proposed by P. G. Bruce et al [115,151]. The CH_2 group adjacent to the carbonyl moiety is easy to break up from the superoxide attack. After breakup, series of further reduction by superoxide radicals results in the lithium propyl dicarbonate, lithium formate, lithium acetate and lithium carbonate as well

as CO_2 and H_2O as discharge products [113-115,151]. The stability of lithium salt from the attack of superoxide radical is another major issue. For instance, the chelating bond between boron and oxygen in lithium bis(oxalato)borate, one of the common salts in lithium batteries, is a possible weak point for the superoxide attack because the negative charge on the terminal oxygen after breakup can be greatly stabilized by the adjacent C=O group. In the case of $LiPF_6$, superoxide attack can occur against PF_5, which exists at equilibrium with PF_6^- in normal condition in the electrolyte [150].

$$PF_6^- \leftrightarrow PF_5(g) + F^- \qquad (1\text{-}46)$$

The electrochemical peroxide decomposition usually accompanies a high anodic overpotential and oxygen gas evolves as a result. Oxidative electrolyte decomposition may occur on the cathode at the same time together with peroxide decomposition since in many cases, the catalyst for OER can work for electrolyte decomposition as well. The oxidation of the electrolyte system, therefore, should be suppressed for better cycling performance. Generally, ether-based solvents are much weaker to oxidation than carbonate-based solvents. For example, it is reported that tetrahydrofuran (THF) is oxidized at 4.0 V vs. Li/Li^+ on platinum surface [150,152]. The cyclic voltammetry under O_2 atmosphere can be a useful tool to determine the working potential window of the electrolyte for the Li-oxygen cell.

In terms of Li-oxygen cell performance, the solubility of oxygen and its diffusivity in the electrolyte solvent have practical importance. High oxygen contents and fast diffusion to the reaction site lead to less concentration overpotential even at higher current rate (more energy is extracted in a given time). The oxygen solubility of common organic solvents is

summarized in **Table 1.1**, which shows that solvents like THF and 1, 2 - dimethoxyethane (DME) exhibit high oxygen solubility. In an idealized condition, the oxygen diffusion coefficient (D) is associated with the viscosity of the solvent (η) through Stokes-Einstein relation [153,154].

$$D = kT / (6\pi\eta R) \qquad (1\text{-}47)$$

where R represents the hydrothermal diameter of oxygen molecule in the solvent and *k* is the Boltzmann constant. As the diffusion coefficient is proportional to the inverse of the solvent viscosity, the less viscous is the solvent, the faster is the diffusion. The viscosity of some common solvents is listed in **Table 1.1** together with other physical properties of interest like dielectric constant (ε) and boiling point (b.p.).

Table 1.1 The physical properties of various candidate solvents for Li-oxygen cell including dielectric constant (ε) [150], viscosity (η) [150], oxygen solubility [102,111] and boiling point (b.p.) [150]. O_2 solubility represents the amount of oxygen in micro-mole in cubic centimeter of solvent. For EC and DMC, viscosity is the value for 40 °C and 20 °C, respectively.

solvent	ε	η (25 °C) [cP]	O_2 solubility [μmol cm^{-3}]	b.p. [°C]
tetrahydrofuran (THF)	7.4	0.46	8.82	66
dimethyl sulfoxide (DMSO)	48	1.948	1.86	189
acetonitrile (ACN)	36.64	0.361	8.10	82
tetraethylene glycol dimethyl ether	7.79	4.05	4.70	275-276
1,2-dimethoxyethane (DME)	7.2	0.46	9.56	84
ethylene carbonate (EC)	89.78	1.90 (40 °C)	1.70	248
Propylene carbonate (PC)	64.92	2.53	3.20	242
Diethyl carbonate (DEC)	2.805	0.75	7.91	126
Dimethyl carbonate (DMC)	3.107	0.59 (20 °C)	7.28	91

The vapor pressure at room temperature (volatility) or the boiling point of the solvent is practically a meaningful criterion because Li-oxygen cell is supposed to be used in open

environments; i.e. oxygen comes from the air. The continuous vaporization causes the depletion of the solvent from the cell and the precipitation of the lithium salt. This increases the viscosity of the electrolyte system rapidly, which in turn enhances the overpotential of electrochemical reactions (slow diffusion of reactants). For example, although solvents like DME and THF have high oxygen solubility, their boiling points are relatively low (84 ^{o}C and 66 ^{o}C) for any practical consideration.

Other important factors include the conductivity of the electrolyte system, dielectric constant (solubility of lithium salt), hydrophobicity of the solvent (resistance to humidity contamination) [116], and stability of electrolyte system towards metallic lithium. In many cases, the anions of common lithium salts are extremely moisture-sensitive. For example, in $LiPF_6$ containing electrolyte, $LiPF_6$ directly or PF_5 from PF_6^- decomposes to produce corrosive by-products under the influence of humidity by following reactions [150].

$$LiPF_6 + H_2O \rightarrow LiF(s)\downarrow + 2HF + POF_3 \quad (1\text{-}48)$$

$$PF_5 + H_2O \rightarrow 2HF + POF_3 \quad (1\text{-}49)$$

In this thesis, two major electrolyte systems, 0.5 M LiBOB in PC and 1.0 M $LiPF_6$ in TEGDME are employed to investigate the effect of the stability of the electrolyte system against superoxide radical attack on the electrochemical performance and the characteristics of Li-oxygen cell.

1.8 Introduction to supercapacitor

Electrical capacitors [66,155] are passive circuit elements, which are designed for storing an electrical charge between two electrical conductor plates separated by insulating dielectric media. Applying a potential difference between two electrodes develops a static electrical field within a dielectric material, which can accumulate an electrical charge (Q), the amount of which is proportional to the voltage applied (V).

$$Q = CV \tag{1-50}$$

where the proportionality constant, C is defined as an electrostatic capacitance of the capacitor with a unit farad (*F*) [155], and thus represents the electrical charge accumulated per unit voltage applied. The value of capacitance is dependent on the dielectric constant of the dielectric insulator (ϵ), the surface area of the electrode (***A***) and the thickness of the dielectric media (***d***).

$$C = \epsilon \boldsymbol{A}/\boldsymbol{d} \tag{1-51}$$

The typical capacitance from conventional electrical capacitor is 0.1 ~ 1 μF with a voltage range 50 ~ 400 V [66]. Many efforts have been made to increase the capacitance, for example, by employing dielectric material with high dielectric constant or by increasing effective surface area by electrochemical etching of conductor surface.

Electrolytic capacitors [66] are similar in principle with electrical capacitors, but a very thin dielectric film is formed by anodizing an aluminum anode, which serves as a positive electrode to achieve a high capacitance per unit volume. Therefore, polarity exists for this type of capacitor where the negative terminal lead is shorter, which limits its application. This oxide layer has a high dielectric constant (~10), and its thickness is determined by the working voltage of the capacitor. The electrolyte is located between dielectric media and negative electrode and acts as a conductor. The electrolyte should possess several criteria like a high dielectric constant and low resistivity, and it is usually aqueous boric acid or sodium borate solution with many additives for retarding evaporation and harnessing chemical stability.

Conventionally, these capacitors are used for storing and providing electrical energy or blocking direct current in many electrical circuit. Today, advanced capacitors find a wide industrial application ranging from small electronics, computers to automobile and aircrafts where fast charging/discharging as well as high energy density are necessary. In order to meet these ever-increasing demands and new specifications for energy density and power levels, new types of capacitors are being developed including electrical double layer capacitors (EDLC) and pseudo-capacitors based on the transition metal oxides [66-73,156]. These capacitors utilize simple ion movement to the electrode surface or fast surface redox reactions on the metal oxide. They are called supercapacitors or ultracapacitors for their high energy density and stability over many cycles.

The electrical double layer capacitor (EDLC) stores electrical charges in an electrical double layer where effective charge separation occurs at a very thin electrode/ electrolyte interface (ions of opposite charge to electrode potential is arranged inside the double layer as

described in **Figure 1.2** [83]). The electrodes are usually made of activated carbon with high surface area (up to 3000 m^2 g^{-1}), which provides charge storage thousands times higher than the conventional capacitors without any significant degradation over hundreds of thousands of cycles [70,156]. They can offer much higher power density than batteries which allows a variety of commercial applications from backup powder sources for small electronic devices, power sources for engine start or acceleration of hybrid electric vehicles, and electricity storage from solar or wind power [20]. The capacitance of EDLC depends on the properties of carbonaceous material and electrolyte system employed and ranged from 50 ~ 100 F g^{-1}. A lot of carbonaceous materials other than activated carbon from various sources and the effect of variety of surface modifications were investigated for possible electrode materials including fullerenes, carbon nanofibers (CNF), carbon nanotubes (CNT), mesoporous carbon, graphenes and so on. EDLCs can employ either aqueous or nonaqueous electrolyte systems [156]. Compared with the aqueous electrolyte, which has about 1 V working voltage, and thus a lower energy density, nonaqueous electrolytes give higher working voltage of 2.3 ~ 3 V, but increased internal resistance.

Although EDLC provides much higher energy density than the conventional capacitors, the energy density from most commercial EDLCs is below 10 Wh kg^{-1}, which is considerably lower than those for common battery systems (35 Wh kg^{-1} for lead-acid battery, 150 Wh kg^{-1} for Li-ion battery) [73]. When some transition metal oxides are used as an electrode material for capacitors, their charge storage mechanisms include the capacitances both from non-faradaic and faradaic origins; capacitances from charging / discharging electrical double layer as well as fast surface redox reaction of metal oxide, which is called pseudo-capacitance [72,73]. The surface redox process produces the capacitance of at least

10 times higher than EDLC depending on the type of metal oxides. The most beneficial metal oxide in terms of energy density is hydrous amorphous ruthenium oxide, $RuO_2 \cdot xH_2O$, the protonated form of which, RuO_xH_y is a mixed electron-proton conductor with a high capacitance from 720 to 900 F g^{-1} [157,158], although its high commercial price is one of its main drawbacks. The extensive research for other metal oxides reveals many transition metals such as NiO, $Ni(OH)_2$, MnO_2, Co_2O_3, IrO_2, FeO, TiO_2, SnO_2, V_2O_5, MoO, and ZnO are potential candidates for commercial applications (**Figure 1.10**) [72,73]. Some transition metal nitrides such as vanadium nitride [159] and electrically conducting polymers [73] are also investigated for their high pseudo-capacitance.

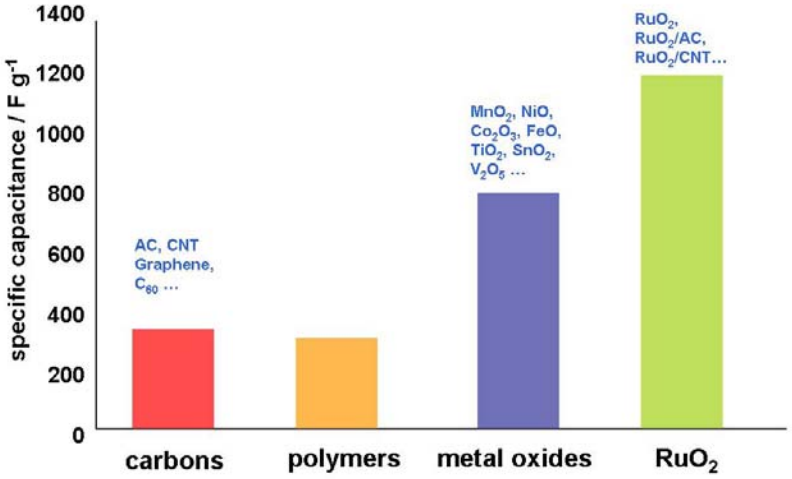

Figure 1.10 Common specific capacitance ranges of various supercapacitors from the literature.[73] The use of surface faradaic reactions in redox polymers and transition metal oxides increases specific capacitance significantly.

Recently, many studies have focused on the nano-composite of uniformly dispersed nano-sized metal oxide on the porous carbonaceous material (activated carbon, CNF, CNT etc) with a high surface area, which exhibits high specific capacitance and rate capability due to the increased electrochemical utilization of metal oxide and low concentration polarization

of electrolyte [160-162]. For some transition metal oxides, the hybrid systems, for example, MnO_2 as positive electrode and activated carbon as negative, are employed to increase the operating voltages as well as enhance the overall capacitance [72]. The maximum energy density and power level which can be delivered by these supercapacitors are expressed by following equations.

$$E = \frac{1}{2} C_T V^2 \tag{1.52}$$

$$P = \frac{V^2}{4R_S} \tag{1.53}$$

where C_T is the total capacitance, and R_S is the equivalent series resistance (ESR). Therefore, in order to achieve a high power level, the ESR should be minimized which relates to the internal resistance.

1.9 Scope of this thesis

This thesis analyzes the problems of the emerging high energy storage system of the Li-oxygen cell as well as transition metal oxide supercapacitors and deals with the systematic improvement of both systems by developing and applying new materials based on nanotechnology. Chapter II describes the main characterization techniques employed in this thesis. Chapter III accounts for the synthetic procedures for new nanostructured materials prepared in this thesis and shows their characteristics. Chapter IV addresses the current status of the Li-air cell and deals with the improvements made by applying nanostructured

materials developed in this thesis. In Chapter V, a supercapacitor based on pseudo-capacitance from mesoporous ruthenium oxide is presented. Finally, Chapter VI contains the summary of the whole thesis and the possible future work.

II. Characterization Techniques

2.1 Powder X-ray diffraction

Powder X-ray diffraction is a technique for identifying the crystal structure of the polycrystalline sample by investigating a set of diffracted X-ray peaks from the sample to the monochromatic incident X-ray beams. The diffraction of an X-ray beam by the crystal structure was first described mathematically by Max von Laue [163] in the early 20th century, but as Bragg [164] showed later, it can be more intuitively understood by supposing it as a reflection of an X-ray beam on a series of crystallographic planes through Rayleigh scattering, which is summarized into Bragg's law. From the **Figure 2.1**, the condition for the constructive interference to occur in the crystallographic plane (h k l) is that overall path difference (2Δ) should be integer (n) times of wavelength (λ) of the incident X-ray beam.

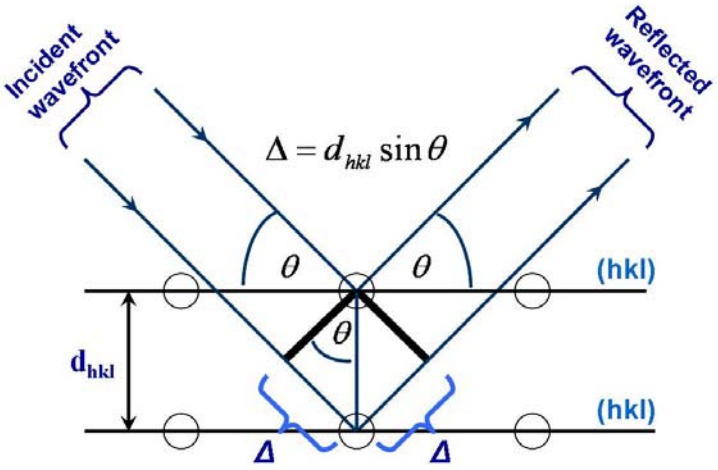

Figure 2.1 Diagram for Bragg's law, which explains that the X-ray diffraction can be intuitively understood from an optical analogy that crystallographic planes reflect incident X-rays.

$$2d_{hkl} \sin \theta_{hkl} = n \cdot \lambda \qquad (2\text{-}1)$$

where d_{hkl} and θ_{hkl} represent the interplanar distance and the angle between incident X-ray beam and crystallographic plane under investigation, respectively. As numerous crystal domains exist with arbitrary directions in the finely ground powder sample, some fraction of crystals with crystallographic plane (h k l) are always aligned with Bragg angle θ. The existence of a diffraction peak from the particular crystallographic plane depends on the symmetry group which the crystal structure belongs to, and its position is determined by unit cell parameters (a, b, c, α, β, γ). The intensities of diffraction peaks hold the information on the contents of unit cell like type of atoms, its positions, vacancies and so on. Therefore, a comparison of powder diffraction pattern of sample with a commercial database gives the identification of particular phases and their relative amounts, the existence of impurities and so on [165]. The shape of a diffraction peak is governed by many factors including instrumental parameters as well as sample properties; noticeably crystallite size of the sample. The diffraction peak of nano-crystalline (< 50 nm) material is broadened simply because the number of planes is not enough for complete constructive interference of waves. Scherrer equation [166] relates the broadness of diffraction peak of the nano-crystalline materials with the size of crystallographic domain in the sample.

$$\tau = K \lambda / (B \cdot \cos \theta) \qquad (2\text{-}2)$$

where τ represents the coherent length of crystal domain along the plane involved, B is the full width at the half maximum intensity (FWHM) in radian at angle θ, and K is a constant approximately equal to unity, which is related with the crystallite shape [167].

Powder X-ray diffraction in this thesis was performed using a Bruker D8-Advance powder diffractometer using Cu-$K_{\alpha 1}$ radiation (λ = 1.5405 Å) with scintillation detector.

2.2 Scanning electron microscopy

The interaction of material surface with a high energy electron beam (~40 keV) triggers a lot of phenomena such as emission of secondary electrons (SE), elastically back scattered electrons (BSE), transmitted electrons, and characteristic X-rays, which contains information on the topology and the chemistry of the material surface. These electron signals are captured in the detectors like SE detector and BSE detector to visualize surface morphology of the sample. The characteristic X-ray is generated when an electron beam removes the inner shell electron and another electron from the outer shell fills the empty hole, releasing X-rays with characteristic photon energy. These X-rays are used to identify the chemical composition of the sample. This technique is utilized in Energy-dispersive X-ray spectroscopy (EDX) and wave-length dispersive X-ray spectroscopy (WDS).

All the SEM images in this thesis were taken with a LEO 1530 field emission SEM instrument equipped with EDX attachment (Zeiss) located at the Waterloo Advanced Technology Lab. Images were taken using a 10 ~ 15 kV accelerating voltage with either the backscattered electron or secondary electron detection mode. In most cases to enhance the surface electrical conductivity of sample, thin layer (~10 nm) of gold was first sputtered on

the surface. In the case of gold-coated samples by other method (wet process), further gold-sputtering process was not applied.

2.3 Transmission electron microscopy

Electrons accelerated by high electrostatic potential (several hundreds kV) and thus having a high kinetic momentum, can interact with crystallographic structure of sample in a wave-like manner just like X-ray diffraction. This occurs because electrons assume wave-like character as it was proposed by Louis de Broglie in his Ph. D thesis in 1924 [168], which states that all matter has a wave-like character (λ) related with its momentum (**p**).

$$\lambda = h / \mathbf{p} \qquad (2\text{-}3)$$

where h is Planck's constant. The de Broglie wave length of electrons accelerated under 200 kV is 0.0251 Å, which is small enough to probe the crystalline structure of matter. Transmission electron microscopy (TEM) observes the morphology and the crystalline structure of sample when the high energy electron beam controlled by a set of magnetic lenses and apertures, is diffracted through a very thin sample. Besides images, electron diffraction patterns for a certain selected area of the sample can be obtained, containing crystallographic information. The image formed by selective area diffraction pattern (SAED) is a series of spots or rings which reflects the reciprocal space of the crystal lattice like X-ray diffraction patterns. Most TEM images in this thesis were taken on a Hitachi HD-2000 scanning transmission electron microscope (STEM) operating at 200 kV located at the

Centre for Nanostructure Imaging in University of Toronto. Powder samples were simply mechanically dispersed on the carbon grid.

2.4 Thermal analysis

Thermal measurements for thermogravimetric analysis (TGA) and differential thermal analysis (DTA) were carried out by SDT Q600 analyzer. For TGA, change in sample weight is continuously recorded while it is heated up to the target temperature with a constant heating rate or while it is kept at a specific temperature under desired atmosphere to estimate for example, the amount of water in the sample (**Section 3.1.1**). DTA measures the temperature difference between the sample and the inert reference material during the thermal cycle as function of heating temperature while it is heated (**Figure 2.2a**). Therefore based on DTA curve, information on the phase transitions can be traced which occurs during the thermo-cycle such as glass transition, crystallization, melting and sublimation (**Figure 2.2b**).

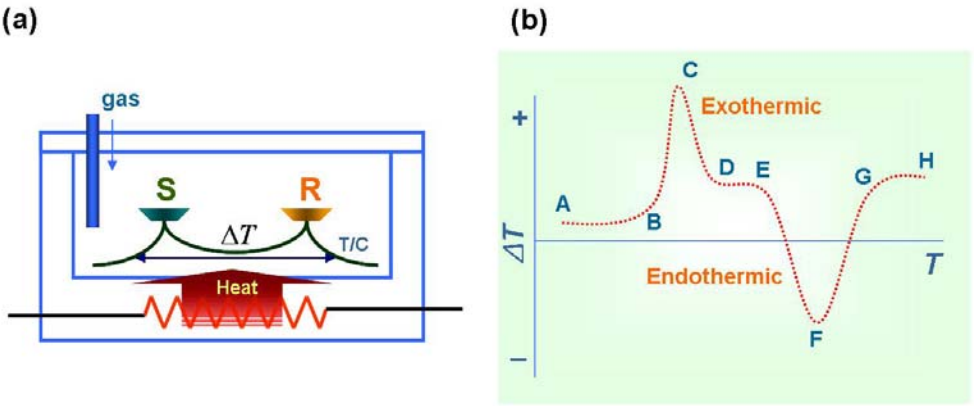

Figure 2.2 (a) Schematic for DTA equipment and (b) data presentation showing exothermic and endothermic events during thermal cycling. DTA measures the temperature difference between sample and inert reference.

2.5 Nitrogen sorption isotherm

The surface area and pore size distribution for mesoporous material [169] and nano-particles were calculated from the nitrogen sorption isotherm [170] data measured by Quantachrome Autosorb-1. Samples were usually dried in a vacuum oven at 80 ^{o}C overnight and then were further dried in the degassing station at 150 ^{o}C for 24 h before measurement. The N_2 adsorption-desorption was carried out at 77.3 K.

The Brunauer-Emmett-Teller (BET) method [171] based on **Equation (2-4)**, which relates the amount of gas adsorbed (V) with relative pressure (P/P_o) was applied to the initial adsorption data ($P/P_o < 0.3$) to estimate the volume needed for the formation of monolayer of adsorbate on the sample surface (V_m) [172].

$$\frac{1}{V\left[\left(P_o / P\right)-1\right]} = \frac{1}{V_m C} + \frac{C-1}{V_m C}\left(\frac{P}{P_o}\right) \qquad (2\text{-}4)$$

From the slope (s) and y-intercept (i) of the plot, $[V(P/P_o\text{-}1)]^{-1}$ vs. P/P_o for the initial several points ($P/P_o < 0.3$) of adsorption branch, V_m can be calculated by following equation.

$$V_m = (s + i)^{-1} \qquad (2\text{-}5)$$

The surface area of sample (S_{BET}) was converted from V_m through following equation.

$$S_{BET} = (V_m / V_N) \times N_A \times A_{CS} \qquad (2\text{-}6)$$

where V_N, N_A, A_{CS} represents the molar volume of nitrogen at STP (22.414 L/mol), Avogadro number, and average cross-sectional area of nitrogen gas (16.2 $Å^2$), respectively.

The micropore [169] volume in the sample was estimated by the t-plot method [173], which describes the relationship between the amount of total adsorbed gas and the thickness of the adsorbed layer. The y-intercept and slope in a t-plot represent the micropore volume and surface area, respectively. The statistical thickness of the adsorbed layer depends on the relative pressure and many equations based on empirical, semi-empirical and theoretical formulae exist, such as the de Boer equation [173], Hasley equation [174] and carbon black equation.

The pore size distribution was estimated by the Barrett-Joyner-Halenda (BJH) method, [175] which is applied to the desorption branch. BJH method uses modified Kelvin equation [176] to calculate pore diameter (r_p) from capillary diameter (r_k) and statistical thickness (t).

$$r_p = r_k + t \tag{2-7}$$

where r_k and t are functions of relative pressure (P/P_o). The capillary diameter is given by Kelvin equation.

$$r_k = \frac{-2\gamma V_L}{RT \ln(P/P_o)} \cos\theta \tag{2-8}$$

where γ is the surface tension of nitrogen at its boiling point, V_L is the molar volume of liquid nitrogen and θ is defined in **Figure 2.3**. The mesopore filled with liquefied adsorbate gas by capillary force is described in **Figure 2.3**.

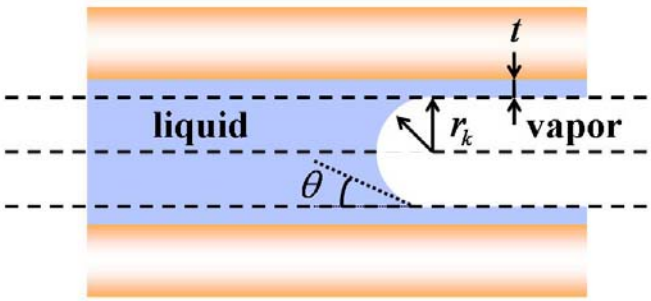

Figure 2.3 Schematic diagram of mesopore filled with liquefied adsorbate in equilibrium with gas phase. Overall pore radius is sum of Kevin radius and statistical thickness layer on the wall, both of which are functions of relative pressure (P/P_o). Therefore desorbed gas at a certain pressure consists of two components.

The pore size distribution (ΔV_p) is then obtained based on the following relation of pore volume at one specific desorption step (ΔV_p) with other externally measured parameters like desorption pore volume (ΔV), change in statistical thickness (Δt), pore diameter and capillary diameter.

$$\Delta V_P = V_k \left(\frac{r_p}{r_k} \right)^2 = \left(\Delta V - \Delta t S \right) \left(\frac{r_p}{r_k} \right)^2 \qquad (2\text{-}9)$$

where S represents the surface area, when the surface of adsorbed layer with thickness t is considered as a 'real' surface, and thus $\Delta t S$ represents a volume of desorbed gas contributed by thinning of statistical thickness from the pore as pressure goes down.

2.6 Infrared spectroscopy

Infrared spectroscopy measures the absorption spectrum (thus transmitted or reflected spectrum) of a sample when it is exposed to the electromagnetic waves of wide infrared ranges especially to identify chemical functional groups and thus chemistry of the sample [76,154]. The electromagnetic waves in the infrared range interact with rotational-vibrational (4000 ~ 400 cm^{-1}) and rotational (400 ~ 10 cm^{-1}) characteristics of free molecules or functional groups in the condensed phase. They are absorbed when the photon energy of infrared corresponds to the energy difference in the rotational-vibrational energy levels of the sample. However to be detected in the infrared spectroscopy, vibration of the molecules or functional groups should be associated with the change in the permanent dipole moment. These vibrational modes include symmetrical stretching, antisymmetrical stretching, scissoring, rocking, wagging, twisting and so on. A linear molecule with N constituent atoms has 3N-5 vibrational modes whereas non-linear molecule with N atoms has 3N-6 vibrational modes [154]. Infrared spectra in this thesis were measured using a Bruker Vertex 70 FT-IR spectrometer in the spectral range from 4000 to 400 cm^{-1}.

2.7 Electrochemical measurement techniques

2.7.1 Galvanostatic cycling

Most of battery performance tests were carried out by a galvanostatic charging and discharging technique. In this testing mode, constant anodic (or cathodic) current is applied

to the electrochemical system and its potential response with time is observed (thus constant-current chronopotentiometry) [83]. In a typical battery test, a constant current is employed to extract the useful energy from the battery during the discharge process until the energy stored in the battery is completely depleted as evidenced by sharp voltage drop at the end of discharge. After the full discharge, a constant current is again applied in the reverse direction to provide battery with electrical energy during the charge process, which can reverse the electrochemical reactions. The full restoration of energy in the battery is marked by a sharp increase in cell voltage. The proper voltage cutoff should be made to prevent other detrimental electrochemical reactions from occurring such as electrolyte oxidation, corrosion of cathode active material as well as other cell components. In general, the existence of unwanted side reactions leads to the rapid capacity fading upon cycling. The magnitude of current applied is usually expressed in terms of C-rate which represents how fast the energy is taken into/out of battery. Considering the nominal capacity of battery, if the current is applied in such a magnitude that the battery will be completely discharged in 2 hours, the C-rate is C/2.

2.7.2 Potential sweep method

In the potential sweep method [83], the potential of the working electrode is increased (or decreased) with a constant ramping speed to the desired potential versus the reference electrode to observe the overpotential related with oxidation (reduction) of active species in the solution. In cyclic voltammetry (CV), the scanning direction is reversed at high or low turning point (E^{λ}) to make a complete round potential sweep like **Figure 2.4**. In the

reversible system, the reduction (or oxidation) potential (E_{pc}) is independent of scanning speed (v) and is related with half way potential ($E_{1/2}$) through the following equation.

$$E_{pc} = E_{1/2} - (28.5/n) \text{ mV at } 25\ ^{o}\text{C} \quad (2\text{-}10)$$

In most cases, half way potential is similar with equilibrium potential (E^{o}). Thus the potential difference in CV between oxidation and reduction peaks in the reversible system is (57/n) mV regardless of scanning speed. The cathodic (or anodic) peak current density (i_{pc}) is related with the scanning speed with the following equation at 25 ^{o}C.

$$i_{pc} = 2.69 \times 10^{5}\ n^{3/2}\ D^{1/2}\ C^{*}\ v^{1/2} \quad (2\text{-}11)$$

where D and C^{*} represents the diffusivity in $cm^{2}\ s^{-1}$ and bulk concentration of reacting species in mol cm^{-3}, respectively. Therefore, as the scanning speed increases, so does the peak current. In addition, the measurement of peak current with varying scanning speed leads to the information about n and D. In an irreversible system involving one-step and one-electron process, however, the location of reduction (oxidation) potential is dependent on the scanning speed, i.e. as scanning speed increases, the reduction peak moves to more negative value and thus the potential difference between oxidation and reduction peak is much greater than (57 / n) mV. The reduction peak current for irreversible systems is also expressed in a similar manner with that for the reversible system.

$$i_{pc} = 2.99 \times 10^{5}\ \alpha^{1/2}\ D^{1/2}\ C^{*}\ v^{1/2} \quad (2\text{-}12)$$

where α represents a transfer coefficient for the reaction. The irreversible process which has more than one-electron involved or multi-step processes is seldom expressed quantitatively for their complexity.

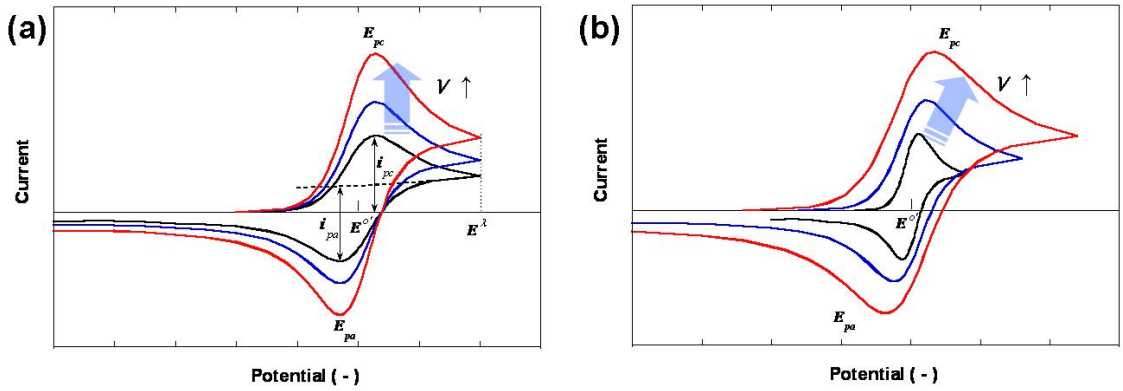

Figure 2.4 Typical cyclic voltammograms with an increasing scanning speed (ν) for (a) reversible system and (b) totally irreversible system. For reversible system, peak potential is independent on scanning speed and peak current is proportional to $\nu^{1/2}$. For totally irreversible system, peak potential appears farther from the equilibrium potential as scanning speed increases but peak current is still proportional to $\nu^{1/2}$.

2.7.3 Impedance measurement

The electrochemical impedance spectroscopy [177] is an electrochemical analog for the impedance from electrical engineering. The governing equation in the electrical circuit, Ohm's law (R = V/ I) is replaced by the Butler-Volmer equation. The double layer charging and charge-transfer at the interface for an electrochemical cell is simulated by parallel connection of double layer capacitance (C_{dl}) and charge-transfer resistance (R_{ct}) [74].

Herewith the connection with the resistance from the electrolyte system (R_∞) in series makes a common 'equivalent circuit' used for analysis for the electrochemical system (**Figure 2.5a**).

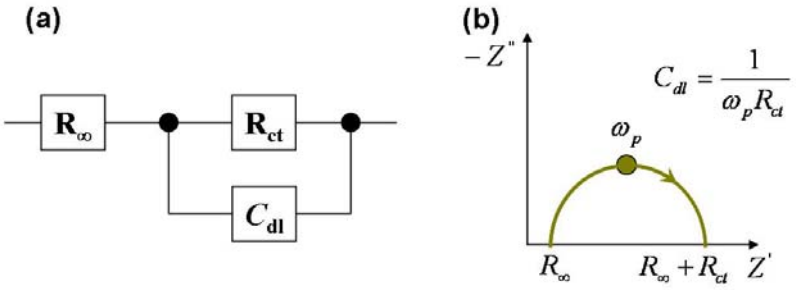

Figure 2.5 (a) Common equivalent circuit containing charge transfer resistance (R_{ct}), double layer capacitance (C_{dl}) and solution resistance (R_∞) for a simple electrochemical system and (b) data presentation using Nyquist plot and analysis.

In practice, a sinusoidal voltage with the amplitude V_o and frequency ω is applied to the system and the current response, which usually has the same frequency, but different phase angle is measured to calculate the impedance in the frequency domain, **Z** = **V** / **I**., where ***V*** and ***I*** represent Laplace transformed voltage and current, respectively, from time domain [178]. The measurement of impedance response for a wide range of frequency (typically from 10^6 to 10^{-4} Hz) provides a spectroscopic representation of the system in response to the periodic perturbation, which is called electrochemical impedance spectroscopy (EIS). Because the relationship between voltage and current in the electrochemical system is not linear, voltage perturbation should be as small as possible so that Butler-Volmer equation effectively simulates linear relationship (otherwise impedance cannot be defined) [177,178]. At this point, simple mathematical treatment reduces Butler-Volmer equation to the following relation on charge transfer resistance (R_{ct}) with exchange current (i_o).

$$R_{ct} = V_T / (n\, i_o) \qquad (2\text{-}13)$$

where V_T and n represent thermal voltage (kT/e) and number of electrons involved. Practically, the excitation voltage in EIS should be much smaller than thermal voltage so that the exponential term in Butler-Volmer equation can be linearized. At 25 ^{o}C the value of thermal voltage is around 25 mV, and the excitation voltage of from 5 to 10 mV is usually taken. However, the voltage perturbation should be large enough to overcome noise from the ambient environment or electronics.

The impedance data obtained from the electrochemical system is usually presented in two ways, i.e. Bode plot and Nyquist plot. In a Bode plot, the absolute value of impedance and phase difference are plotted as a function of frequency, whereas in a Nyquist plot, sets of real and imaginary impedance data are presented in the complex plane (**Figure 2.5b**). In either case, the impedance data are least-square fitted into the equivalent circuit derived from physical modeling of electrochemical system. The optimized values for the circuit elements (R_1, R_2, C_1, C_2 …) in the equivalent circuit are utilized to estimate physical and chemical parameters in the electrochemical system. Therefore, the correct understanding and the right modeling of the electrochemical system under investigation are vital for a meaningful analysis and interpretation. In reality, however, the impedance obtained from electrochemical systems often cannot be fitted well enough with just a combination of resistors and capacitors. This occurs simply because the circuit elements in the electrochemical system are not ideal; for example, the behavior of electrical double layer cannot be completely described by a simple capacitor, where the capacitance is often frequency-dependent with a characteristic distribution. To compensate this deviation from

ideality, a lot of other circuit elements are introduced such as a constant phase element (CPE), Warburg impedance (W_∞, W_s, W_o) and even negative resistance and inductors (L).

III. Synthesis and Characterization of Materials

3.1 Mesoporous ruthenium dioxide

3.1.1 Synthesis procedure

To prepare surfactant-templated mesostructured ruthenium hydroxide, 0.800 g of 25 % (w/w) aqueous hexadecyl-trimethylammonium chloride (Fluka, $C_{16}TMA^{+}Cl^{-}$) solution, 6.600 g of ruthenium(III) nitrosyl nitrate solution (Sigma-Aldrich, $Ru(NO_3)_x(OH)_y$, $x + y = 3$, 1.53 wt. % Ru), and 2.0 g of deionized water were mixed in a 20 mL PTFE bottle and stirred for 1 h at room temperature. The solution was transferred to a 100 ^{o}C oven and heated for 12 h with the bottle tightly capped. Subsequently, 2.0 g of a 2 M aqueous NaOH solution was added and the solution was vigorously stirred for 6 h at room temperature, transferred to the 100 ^{o}C oven and heated for another 12 h. The reaction mixture was filtered and washed with copious amounts of deionized water and was dried in the air at 60 ^{o}C to yield surfactant-templated mesostructured ruthenium hydroxide **mRO-1** (yellowish powder, typically 0.2 g). For the synthesis of mesoporous RuO_2 with quasi-crystalline wall character (**mRO-3)**, **mRO-1** was heated in a forced convection oven for 36 h at 200 ^{o}C. Less than 36 h heating resulted in the hydrous amorphous phase, **mRO-2**. Mesoporous, crystalline rutile (coherence length of 5.3 nm) RuO_2 **(mRO-4)** was obtained by heating **mRO-1** in 48 h at 200 ^{o}C.

3.1.2 Characterization

The porous samples were prepared by starting from surfactant-templated ruthenium hydroxide (**mRO-1**) followed by gradual removal of the surfactant through subsequent heat-treatment. The low-angle and wide angle powder X-ray diffraction patterns for the surfactant-templated ruthenium hydroxide (**mRO-1**); the amorphous mesoporous RuO_2 formed after template removal (**mRO-2**); the quasi-crystalline mesoporous RuO_2 (**mRO-3**) and crystalline RuO_2 (**mRO-4**) are shown in **Figure 3.1**.

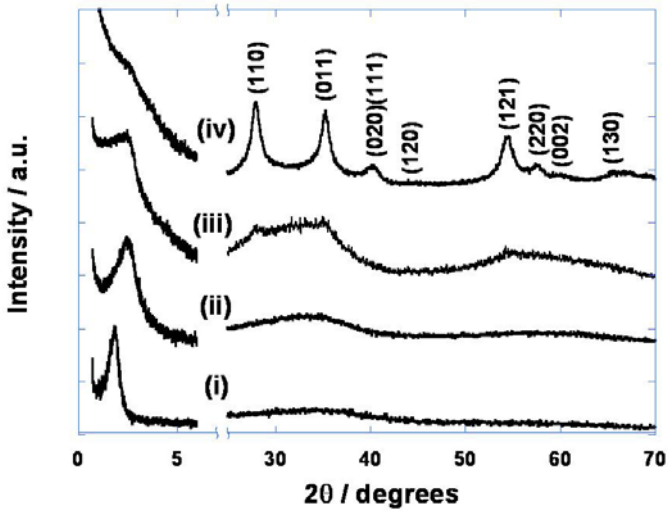

Figure 3.1 Low-angle and wide-angle X-ray diffraction patterns of (i) mesostructured ruthenium hydroxide and (ii) mesoporous amorphous or (iii), (iv) quasi-crystalline RuO_2, which represent samples heat-treated at 200 ^oC for 12 h, 36 h, 48 h, respectively.[179]

For **mRO-1**, the reflection at 1.86 ^{o} was indexed as (100) and indicates the formation of a mesostructure having an inter-planar *d* spacing of 4.7 nm, as expected for a hexagonal mesostructure templated by $C_{16}TMA^+Cl^-$ [180-182]. Gentle decomposition of **mRO-1** for 12 h at 200 ^oC to remove the surfactant results in the formation of amorphous mesoporous RuO_2 (**mRO-2**), as shown in the wide-angle XRD pattern. More prolonged heating (12 - 36 h at 200 ^oC) nucleates the growth of nano-crystallites of RuO_2 within the wall structure, a process that is controlled by kinetics. The wide-angle diffraction pattern initially shows

poorly resolved reflections corresponding to the rutile phase of RuO_2, which sharpen upon further heat treatment. The broadness of the reflections, as estimated by application of the Scherrer equation, suggests a coherence length of about 5.3 nm for the more crystalline, but still porous sample (**mRO-4)**. The crystallite size of the initial poorly crystalline sample (**mRO-3**) is considered to be in the order of the wall thickness of the mesoporous material, about 1.5 nm. The low-angle reflections of **mRO-2** and **mRO-3** have reduced intensities, and they are broader than those of **mRO-1**, suggesting slight disordering of the mesostructure during heating. The shift of the main reflection to higher angle for the mesoporous products is consistent with a contraction of the pores upon removal of the surfactant, to give an inter-planar *d* spacing of approximately 3.5 nm.

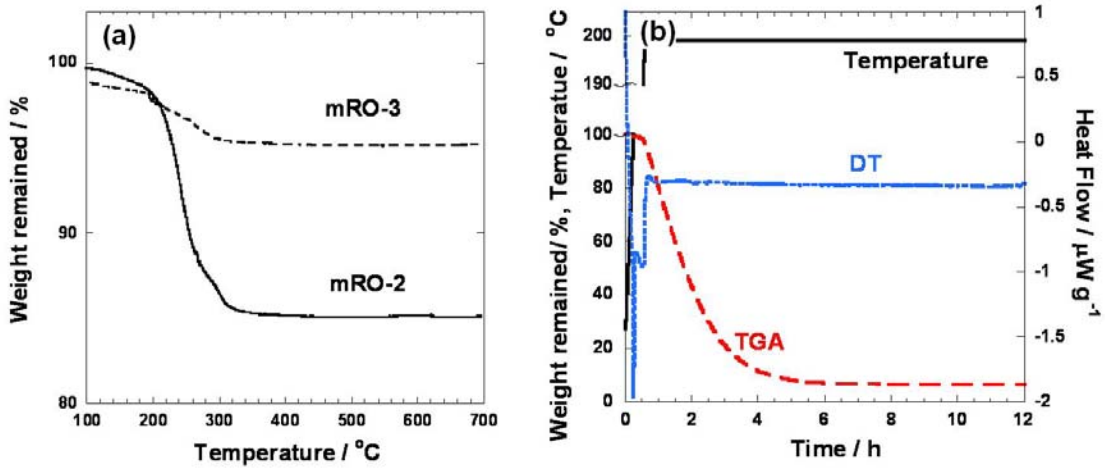

Figure 3.2 (a) Thermogravimetric analysis for amorphous and crystalline mesoporous RuO_2 in air.[179] The water content *x* in $RuO_2 \cdot xH_2O$ was determined by the ratio of initial and final weight of the sample. (b) TGA/DTA of the pure surfactant on isothermal annealing at 200 °C. The temperature was raised to 200 °C using a 10 °C min^{-1} rate, and decomposition was complete after 6 h at 200 °C.

The water content of **mRO-2** and **mRO-3** were evaluated by thermogravimetric analysis (TGA) as shown in **Figure 3.2a**. The residual mass at 700 °C was compared with that at 200 °C to determine the water contents in the crystalline structure, $RuO_2 \cdot xH_2O$. The carbon

residue in the sample from the decomposition of organic compounds based on chemical analysis is almost negligible (less than 0.02 %). The thermogravimetric analysis (TGA) of the pure surfactant also showed only a relatively low (6 %) residue after a temperature hold at 200 ^{o}C for 12 h (**Figure 3.2b**). For the amorphous sample **mRO-2** heated for 12 h at 200 ^{o}C, the material contains 1.3 water molecules per RuO_2, considered to be ideal for pseudocapacitor properties [157,183,184]. The stoichiometry of the crystalline material obtained on more prolonged heating (36 h at 200 ^{o}C) was estimated to be RuO_2•0.4H_2O. Removal of the water of hydration occurs simultaneously with structural crystallization.

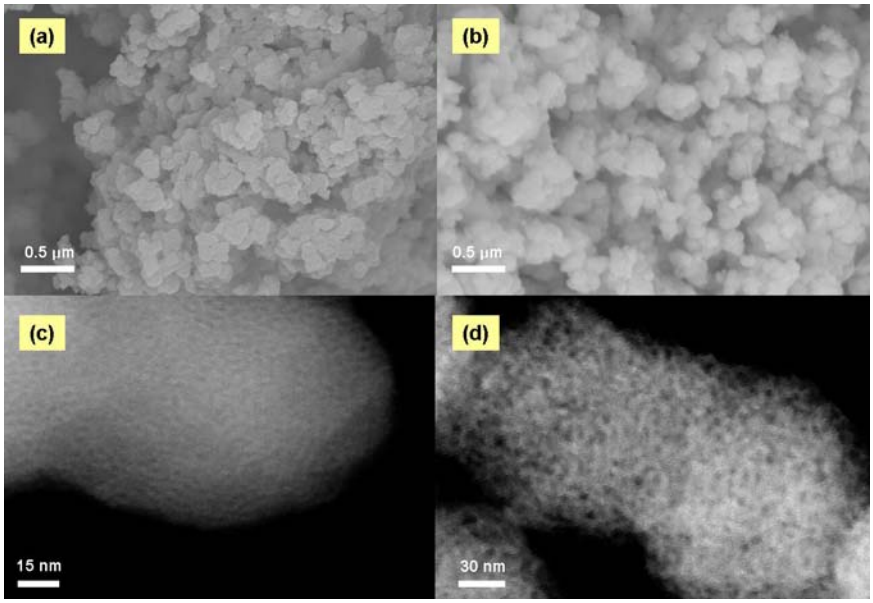

Figure 3.3 SEM (upper) and TEM (lower) images of **mRO-1**, templated mesostructured ruthenium hydroxide (a,c); and **mRO-3** quasi-crystalline mesoporous RuO_2, (b,d).[179]

The nano-sized character of the mesostructured materials is shown in the SEM and TEM images in **Figure 3.3a-d**, which reveal the plate-shaped primary particles of **mRO-1** to have basal dimensions of about 100 nm. The overall morphologies before and after surfactant removal and crystallization of the RuO_2 wall structure; i.e., of **mRO-1** and **mRO-**

3 were very similar. This is best demonstrated by the high resolution TEM images. The surfactant-laden mesostructured RuO_2 **(mRO-1)** shows a relatively smooth surface structure with an underlying "worm-like" pattern, reminiscent of mesoporous silica produced from non-ionic surfactant templating routes [185,186]. The single peak in the low angle XRD pattern arises from the constant pore size and wall thickness throughout the overall structure. The partially crystallized RuO_2 **(mRO-3)** displays the same particle morphology, but the porous structure of the framework created by the removal of the surfactant is clearly visible. Homogeneously sized mesopores about 2 nm in diameter are evident. The overall morphology and order are similar to that of crystalline TiO_2 obtained by polymer-mediated "scaffold" templating [187], but the pore dimensions and wall thickness are smaller by almost an order of magnitude, and the surface area is much higher. This accounts for the much higher surface area of our material, which is necessary for good catalytic and/or capacitance properties.

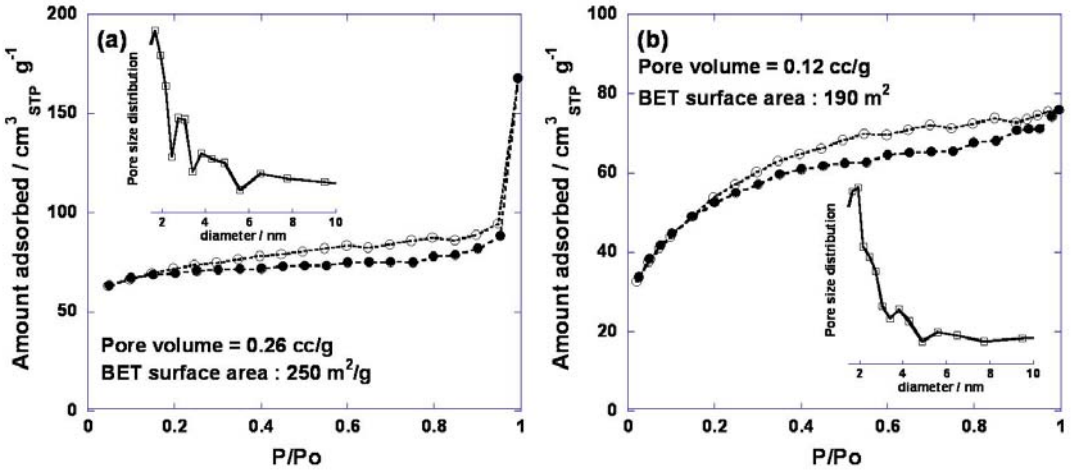

Figure 3.4 Nitrogen sorption isotherms measured at 77.3 K and the corresponding BJH pore size distributions (inset) from the desorption branch (a) for amorphous mesoporous RuO_2 (**mRO-2**) and (b) for quasi-crystalline mesoporous RuO_2 (**mRO-3**).[179]

Nitrogen sorption isotherm measurements on **mRO-3** at 77 K (**Figure 3.4b**) reveal a very high surface area and pore volume, of 190 m^2 g^{-1} and 0.12 cm^3 g^{-1}, respectively. It is higher than the values obtained for mesoporous crystalline Nb_2O_5, of 72 m^2 g^{-1}, although that material exhibited much larger mesopores (20 nm) [187]. The pore size distribution was calculated by applying the Barrett-Joyner-Halenda algorithm to the desorption branch data. A minor portion of mesopores around 4 nm and 6 nm are present, in addition to a large proportion of micropores and mesopores centered around 2 nm. The latter represent the main structural porosity as indicated in the TEM image in **Figure 3.3d**. The high surface area of this material is created by these small-sized and multiple pore structures. This variation is ideal for supercapacitor properties [186,188].

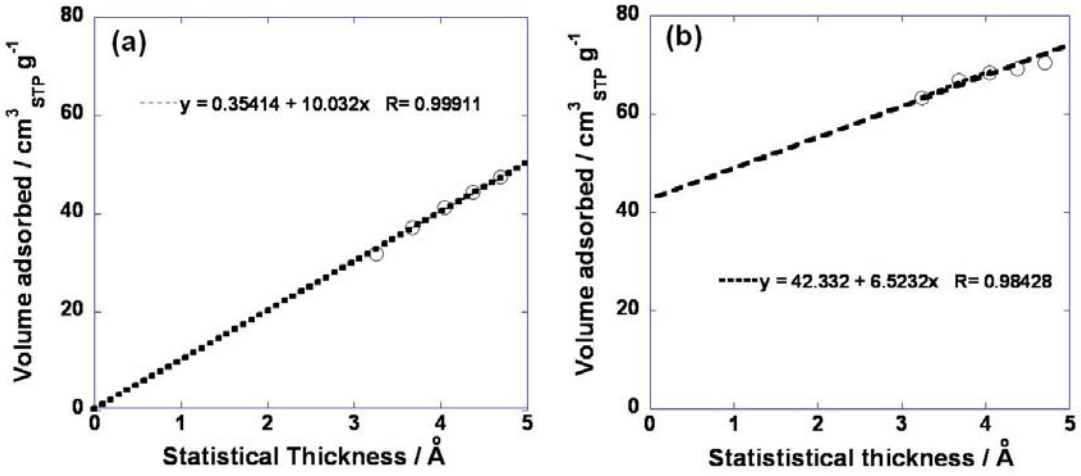

Figure 3.5 The t-plots (a) for amorphous mesoporous RuO_2 (**mRO-2**) and (b) for quasi-crystalline mesoporous RuO_2 (**mRO-3**).[179] The micropore volume was calculated from the y-intercept of the graph.

The amorphous porous material, **mRO-2** possesses a substantially larger surface area of more than 260 m^2 g^{-1}. However, about a third of the pore volume is contributed by the micropores as measured by the t-plot analysis (**Figure 3.5b**) and summarized in **Table 3.1**.

These micropores collapse as crystallization proceeds (**Figure 3.5a**). The origin of the microporosity in the amorphous material can be addressed by consideration of the chemistry used to assemble the mesostructure.

Table 3.1 Physical properties of mesoporous ruthenium precipitate, amorphous $RuO_2 \cdot 1.3H_2O$, and crystalline mesoporous $RuO_2 \cdot 0.4H_2O$.[179]

Material	$d_{(100)}$ / (nm)	Surface area / ($m^2\ g^{-1}$)	Pore volume / ($cm^3\ g^{-1}$)	Micropore / ($cm^3\ g^{-1}$)
mRO-1	4.7	-	-	-
mRO-2	3.5	263	0.20	0.07
mRO-3	3.5	190	0.12	0

The common self-assembly mechanisms invoked when cationic surfactants are used include direct S^+I^- or indirect $S^+X^-I^+$ pathways [181,189,190]. The direct S^+I^- pathway involves the co-condensation of anionic inorganic species with a cationic surfactant, as in the synthesis of MCM-41 [180]. In the indirect $S^+X^-I^+$ pathway, the organic-inorganic self-assembly is mediated by negatively charged ions (usually chloride or bromide) [181,189,190]. In the present case, the chemical analysis for the initial surfactant-laden ruthenium mesostructure (**mRO-1**) measured by energy dispersive X-ray (EDX) spectroscopy indicates a chloride / $C_{16}TMA^+$ ratio close to 1. The FTIR spectrum of **mRO-1** shown in **Figure 3.6a** also reveals the presence of nitrosyl and hydroxyl species. The TGA of **mRO-1** using isothermal annealing at 200 ^oC (**Figure 3.6b**) shows that decomposition to RuO_2 (59 wt. %) occurs after 12 h. Hence we propose that the inorganic-organic self assembly is synthesized through an indirect $S^+X^-I^+$ pathway mediated by the chloride ion expressed as $C_{16}TMA^+$<Cl^->$Ru(NO)(OH)_x(H_2O)_y$ [191]. The slow decomposition and

release of nitric oxide is the source of micropores in the amorphous material. It is reported that MCM-41 formed in alkaline solution synthesized by a direct S^-T^+ pathway has no significant chloride contents using a similar surfactant, for example [181,189,190].

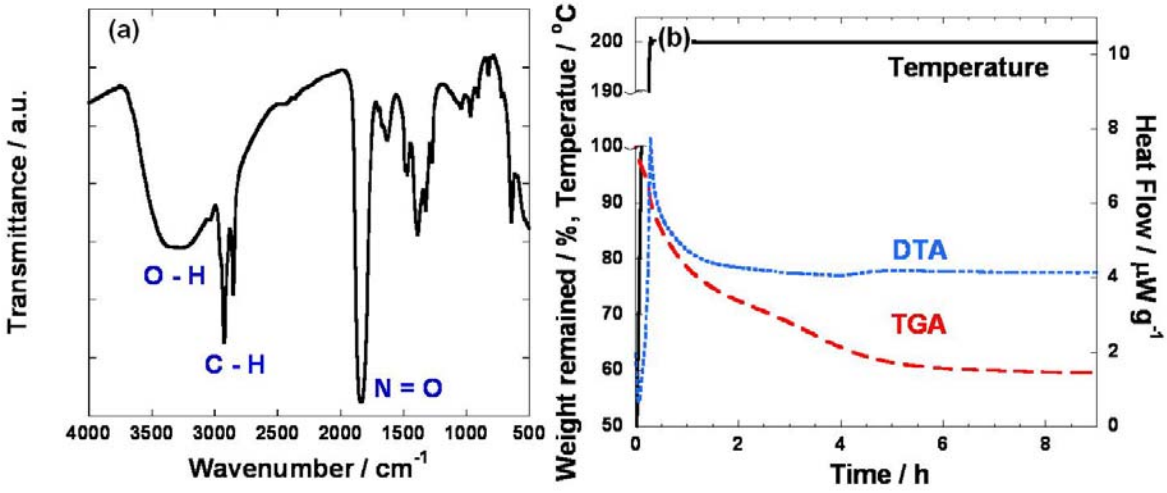

Figure 3.6 (a) FTIR spectrum of **mRO-1** showing the presence of hydroxyl, and nitrosyl functional groups.[179] The absorption at 1836 cm^{-1} is red-shifted compared to gaseous nitric oxide (1876 cm^{-1}) [192], ascribed to complexation of the mononitrosyl species to Ru (III). (b) TGA/DTA profiles of the ruthenium precipitate on isothermal annealing at 200 °C. The temperature was raised to 200 °C using a 10 °C min^{-1} rate. Decomposition was complete after 6 h at 200 °C.

3.2 Mesoporous lead ruthenate

3.2.1 Synthesis procedure

To prepare the templated, mesostructured crystalline lead ruthenate, 0.9000 g of 25 % (w/w) aqueous hexadecyl-trimethylammonium chloride (Fluka, $C_{16}TMA^+Cl^-$) solution, 3.3030 g of ruthenium(III) nitrosyl nitrate solution (1.53 wt. % Ru, Sigma-Aldrich), 0.1340 g of lead sub-acetate ($Pb(OAc)_2 \cdot 2Pb[OH]_2$) and 5.0 g of deionized water were mixed in a 20 mL PTFE container and stirred for 1 h at room temperature. The solution was transferred to

a 100 ^{o}C oven and stored for 3 h with bottle tightly sealed. In a separate bottle, 3.300 g of 2 M aqueous NaOH solution was prepared and poured dropwise into the reaction bottle with vigorous stirring immediately after it was taken out from the oven. The solution was stirred for 3 h at room temperature and then 0.47 ml of sodium hypochlorite solution (11.9 % active Cl, Sigma-Aldrich) was poured dropwise into the reaction bottle with vigorous stirring. The bottle was further stirred for additional 12 h with the bottle tightly sealed. The reaction mixture was then filtered and washed with copious amounts of deionized water and dried in vacuum oven at room temperature to yield typically 0.15 g of quasi-crystalline black power.

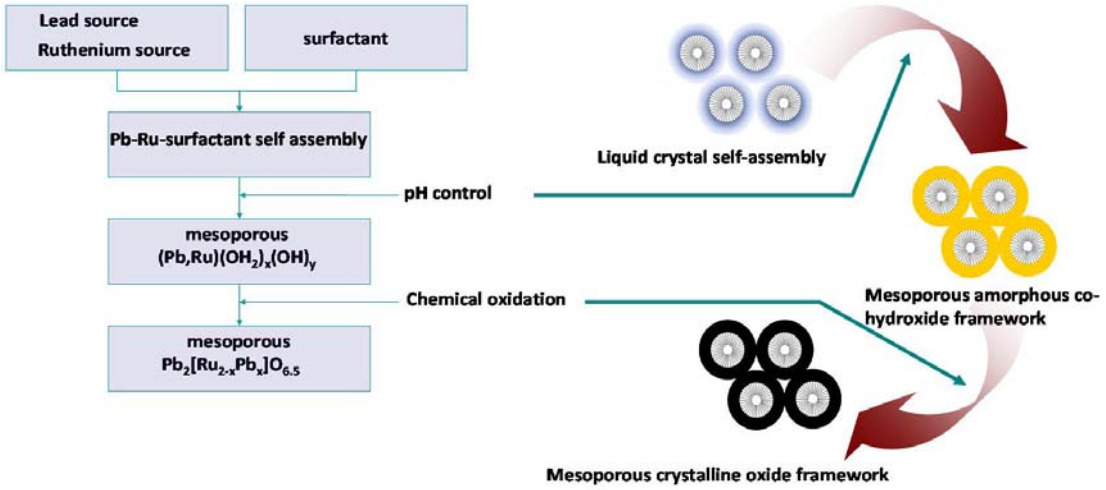

Figure 3.7 Schematic diagram for the synthetic procedure for mesoporous lead ruthenate pyrochlore. Chemical oxidation of self-assembled hydroxide framework leads to the mesostructured nano-crystalline oxide framework at room temperature.

For the preparation of mesoporous surfactant-lead ruthenium hydroxide nano-composite, sodium hypochlorite solution was not added to the reaction bottle. Instead it was heated in a convection oven for 12 h at 100 ^{o}C to obtain yellowish powder. The amorphous oxide can be prepared by adding 0.40 ml of sodium hypochlorite solution. More than 0.5 ml of sodium hypochlorite solution results in the crystalline growth and destruction of mesostructure. The

schematic diagram for overall synthesis procedure is shown in **Figure 3.7**, where the initial organic-inorganic self-assembly liquid crystal structure becomes mesostructured surfactant-hydroxide framework by pH adjustment and then converted into the oxide framework by further chemical oxidation and dehydration.

3.2.2 Characterization

The electronically-conducting lead ruthenate pyrochlore was conventionally considered as a cathodic catalyst for oxygen reduction in solid oxide fuel cells [145,146] and as a bifunctional catalyst for oxygen reduction /evolution in many metal-air cells [85,139]. In this thesis, we report the first successful synthesis of electronically-conducting mesoporous lead ruthenate pyrochlore oxide network and the oxygen reduction / evolution characteristics as a lithium oxygen cell cathode catalyst. So far only few studies about solution-based in situ crystallization of the initial amorphous mesoporous network have been reported with the exception of zeolite structure, where the organic templating results in an ordered metal-organic framework directly [193,194]. In most other cases, the decomposition of the initial amorphous framework by heat treatment at elevated temperature in an effort to crystallize the product often results in the collapse of pore structure either by the decomposition of initial precursors or by crystallite growth. To figure this out, hard templates like silica [98] or carbon [195] are often employed so that these sturdy templates can withstand the structural stress and strain developed during the heat-treatment. However, the reactivity of the initial precursors with the template structure during synthesis (silicate or carbide formation), the cumbersome process of etching the template, and the difficulty in nano-casting the

precursors into the mesopores of the template repeatedly, all limit the use of this method. But in this work, we adopted a fundamentally different approach to crystallize the initial amorphous hydroxide framework using the oxidizing agent, sodium hypochlorite, NaOCl to increase the oxidation state of the transition metal, hence, to catalyze the condensation reaction from the initial poor crystalline hydroxide precursors, eventually resulting in the crystalline material while the original surfactant structure is still present. The organic framework which holds the mesostructure during the development of crystallinity can be easily removed by solvent extraction or by decomposition at mild temperature.

The mesoporous framework was built by adopting liquid crystal templating in an aqueous solution using the cationic surfactant, hexadecyl-trimethyammonium chloride, $C_{16}TMA^+$ Cl^- and subsequent condensation and in situ crystallization by means of the concentrated sodium hypochlorite solution. The condensation triggered by the increase in average oxidation state of ruthenium catalyzes the initial hydroxo-bridges to be converted to oxo-bridges between transition metals [196]. Formal charge increase in transition metals strongly polarizes oxygen atoms coordinated around them, and thus destabilizes the O-H bond, leaving the partial charge of $\delta(H_2O)$ at a more positive value. Considering ruthenium hydroxide alone, the partial charge $\delta(H_2O)$ increases from 0.088 to 0.153 when the ruthenium formal oxidation state changes from +3 to +4.5, where the hydroxide form is very unstable due to the increased average electronegativity. The condensation process ends with the hydroxo ligand catching one acidic hydrogen atom to form a water molecule and leave the structure.

$$2(Pb \cdot Ru^{3+})(OH)_5 + 1.5OCl^- \rightarrow Pb_2Ru_2{}^{4.5+}O_{6.5} + 1.5Cl^- + 5H_2O \qquad (3\text{-}1)$$

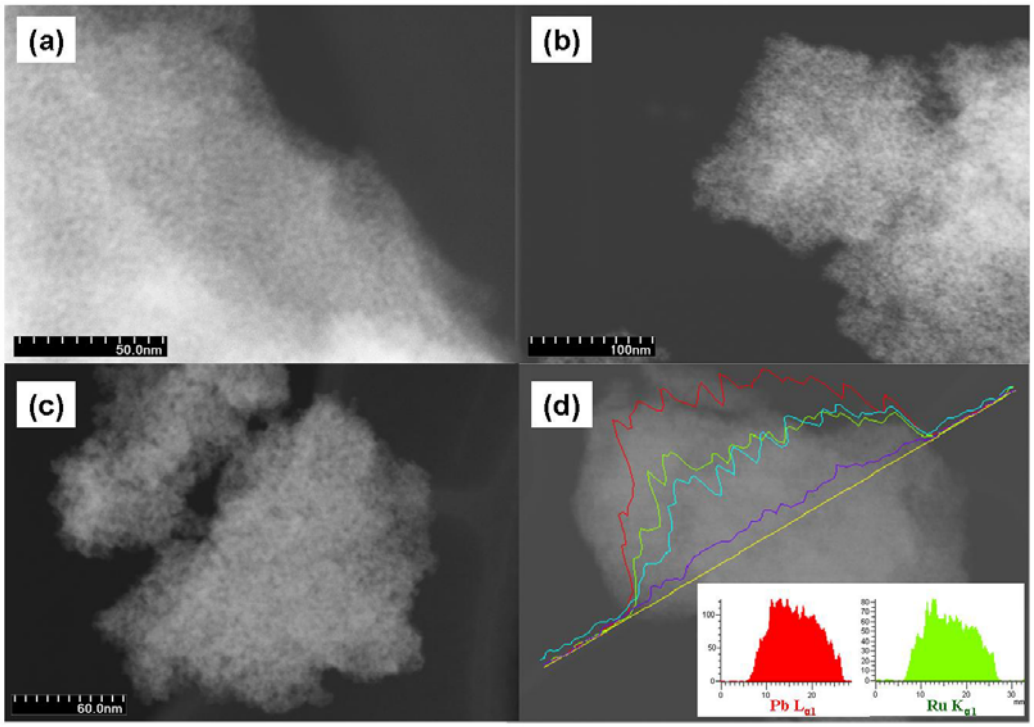

Figure 3.8 TEM images for (a) mesostructured surfactant-templated lead ruthenate co-hydroxide, (b) crystalline lead ruthenate with surfactant present in the pore and (c) surfactant free pyrochlore (d) EDX analysis for crystalline material showing lead-rich character of the synthesized material.

The resulting mesoporous network of the initial amorphous hydroxide material and the final crystalline oxide is shown in **Figure 3.8a-8d**. The amorphous hydroxide (**Figure 3.8a**) shows the well-connected three dimensional disordered pore networks with a uniform wall and surfactant-filled channels of rather spherical pore shape. The crystallized samples (**Figure 3.8b, c**) certainly well maintain the initial porous structure where the nano-crystallite is thought be of the size of wall thickness, while surfactant removed pyrochlore (**Figure 3.8c**) shows much disordered, but still a distinct porous structure. The EDX line scanning on the possible chemical elements for the sample with crystallized wall in **Figure 3.8d** indicates that lead contents in the sample are much higher than ruthenium. The lead enriched pyrochlore is a common product when lead ruthenate is synthesized by low

temperature solution-based method as a result of cation mixing. In other words, some of the lead cations reside on the ruthenium site with a higher oxidation state of Pb^{4+}. The lead ion in its original site exists as Pb^{2+}. The smaller diameter of Pb^{4+} makes it fit into the Ru^{4+} site, which is much smaller than Pb^{2+}.

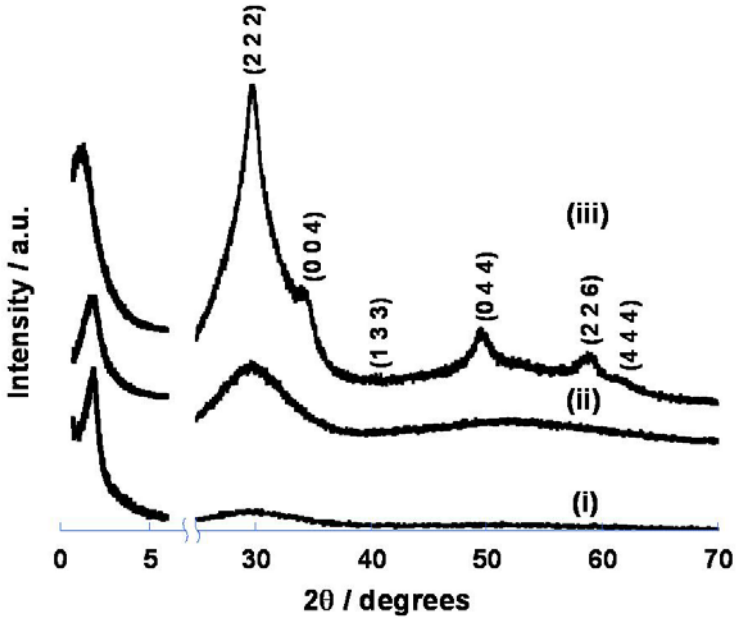

Figure 3.9 Low angle and wide angle X-ray diffraction patterns for (i) mesostructured surfactant-templated lead ruthenate co-hydroxide framework, (ii) amorphous mesostructured lead ruthenate and (iii) crystalline mesostructured lead ruthenate. Interestingly, the meso-dimension increases after chemical oxidation as evidenced by shift to lower angle of lone peak in low angle diffraction. This is probably caused by repulsive interaction between surfactant and oxide structure.

The low angle X-ray diffraction pattern for the initial hydroxide (**Figure 3.9**) shows one amorphous peak at around $2\theta = 1.89^{o}$, where unit mesophase dimension is around 4.7 nm. The locally uniform wall and channel structures develop a single amorphous peak. The crystallized pyrochlore shows the increased mesophase dimension about 7.3 nm ($2\theta = 1.21$). This probably comes from the fact that the inter-molecular force balance between the initial hydroxide and surfactant was intervened by the increased formal charge of the transition metal, resulting in the increased channel size for oxide material. The wide angle X-ray

diffraction pattern for the crystallized pyrochlore shows very broad patterns reflecting nano-sized character of the crystallite, but clearly shows most of the reflections for the Fd-3m space group. The lattice parameter, ***a***, from the (222) reflection is calculated to be 10.380 Å, which is substantially greater than the reported value 10.252 Å for the stoichiometric compound ($Pb_2Ru_2O_{6.5}$) [138,142]. This increase is unequivocally caused by the considerable substitution of lead into ruthenium site, which is common phenomenon when this material is prepared through a low temperature solution route [138,141]. This lead in ruthenium site is considered to be tetravalent and the ionic radius of Pb^{4+}(0.775 Å) is much greater than Ru^{4+}(0.62 Å) resulting in the increase in the lattice parameter. The extent of substitution, x, in $Pb_2[Ru_{2-x}Pb_x]O_{6.5}$ was estimated to be ~0.4 in comparison with the value in the literature [138], in which a well established correlation exists between the lattice parameter and the extent of substitution, and this will be more discussed in **Section 3.3.2**. Therefore, the composition of the mesoporous pyrochlore is approximately written as $Pb_2[Ru_{1.6}Pb_{0.4}]O_{6.5}$. The elemental analysis by the Energy Dispersive X-ray spectroscopy (EDX) measurement for the mesoporous powder sample (**Figure 3.8d**) indicates that the ratio between Pb/Ru is close to 1.58, which is in a reasonable agreement with the value predicted by lattice parameter expansion from the X-ray diffraction. The surfactant existing in the framework was easily removed by simply stirring powder in the absolute ethanol for 2 h, which reflects the weakened interaction between surfactant and oxide framework. The thermogravimetric (TGA) and differential thermal analysis (DTA) in **Figure 3.10a** show that most of the surfactant was removed by extraction in ethanol as the intensive exothermal peak in DTA curve and weight loss in TGA curve around 200 ^oC nearly disappears in the ethanol-treated sample. Certainly, the extraction was accompanied by partial collapse of the

mesoporous oxide framework as evidenced by the suppression of the single peak in the low angle X-ray diffraction pattern in **Figure 3.10b**, and more disordered pore structure observed in TEM image in **Figure 3.8c**.

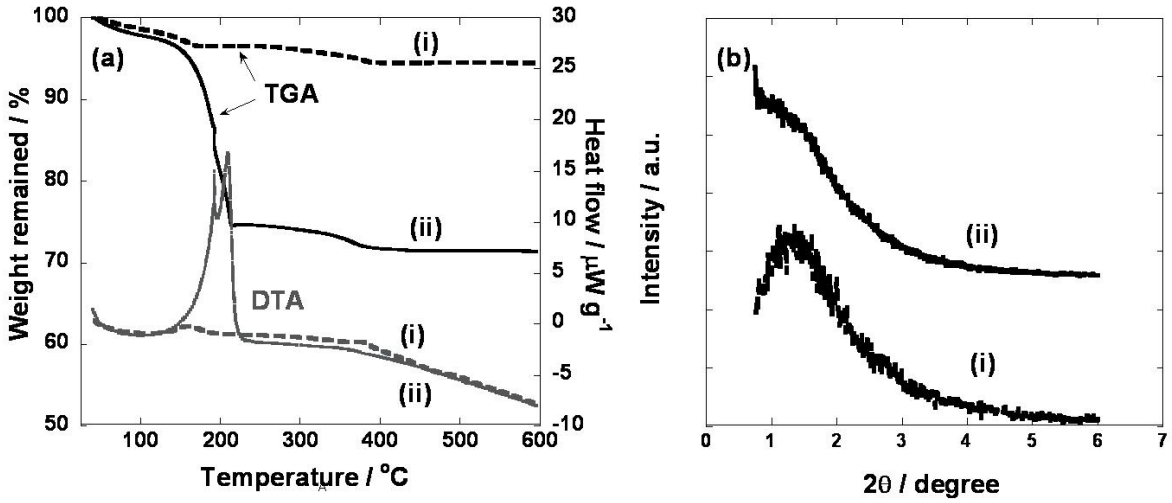

Figure 3.10 (a) Thermogravimetric (TGA) and differential thermal analysis (DTA) curves (i) for the crystalline lead ruthenate pyrochlore containing surfactant and (ii) for the sample after removing surfactant by ethanol treatment and (b) their low angle X-ray diffraction patterns. Most of surfactant is removed from the extraction by ethanol but result in the distortion and the partial collapse of pore structure.

The further increase in the NaOCl amount results in the substantial crystalline growth and the complete destruction of porous structure as described in the sharp X-ray diffraction pattern in **Figure 3.11.** The weight loss in TGA around 300 ~ 400 ^{o}C is ascribed to the decomposition of the expanded pyrochlore structure into lead dioxide and stoichiometric pyrochlore structure, and subsequent decomposition of lead dioxide because the expanded structure is not stable in the high temperature due to the intrinsic instability of tetravalent lead at the high temperature [138,197].

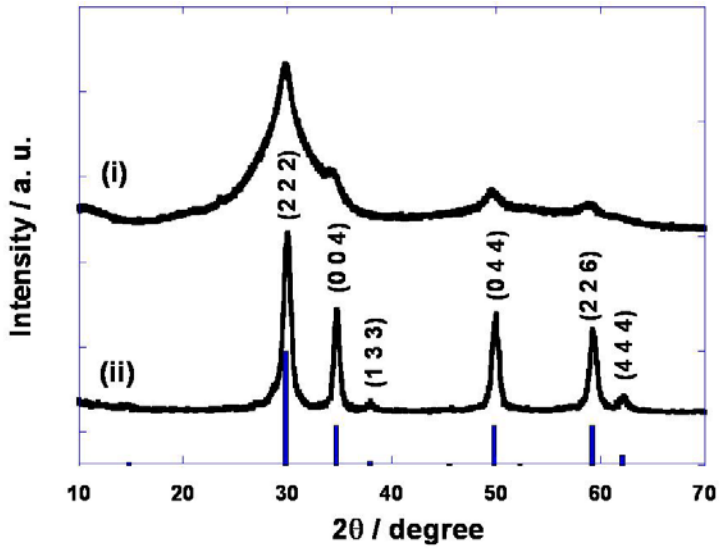

Figure 3.11 The X-ray diffraction patterns for (i) mesoporous crystalline lead ruthenate pyrochlore and (ii) lead ruthenate pyrochlore when an excess amount of oxidizing agent is used. A crystalline growth occurs upon more oxidizing agent. Solid lines are from the reported powder diffraction for the extended pyrochlore $Pb_2[Ru1_{.69}Pb_{0.31}]O_{6.5}$ for comparison.

The nitrogen isotherm of the crystalline pyrochlore, surfactant of which is removed by ethanol extraction, was shown in **Figure 3.12**. The typical type IV isotherm with hysteresis type 2 was observed [169], which is the common isotherm for spherical mesopore morphology. The BET surface area was measured about 149.0 m^2/g, which is the largest surface area ever reported for the crystalline pyrochlore to the best of our knowledge and the pore volume is calculated to be about 0.13 cm^3/g. The pore size distribution was calculated based on the Barett-Joyner-Halenda (BJH) algorithm, which shows the pore size is centered at 5.6 nm. The type 2 hysteresis implies that pore blocking and percolation occurs during the desorption process meaning larger spherical pore shown in TEM picture (**Figure 3.8c**) is connected with channels of smaller pore diameter. Considering the meso-dimension of crystalline material is around 7.3 nm, the wall is considered to be made up of a few unit cells of pyrochlore, which can be also inferred from the wide angle X-ray diffraction pattern **(iii)** in **Figure 3.9**.

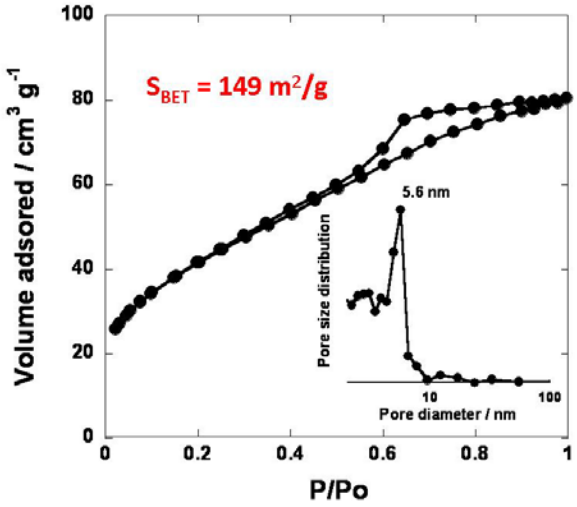

Figure 3.12 Nitrogen sorption isotherm for the surfactant-free mesoporous crystalline lead ruthenate pyrochlores and the corresponding BJH pore size distribution from the desorption branch. Type IV isotherm with H2 hysteresis is observed which is commonly observed for spherical pore shape.

Physical parameters of mesostructured crystalline lead ruthenate pyrochlore and other related materials estimated from X-ray diffraction patterns and N_2 sorption isotherm measurements are summarized in **Table 3.2**.

Table 3.2 Physical properties of mesoporous lead ruthenate amorphous and crystalline pyrochlore and hydroxide precursor.

Materials	d spacing [nm]	Surface area [m^2/g]	Pore size [nm]
amorphous lead ruthenium hydroxide	4.7	-	-
amorphous lead ruthenate	4.7	-	-
crystalline lead ruthenate pyrochlore	7.3	150	5.7

The resistivity of surfactant-free mesoporous lead ruthenate pyrochlore framework was measured by a four-point probes method, and found to be 4.6×10^{-2} Ω·cm at room temperature. The resistivity of the expanded lead ruthenate with a similar composition from

the literature is approximately 5.0 x 10^{-3} Ω·cm [141]. But considering the nano-scale wall structure, surfactant remnants, and less developed crystallinity of the mesoporous material, the value is quite reasonable. In fact, the resistivity of other mesoporous metallic oxide reported in the literature is at least several orders higher than the current value [198,199]. The resistivity of lead ruthenate extended pyrochlore critically depends on the extent of substitution, because as the extent of substitution increases, pyrochlore starts to show the transition from metal-like to semiconducting-like behavior. When *x* is around 0.4, lead ruthenate exhibits almost temperature-independent resistivity. It is believed that Ru_2O_6 framework made of corner-sharing RuO_6 octahedra provides a conduction path for electrons where Pb-substitution on ruthenium site generates thermally activated percolation of electrons among the connected RuO_6. In the amorphous material, conductivity is mostly governed by short-range ordered structure and disordering in cationic sites, which give much higher resistivity compared with its crystalline counterpart. The poor crystallinity and the defective structure of mesoporous pyrochlore lead to substantially higher resistivity.

3.3 Nano-crystalline lead ruthenate and bismuth ruthenate

3.3.1 Synthesis procedure

For the synthesis of nano-crystalline lead ruthenate, a similar procedure which was used for the synthesis of mesoporous lead ruthenate was followed except that the entire process was performed at room temperature without surfactant. Typically 3.3030 g of ruthenium(III) nitrosyl nitrate solution (1.53 wt. % Ru, Sigma-Aldrich), 0.1340 g of lead sub-acetate ($Pb(OAc)_2 \cdot 2Pb[OH]_2$) and 6.0 g of deionized water were mixed in a 20 mL

container, and stirred for 1 h at room temperature. In a separate bottle, 3.3000 g of 2 M aqueous NaOH solution was prepared and poured dropwise into the reaction bottle with constant stirring to obtain a clear dark purple solution. The solution was stirred for 3 h at room temperature, and then 0.50 ml of sodium hypochlorite solution (11.9 % active Cl, Sigma-Aldrich) was poured dropwise into the reaction bottle with vigorous stirring. The bottle was further stirred for an additional 24 h with the bottle tightly sealed. The reaction mixture was then filtered and washed thoroughly with copious amounts of deionized water, and the resultant black powder was dried in vacuum oven at room temperature to yield typically 0.15 g of crystalline product.

For the synthesis of nano-crystalline bismuth ruthenate, 0.2425 g of bismuth(III) nitrate pentahydrate and 3.3030 g of ruthenium(III) nitrosyl nitrate solution were dissolved in 1.0000 g of water to form a clear solution by adding 0.4000 g of concentrated (68 wt. %) nitric acid solution. Then, 10.0000 g of 2 M NaOH solution was slowly added to the precursor solution while stirring to form a solid precipitate, which was kept in 60 ^{o}C oven for 3h. Next, 0.50 ml of NaOCl was poured dropwise into the reaction bottle with vigorous stirring. The bottle was further stirred at 70 ^{o}C for additional 24 h with the bottle tightly sealed. The reaction mixture was then filtered and washed with plenty of water, and dried in vacuum oven at room temperature.

According to the literature, the point of zero charge for lead ruthenate $Pb_2Ru_2O_{6.5}$ is pH 10.74 [137]. It implies that in the strong alkaline solution such as synthetic condition in this thesis, its surface, especially oxygen vacancy site on the surface is filled with deprotonated water, and lead ruthenate particles take on negative charges. During the synthesis, this negative surface charge attracts considerable amount of sodium ions in the

water due to its high surface area. Thus, the washing process should be done thoroughly enough for water molecules to replace hydroxide ions in the vacancy sites and remove these surface adsorbed sodium ions.

3.3.2 Characterization

The X-ray diffraction patterns for the synthesized materials in **Figure 3.13** exhibit the formation of nano-crystalline pyrochlores with space group Fd3-m with lattice parameter ***a*** = 10.340 Å for lead ruthenate and ***a*** = 10.378 Å for bismuth ruthenate. The crystallite size from the peak broadening through [111] directions shows the coherent length is about 4 nm along that direction for both materials.

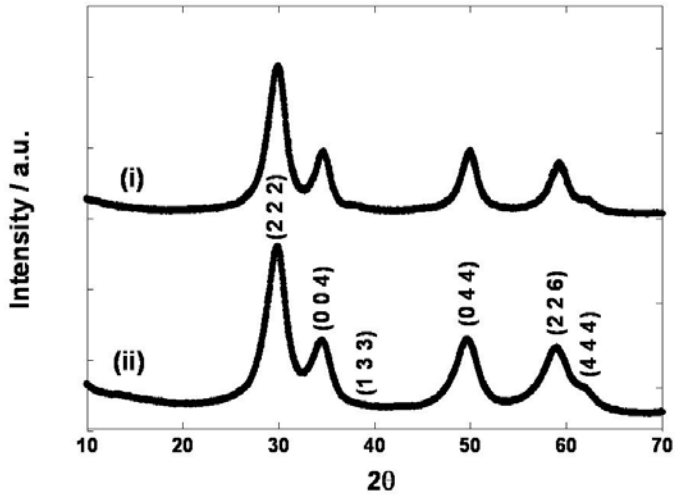

Figure 3.13 X-ray diffraction patterns for (i) nano-crystalline lead ruthenate and (ii) nano-crystalline bismuth ruthenate pyrochlore. The broad X-ray diffraction peaks represent nano-crystallite character.

For the lead ruthenate, the whole synthetic process was carried out at room temperature to obtain a single crystalline phase, whereas bismuth ruthenate pyrochlore needs an elevated

temperature (70 ^{o}C) to initiate the crystallization process. The nano-crystalline character of less than 10 nm size is also evident from the TEM images (**Figure 3.14a-d**), which show agglomerated polycrystalline particles with nanocrystallite domains.

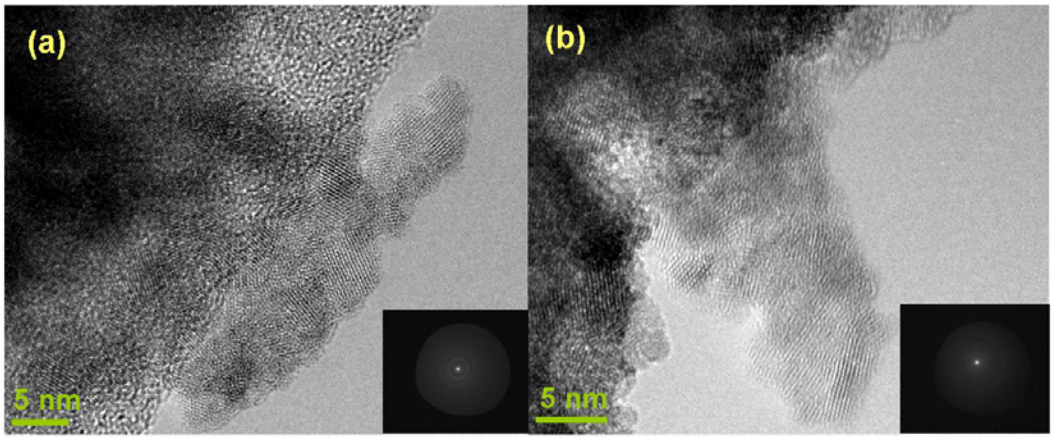

Figure 3.14 TEM images for nano-crystalline (< 10 nm) (a) lead ruthenate and (b) bismuth ruthenate pyrochlore with electron diffraction patterns, which exhibit polycrystalline character.

These pyrochlores also showed an increase in the lattice parameter, ***a***, compared with stoichiometric compounds as B-site substitution of noble metal with post transition metal is expected from the low-temperature synthesis method for these materials [138,141]. The extent of substitution was readily estimated from the empirical formula based on Vegard's law. For lead ruthenate $Pb_2[Ru_{2-x}Pb_x]O_{6.5}$ it is given by $y(Å) = 10.25 + 0.33\ x$, and in the case of bismuth ruthenate $Bi_2[Ru_{2-x}Bi_x]O_{7-\delta}$, $y(Å) = 10.30 + 0.31x$ [138]. From the above equations, the compositions of pyrochlores are determined to be $Pb_2[Ru_{1.73}Pb_{0.27}]O_{6.5}$ and $Bi_2[Ru_{1.74}Bi_{0.26}]O_{7-\delta}$. The EDX analysis on the powder samples, however, shows that the ratios of Pb / Ru and Bi / Ru are actually 1.24 and 1.17, respectively (**Table 3.3**), which is a little lower than the values predicted from the lattice parameters calculated from X-ray diffraction patterns, 1.31 and 1.30 respectively. This implies that a small amount of

amorphous ruthenium oxide phase may exist. It is verified that without the presence of lead or bismuth ions, the above procedure results in amorphous ruthenium oxide.

Table 3.3 Composition of lead and bismuth ruthenate pyrochlores analyzed by lattice parameters calculated from XRD patterns and Pb/Ru and Bi/Ru ratio from EDX analysis**.**

Materials	Composition from XRD analysis	Ratio Pb/Ru or Bi/Ru from XRD	Pb/Ru or Bi/Ru ratio from EDX
mesoporous lead ruthenate	$Pb_2[Ru_{1.6}Pb_{0.4}]O_{6.5}$	1.50	1.58
nano-crystalline lead ruthenate	$Pb_2[Ru_{1.73}Pb_{0.27}]O_{6.5}$	1.31	1.24
nano-crystalline bismuth ruthenate	$Bi_2[Ru_{1.74}Bi_{0.26}]O_{7-\delta}$	1.30	1.23

The surface area of these materials was measured from the adsorption curve of the nitrogen sorption isotherm (**Figure 3.15a, b**). The surface areas of lead ruthenate and bismuth ruthenate are about 66 $m^2 g^{-1}$ and 103 $m^2 g^{-1}$, respectively, which reflect the nano-crystalline character, and these large surface areas are beneficial for maximizing the catalytic effect.

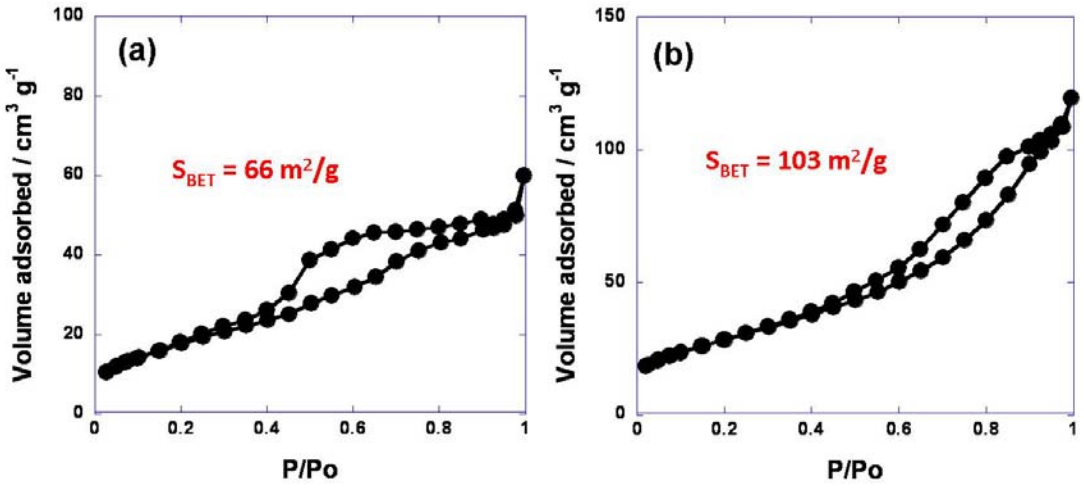

Figure 3.15 Nitrogen sorption isotherms for (a) nano-crystalline lead ruthenate and (b) nano-crystalline bismuth ruthenate pyrochlores with corresponding surface area from BET plot method.

3.4 Lead ruthenate / Ketjen Black nano-composite

The lead ruthenate nano-particles with extended pyrochlore structures were deposited on the amorphous carbon (Ketjen Black, KB) through oxidizing metal precursors in oxygen-saturated aqueous alkaline solution at elevated temperature. The procedure is based on the method previously reported [138,139,141,143] with several modifications. First, in order to introduce a hydrophilic moiety on the amorphous carbon surface (surface area: 1416 m^2 g^{-1}), 0.400 g of carbon was dispersed in 10 mL of deionized water to which 0.5 mL of sodium hypochlorite (11.9 % active Cl, Sigma-Aldrich) was added [200]. The mixture was stirred for 15 min at room temperature, and quickly filtered to prevent the excessive oxidation of the surface. The resulting carbon was dried at 100 ^oC in an oven. The precursor solution for lead ruthenate was prepared by mixing 1.3212 g of ruthenium(III) nitrosyl nitrate solution (1.53 wt. % Ru, Sigma-Aldrich), 0.0536 g of lead sub-acetate ($Pb(OAc)_2 \cdot 2Pb[OH]_2$) in 8.0 g of deionized water to which 3.0 mL of 2 M NaOH solution was added to obtain a dark purple solution. This precursor solution was poured into Teflon reactor containing 0.180 mg of amorphous carbon. The reactor was placed at 70 ^oC in the oven for 24 h while being stirred vigorously under constant 1 atm oxygen atmosphere, which is fed to the solution through a gas bubbler. After cooled down, the black reaction product, which was submerged under transparent solution was filtered and washed thoroughly with plenty of distilled water. After being dried at 100 ^oC in the hot oven, typically around 250 mg of powdered sample was obtained.

Figure 3.16a-d shows the SEM images for the original Ketjen Black (KB), surface-treated KB, 30 wt. % and 50 wt. % (targeted composition) lead ruthenate coated KB powders.

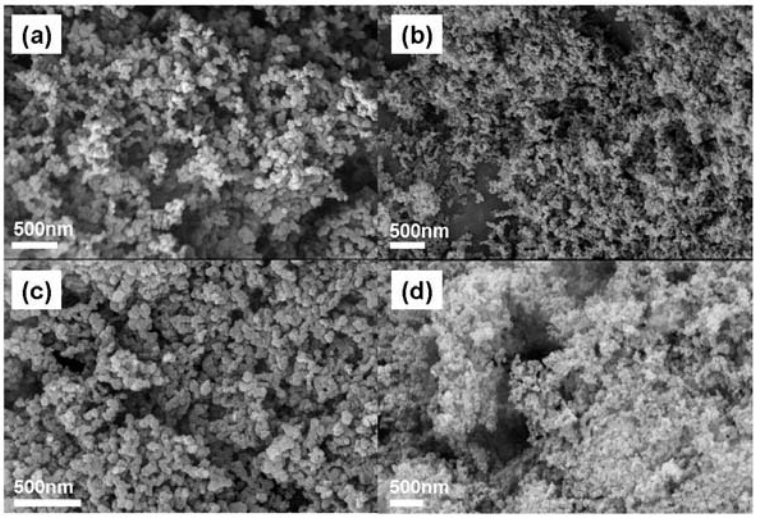

Figure 3.16 SEM images for (a) original Ketjen Black (KB) (b) surface-treated KB (c) 30 wt. % lead ruthenate coated KB and (d) 50 wt. % lead ruthenate coated KB.

Even after surface treatment and significant amount of metal oxide coatings, the original morphology of KB is well maintained, which shows spherical particles of around 40 nm size. This implies that lead ruthenate particles on the carbon surface are nano-sized and well-dispersed. These nano-sized metal oxide coatings were clearly visible in the TEM images shown in **Figure 3.17a, b** where the lead ruthenate nano-particles less than 10 nm are homogenously distributed all around KB surface.

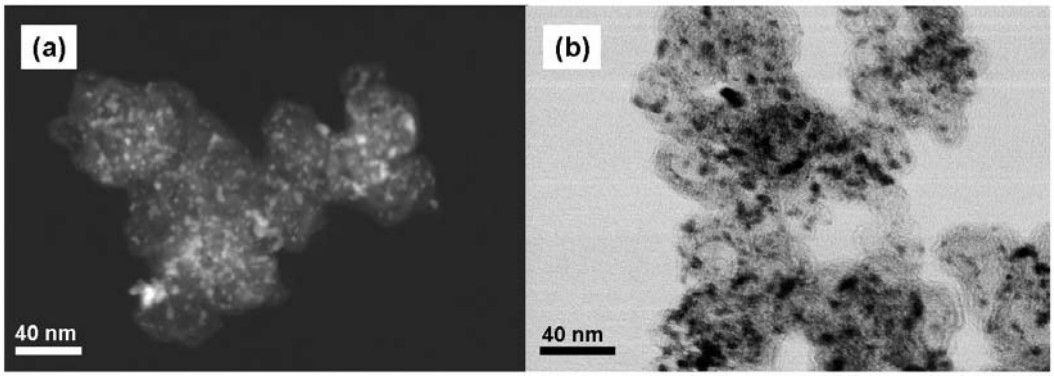

Figure 3.17 TEM images for 30 wt. % lead ruthenate coated KB; (a) dark field and (b) bright field images. The images show that nano-sized lead ruthenate particles are homogenously coated on the carbon.

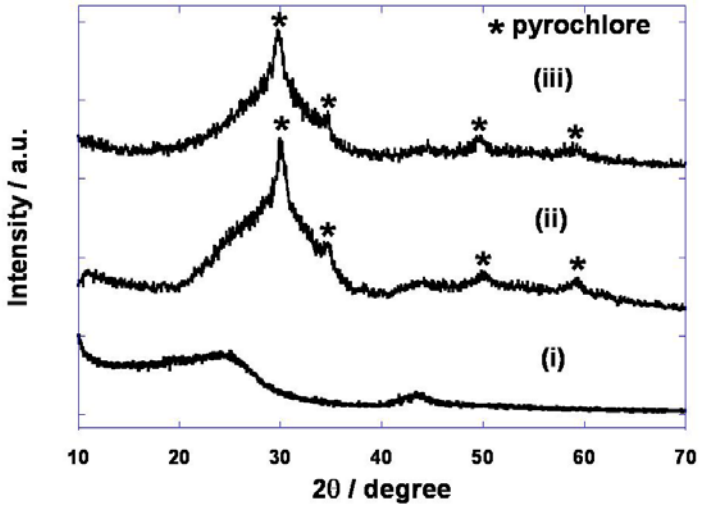

Figure 3.18 X-ray diffraction patterns for (i) Ketjen Black (KB), (ii) 30 wt. % lead ruthenate coated KB and (iii) 50 wt. % lead ruthenate coated KB. The mark * represents reflections from crystalline lead ruthenate pyrochlore.

The X-ray diffraction patterns for lead ruthenate coated KB in **Figure 3.18** further confirm the formation of nano-crystalline lead ruthenate phase in both 30 % and 50 % metal oxide coated samples. The thermogravimetric and differential thermal analysis (TGA-DTA) for the metal oxide coated sample under air was performed to evaluate the amount of lead ruthenate deposited on the carbon (**Figure 3.19**). The decomposition of carbon around 300 ^{o}C leaves only lead ruthenate where the amount of metal oxide is estimated. The actual contents of metal oxide in two samples from TGA curves are 29.3 wt. % and 46.8 wt. %. Considering a small loss of lead oxide contents during the TGA measurement by the decomposition of extended pyrochlore structure [138], the real composition of composite is considered to be very close to the targeted ones.

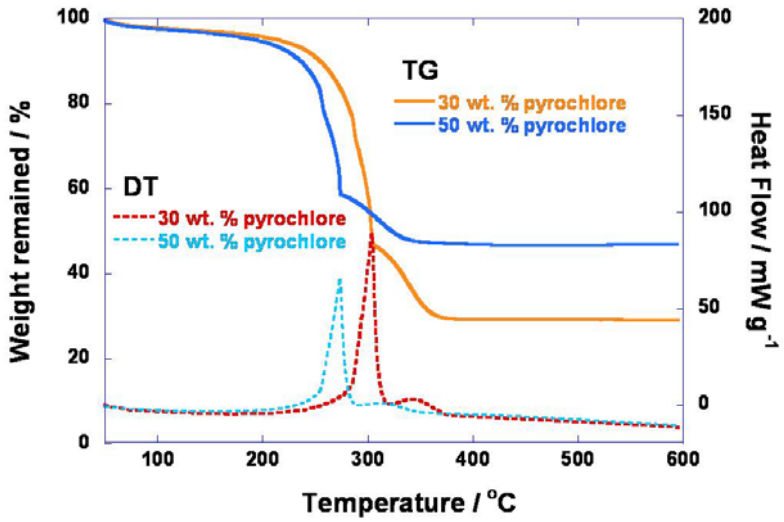

Figure 3.19 Thermogravimetric and differential thermal analyses (TGA/DTA) for lead ruthenate coated Ketjen Black carried out under air to estimate the amount of catalyst**.**

3.5 Gold-decorated metal oxide

The gold-decorated lead ruthenate was prepared by the spontaneous reduction of $HAuCl_4 \cdot 3H_2O$ (Aldrich) precursor in the aqueous solution on the surface of nano-crystalline lead ruthenate powders [201]. In a typical procedure, 50 mg of nano-crystalline lead ruthenate particles were suspended in 10 mL of water with vigorous stirring and the solution pH was adjusted to 9.0 by adding 0.2 M $(NH_4)_2CO_3$ solution slowly. Then, 10 mL gold precursor solution containing 0.01 M chloroauric acid was added drop by drop to the above solution containing lead ruthenate with vigorous stirring. The solution was further aged for additional one hour with a stirring and then filtered, being washed thoroughly with deionized water, and then dried at 100 ^oC in the oven. It is estimated that approximately 26 wt. % of gold was deposited on the pyrochlore surface by following the above procedure.

Gold-decorated silica was manufactured in much the same way with the gold-decorated lead ruthenate. In this case, 70 mg of spherical silica bead (0.5 μm, Alfa Aesar) was dispersed in 14 mL of deionized water and 14 mL of 0.01 M chloroauric acid was slowly added to the solution containing silica beads. All the other procedures are followed in the same way. In this way, approximately 26 wt. % of gold (estimated) was decorated on silica surface.

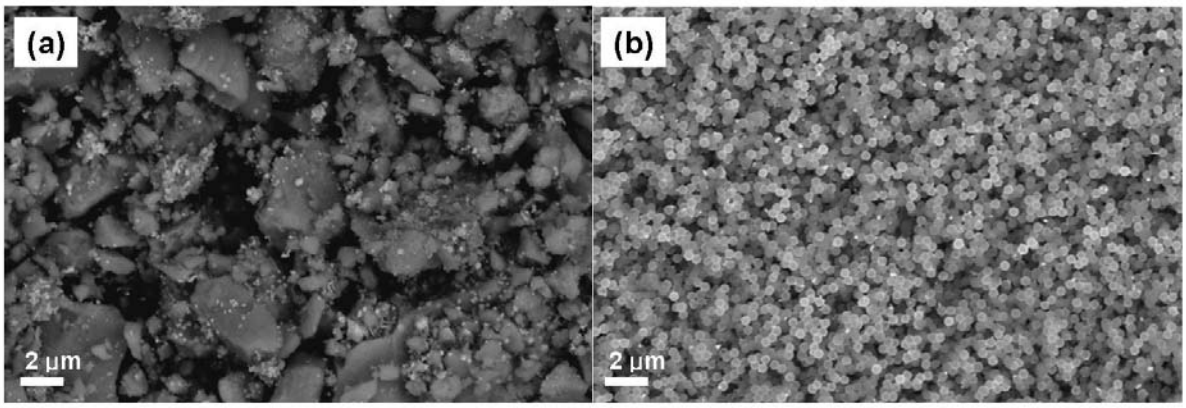

Figure 3.20 Gold depositions on metal oxide; (a) lead ruthenate pyrochlore (b) silicon dioxide

Figure 3.20a, b shows the SEM images of gold-decorated lead ruthenate and silica particles. They show gold particles (small bright spot) around ~100 nm are homogeneously mixed with lead ruthenate or silica particles. The Energy-dispersive X-ray spectroscopy (EDX) results on the elemental analysis exhibit that gold occupies 21 wt. % and 26 wt. % of total mass for the gold decorated lead ruthenate and the gold coated silica, respectively. In case of lead ruthenate, some agglomeration of the primary particles occurs during the deposition process. The X-ray diffraction patterns (**Figure 3.21**) show the existence of nano-crystalline gold phase in the mixture, and the reflections from gold are broader in case of silica, which means smaller gold phases are formed with silica.

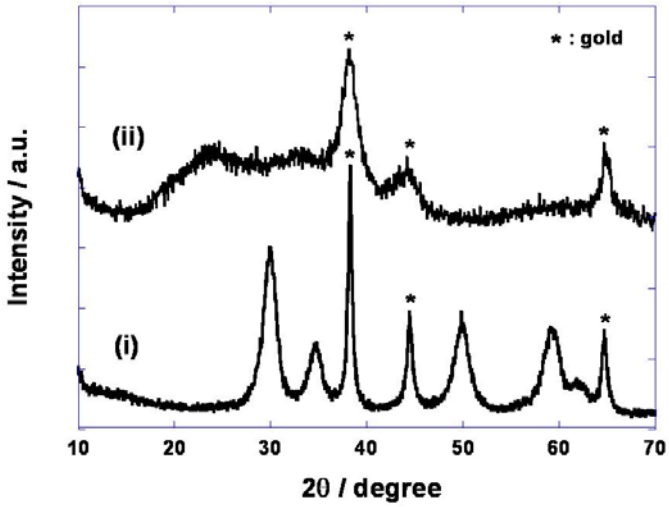

Figure 3.21 X-ray diffraction patterns for (i) gold-decorated pyrochlore and (ii) gold-decorated silica

3.6 Alpha-manganese dioxide nanowire

The α-MnO_2 nanowire, the structure of which resembles the mineral cryptomelane, was synthesized according to the literature method [202]. Typically 0.8 mmol $KMnO_4$ (0.1264 g) and 0.8 mmol NH_4Cl (0.0428 g) were dissolved in 40 mL of deionized water and stirred for 1 h at room temperature. Then, the solution was transferred to Teflon container (capacity: 60 mL) of hydrothermal reactor. The reactor was kept in static condition at 140 ^oC for 24 h in the oven. After cooled down, the reaction mixture was filtered and washed thoroughly with plenty of distilled water. The resulting brownish powder was dried at 100 ^oC in the oven.

Figure 3.22a shows the SEM image of α-MnO_2 nanowire exhibiting a typical nanowire shape with a diameter about 50 nm. **Figure 3.22b** shows the X-ray diffraction pattern of α-MnO_2, which exhibits a good agreement with reference data [202]. It belongs to

tetragonal space group I4/m with lattice parameter a = 9.78470, c = 2.86300 and shows no other phase than pure α-MnO_2 structure. Although it is not usually expressed explicitly, the actual composition of α-MnO_2 is considered to be $KMn^{4+}_6Mn^{2+}_2O_{16}$ [203] where potassium resides inside 2 × 2 tunnels made of edge- and corner-sharing MnO_6 octahedra (**Figure 3.23**), and stabilizes the overall tunneling structure.

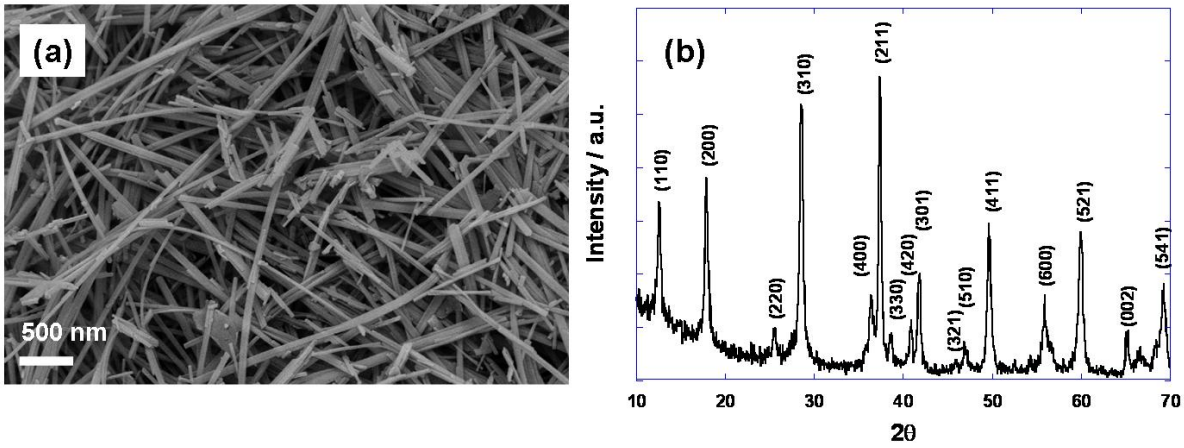

Figure 3.22 (a) SEM image and (b) X-ray diffraction pattern for α-MnO_2 nanowire

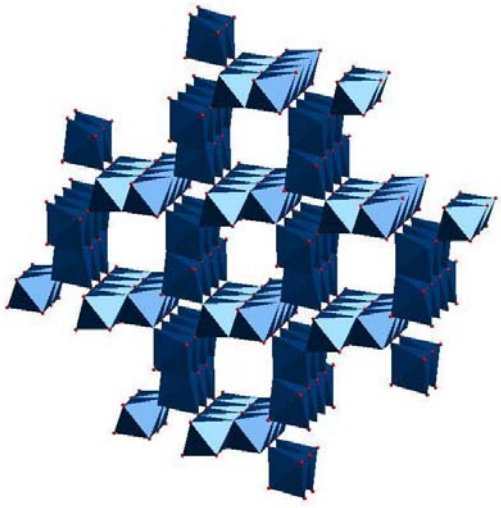

Figure 3.23 Crystal structure of α-MnO_2 showing 2 ×2 tunnel structure made of edge- and corner-sharing MnO_6 octahedra. It resembles the structure of mineral cryptomelane (KMn_8O_{16}).

IV. Li-oxygen Cell

4.1 Cell design and construction of cathode

A nano-porous, high surface area carbon structure with well dispersed catalyst and high pore volume is required to adopt insoluble reaction products on the cathode side and to facilitate oxygen and lithium ion diffusion to the reaction site through the cathode film as well as to promote the decomposition reaction of reaction product upon charge. This porous structure should be electronically well-percolated as well to provide electrons to the reaction site smoothly. Historically, a porous structure designed for similar objectives has been well developed in the construction of polymer-gel electrolyte and porous cathodes in lithium-polymer battery industry [204-207]. The key idea is the utilization of the conventional plasticizer like ethylene carbonate (EC), propylene carbonate (PC) or dibutyl phthalate (DBP) as a pore forming agent. These materials are put into the cathode mixture slurry containing high-surface area carbon, nanosized catalyst and binder during the manufacturing process forming well dispersed nano-scale lubricating emulsions between carbon and polymer binder mixtures in the solvent. After the mixture is printed in a thin film and dried, these plasticizers are conveniently removed by solvent extraction (typically ether) leaving a nano-scale pore structure in the film. The schematic diagram of such a film before and after ether treatment is shown in **Figure 4.1**. The solvent should dissolve the binder actively, and volatile enough to be dried quickly to generate a highly porous structure. A good dispersion for carbon and catalyst in the slurry is important as well. The speed of vaporization of the solvent during the drying process is considered as an important factor determining overall

pore volume of the film. The substrate or slurry is sometimes heated intentionally to promote a highly porous structure. The typical nominal porosity calculated just by the volume of plasticizers is about 4 cm^3 per gram of carbon. The coulombic capacity predicted from this porosity is just over 10,000 mAh g^{-1} assuming that all the pores are filled with lithium peroxide (density: 2.3 g/cm^3 [208-210]). But the actual porosity of the film is expected to be more than 4 cm^3 g^{-1} because a quick solvent evaporation leaves the additional porous structure as well as intrinsic micro-pores of carbon.

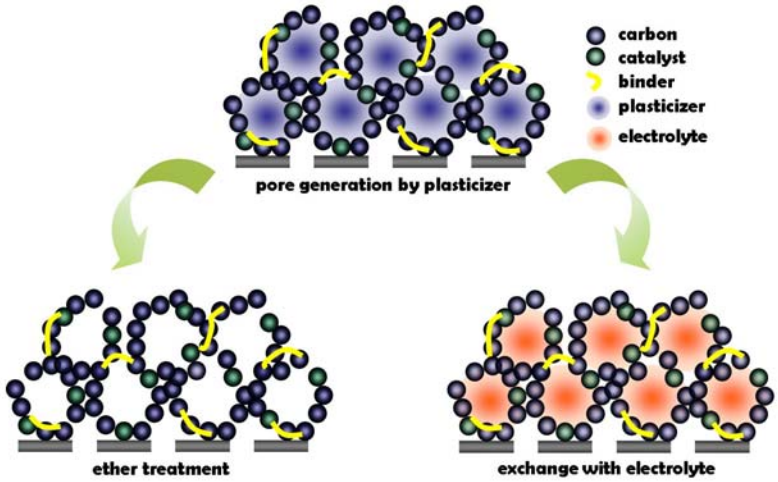

Figure 4.1 Manufacturing highly porous cathode using plasticizers and removal of plasticizer by ether treatment or plasticizer exchange with electrolyte solution.

Figure 4.2 shows the thermogravimetric (TGA) / differential thermal analysis (DTA) of cathode films conducted in N_2 atmosphere to confirm if the plasticizer is actually removed by ether treatment (ethyl ether, b.p. = 34.6 ^oC). For ether treated film, the weight remained virtually unchanged up to 300 ^oC where in another run the plasticizer volatilizes completely. The characteristic heat absorption signal for plasticizer also disappears in the ether treated electrode. Therefore, the ether-treatment is an efficient tool to remove plasticizers from the film.

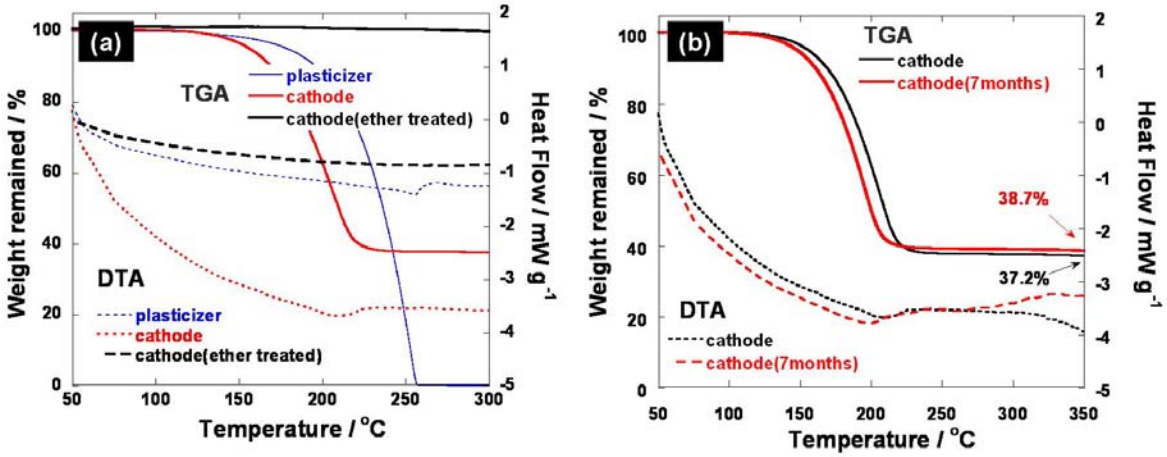

Figure 4.2 (a) TGA / DTA curves of cathode films before and after ether-treatment for confirming the removal of plasticizer. The weight of ether-treated electrode remains unchanged up to 300 ^{o}C, which suggest complete removal of plasticizers. (b) TGA / DTA curve of original cathodes film and the one stored for seven months. Even after 7 months, the cathode composition did not change much.

The amount of the plasticizer (DBP) present in the film is evaluated for the freshly manufactured film and the one stored for seven months to verify the composition (**Figure 4.2b**). The results show that the amount of plasticizer agrees accurately with the targeted composition of the film and there is just 2 % decrease in overall DBP amount even after 7 months, which shows the reliability of the film composition after long storage time. However, when PC is used as pore forming agent, the significant loss occurred in the electrode weight just in one day after it is manufactured. Thus, DBP is chosen as pore forming agent in this thesis.

The extraction of plasticizers from the cathodic film by ether treatment sometimes makes the film shrink too excessively as the counter tensile stress from the plasticizers is eliminated suddenly from the boundary between plasticizers and carbon. Although the refilling of the pores with electrolyte solution makes it recover to some extent, some destruction of the valuable original pore structure generated by plasticizer is inevitable. A

convenient way to solve this problem is to replace plasticizers by electrolyte solvent which is miscible with the plasticizers through solvent exchange process. The original cathodic film is soaked in the excess electrolyte solvent overnight for exchange at room temperature. **Figure 4.3** shows the TGA / DTA curves for before and after the exchange process when DBP is replaced by PC or tetraethylene glycol dimethyl ether (TEGDME). As the boiling point of PC (240 ^{o}C) or TEGDME (275 ^{o}C) is much lower than DBP (340 ^{o}C), PC or TEGDME volatilizes at much lower temperature. And PC or TEGDME in the cathodic film volatilizes at lower temperature than bulk solution due to the increased surface area. Most of DBP is considered to be replaced by the electrolyte solvent as the heat absorption signal for DBP disappears in the electrode exchanged by electrolyte solvent.

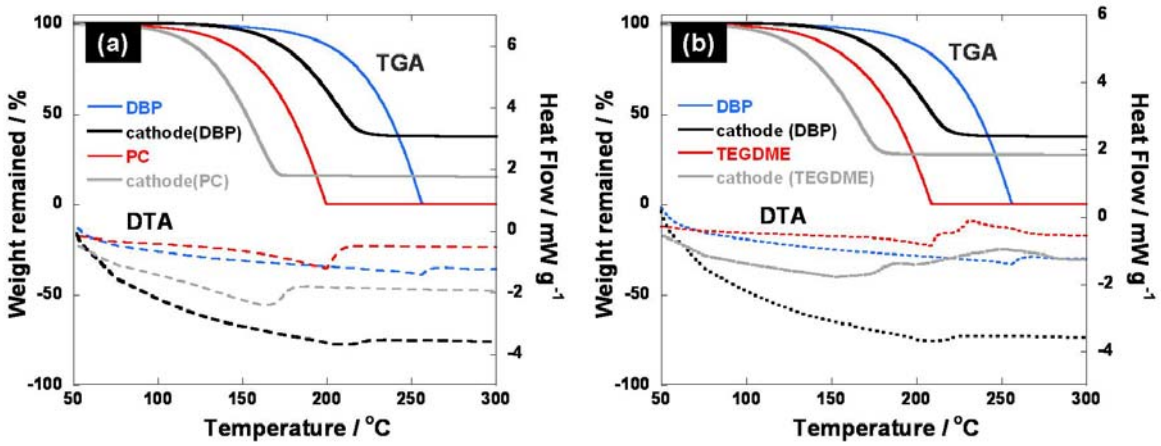

Figure 4.3 TGA/DTA curves for DBP exchange with electrolyte (a) propylene carbonate (PC) and tetraethylene glycol dimethyl ether (TEGDME)

A Swagelok® type cell was devised to evaluate Li-air cell performance (**Figure 4.4**). The inner surface of a bored-through half-inch union fitting was electronically insulated with a thin Kapton® film and PTFE ferrules. A half-inch stainless steel rod and aluminum tube were used as a current collector for anode and cathode, respectively. The aluminum tube on

cathode side is to be connected to the pressure-balanced chamber containing one atm oxygen gas to introduce oxygen gas to the cells. Inside the union fitting, circular form of lithium foil anode, glass wool separator, cathode assembly and aluminum ring were placed in turn together with the addition of appropriate amount of electrolyte solution. The cathode assembly was made by pressing the cathodic film gently on the aluminum mesh for better adhesion. The Swagelok® cells were assembled in an argon-filled glove box and then cells were connected to oxygen filled 500 mL pressure-balanced containers in another glove box filled with 1 atm pure oxygen. No further oxygen was supplied to the cells during the electrochemical experiment.

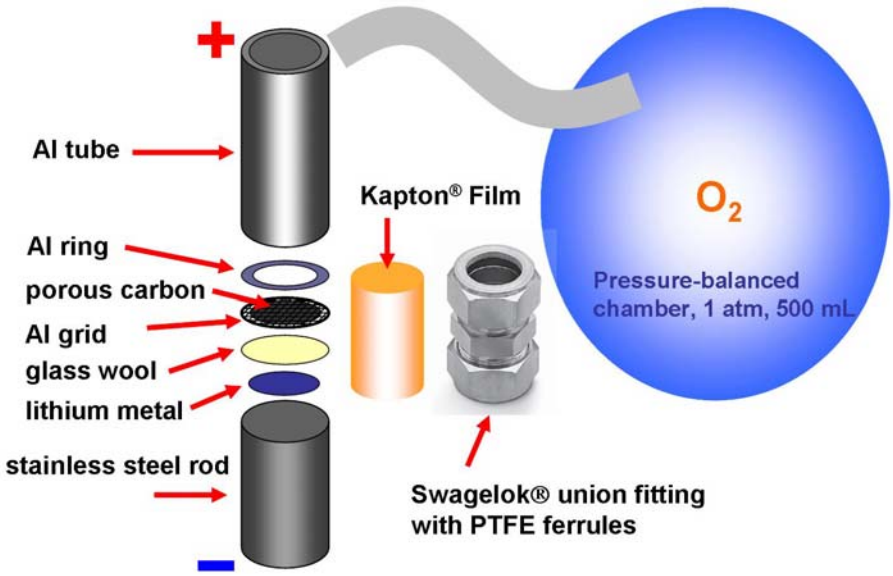

Figure 4.4 Design of Li-oxygen cell components and their assembly. Swagelok® cell is connected to pressure-balanced chamber containing 1 atm oxygen gas through aluminum tubes.

4.2 Electrochemistry of pyrochlore catalyst

The electrochemical behavior of lead ruthenate pyrochlore catalyst was investigated by a low scan rate (0.02 mV s^{-1}) potential sweep method in the voltage range of interest for the Li-oxygen cell. The contribution to the total capacity from the catalyst itself needs to be examined because the complete electrochemical decomposition of catalyst into its elemental forms sometimes produces a significant amount of capacity [65]. Furthermore, as the destructive transformation of the original structure leads to the loss of catalytic activity, it is necessary to determine an appropriate potential range before an actual Li-oxygen cell test. For the lead ruthenate (expanded) pyrochlore, the complete decomposition reaction by metallic lithium activity involves the following possible conversion reactions owing to its nano-crystalline character [211-215].

$$Pb_2Ru_2O_{6.5} + 13Li^+ + 13e^- \rightarrow 2Pb + 2Ru + 6.5Li_2O \quad (4\text{-}1)$$

$$Pb_2[Ru_{1.73}Pb_{0.27}]O_{6.5} + 13Li^+ + 13e^- \rightarrow 2.27Pb + 1.73Ru + 6.5Li_2O \quad (4\text{-}2)$$

The total reactions involve thirteen electrons per unit pyrochlore formula. The capacities of lead ruthenate stoichiometric and expanded pyrochlore expected from these reactions are 484 mAh g^{-1} and 465 mAh g^{-1}, respectively. The electrochemistry of nanocrystalline lead ruthenate pyrochlore in two different voltage ranges is shown in **Figure 4.5**.

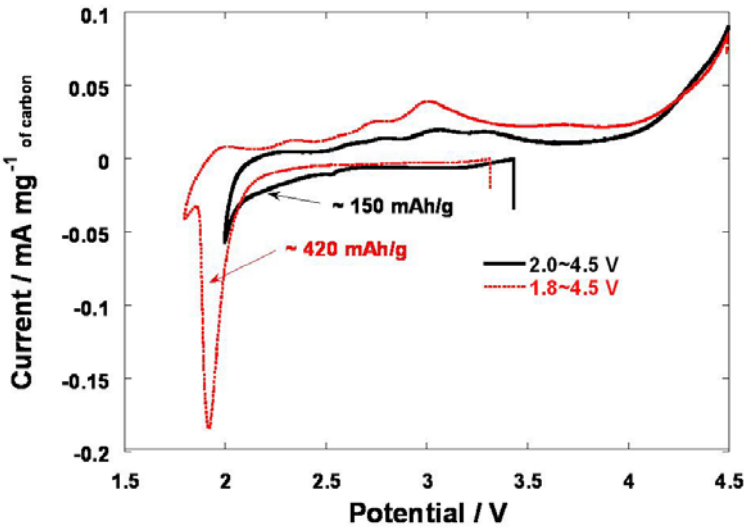

Figure 4.5 Potential sweep measurement for lead ruthenate pyrochlore with two different potential ranges. Electrolyte system is 1 M $LiPF_6$ in tetraethylene glycol dimethyl ether (TEGDME) and the scan rate is 0.02 mV/sec.

The discharge capacity down to 1.80 V is approximately 420 mAh g^{-1} whereas 150 mAh g^{-1} down to 2.00 V. The sharp reduction peak at 1.92 V vs. Li/Li^+ means that the reduction process at this potential involves the same number of phases and components, which is a typical condition for many conversion process involving metal oxide and lithium ion. This probably represents a conversion reaction of the pyrochlore decomposition although a slight less capacity indicates the conversion at this potential may not involve complete reduction to metallic state of its components. Therefore, in order to maintain catalytic activity of pyrochlore structure, the lower cutoff potential for Li-oxygen cell should be higher than this value. The capacity down to 2.00 V, however, is certainly related with the intercalation of lithium ions through pyrochlore structure, and the corresponding reduction of Ru^{5+} to Ru^{3+} as only broad electrochemical peaks for single phase reactions are observed. The two dimensional hexagonal arrangement of RuO_6 octahedra and their stacking through (111) direction in Ru_2O_6 structure leaves plenty of internal space for lithium diffusion [135,138]. The charging of the electrode discharged down to 1.80 V exhibits at least five separate

electrochemical reactions. These probably represent redox reactions from Pb^{2+}/Pb^{3+}, Pb^{3+}/Pb^{4+}, Ru^{o}/Ru^{3+}, Ru^{3+}/Ru^{4+} and Ru^{4+}/Ru^{5+} couples. These reactions produce a mixture of separate transition metal oxides rather than the single original pyrochlore structure. The charging of the electrode discharged down to 2.00 V shows two distinct electrochemical peaks at 3.06 V and 3.30 V, which are probably related with the Ru^{3+}/Ru^{4+} and Ru^{4+}/Ru^{5+} redox couples [211]. The additional peak at 2.80 V may be related with the $Pb^{2}+/Pb^{4+}$ redox couple as the area under this peak is substantially smaller than the other two major peaks [214]. From the previous discussion, it is proposed that the OER proceeds on the surface oxygen of Ru_2O_6 structure, and it occurs anodic to the redox potential of $Ru^{4}+/Ru^{5+}$ couple. Therefore, ideally, the oxygen evolution should occur at just over 3.30 V vs. Li/Li^{+} in the presence of ruthenium pyrochlore oxide. The increase in anodic current over 4.0 V is probably related with the decomposition of electrolyte system [150].

The contribution of various catalysts to the total electrochemical capacity of the Li-oxygen cell was evaluated by a galvanostatic discharge experiment and is shown in **Figure 4.6**. The capacity from the capacitive charging of the carbon surface amounts to approximately 20 mAh g^{-1}. The contribution of catalyst excluding this double layer charging is about 30 ~ 110 mAh g^{-1} depending on the catalyst type. As the capacity of Li-oxygen cell with bismuth ruthenate pyrochlore exhibits about 3300 mAh g^{-1} with the same electrode and electrolyte system, the catalyst contribution to the total capacity is considered to be almost negligible. This result proves that the high capacity shown in Li-oxygen cell really comes from oxygen reduction reaction.

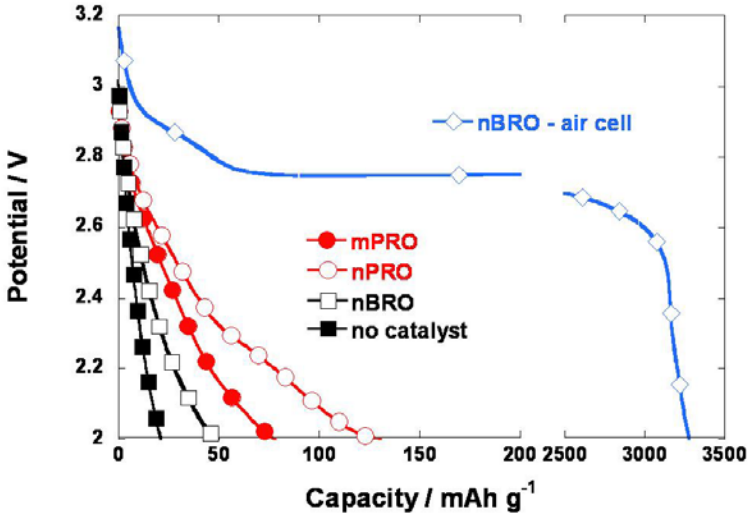

Figure 4.6 Galvanostatic discharge curves of Li-oxygen cell with / without presence of oxygen. The cathodes containing catalysts **nPRO**, **mPRO**, and **nBRO** are defined in **Section 4.7.2**. Constant current of 70 mA g^{-1} were applied to the all the cells.

4.3 ORR / OER of Li-oxygen cell with 0.5 M LiBOB in PC

4.3.1 Li-oxygen cell with 0.5 M LiBOB in PC electrolyte

The Li-oxygen cell performance with various catalysts synthesized in this thesis, including mesoporous lead ruthenate (**mPRO**), nano-crystalline lead ruthenate (**nPRO**), nano-crystalline bismuth ruthenate (**nBRO**) with the extended pyrochlore crystal structure together with α-MnO_2 nanowire catalyst, was evaluated with 0.5 M LiBOB in PC electrolyte. The α-MnO_2 nanowire was prepared by following the literature method [202] and utilized as a reference material for the evaluation of pyrochlore catalysts, as the ORR/OER properties of this material were already investigated by P. G. Bruce et al. [121] and it is known to be one of the best catalysts so far.

Propylene carbonate is a viscous, highly polar (dielectric constant: 64) but aprotic solvent. It has a wide range of liquid region (m.p.: -48.8 ^{o}C) as opposed to ethylene carbonate (EC) which has similar structure and properties, but solid at room temperature (m.p.: 36.4 ^{o}C). It is often considered as a solvent for lithium battery as it creates a very effective solvation shell around lithium ion creating highly conductive electrolyte. It is often used in a combination with other less viscous solvents like DME to lower the viscosity of the overall solvent. However, PC is not considered for Li-ion batteries mainly because it has a destructive property for graphite as it intercalates into graphene layer together with lithium ion and get trapped during the charge process [216,217]. Eventually, this leads to the exfoliation of the graphite. The excellent stability of PC with lithium metal comes from the initial reduction of some PC molecules and the formation of alkyl carbonate-type SEI layer on the surface, which serves as a protective passive layer. Ironically, the same reduction phenomenon of PC by metallic lithium also accounts for the slow degradation of cell performance after long cycling. PC has a moderate oxygen solubility of 3.20 μmol cm^{-3} and its viscosity is relatively high (2.53 cP) meaning slow diffusion of O_2. However, it has a high boiling point (242 ^{o}C) and the vapor pressure at room temperature is very low (0.003066 kPa) [218], which is suitable as a solvent for Li-oxygen cells.

Lithium bis(oxalato)borate (LiBOB) was introduced as one alternative lithium salt to replace conventional $LiPF_6$ [219,220]. For $LiPF_6$, it is well known that a little contamination by humidity generates corrosive HF which has a lot of detrimental side effects on either the cathode or anode while LiBOB is quite stable in the presence of humidity. Because the Li-oxygen cell easily takes up moisture from the ambient atmosphere, the resistance of the lithium salt anion against decomposition from moisture attack is one of the most important

factors [150]. In this aspect, LiBOB is superior to $LiPF_6$ although the solubility of LiBOB in aprotic solvent is generally lower. However, the stability of PC or LiBOB as an electrolyte system for the oxygen reduction and evolution reactions has not been fully investigated yet.

The catalytic activity of various catalysts and the corresponding Li-oxygen cell performance were evaluated by galvanostatic discharge-charge cycling experiments. The cathode was manufactured, and the electrochemical cells were assembled as they are explained in **Section 4.1**. The actual compositions of various cathodes were listed in **Table 4.1**. A sufficient amount of catalyst (catalyst: carbon = 1: 1 by weight) was provided to investigate the catalytic effect clearly taking high density of pyrochlore materials into account (density = 8.88 g/cm^3 [140]). In the case of α-MnO_2, the ratio of catalyst to carbon is set to 0.5 by weight, which shows the best performance among the various electrode compositions tried. The current was applied at a rate of 70 mA per gram of carbon existent on the cathode [97,99,100,121], which corresponds to the rate where approximately 1.0 g of oxygen gas reacts per gram of carbon in one day.

Table 4.1 Compositions of electrodes manufactured for catalyst evaluation. Catalysts include **mPRO** (mesoporous lead ruthenate), **nPRO** (nano-crystalline lead ruthenate), **nBRO** (nano-crystalline bismuth ruthenate) and α-MnO_2 catalysts. Numbers are in w.t. ratios.

Electrode	catalyst type	carbon	catalyst	binder	DBP
mPRO	meosporous oxide	1	1	2.4	4
nPRO	nano-crystalline oxide	1	1	2.4	4
nBRO	nano-crystalline oxide	1	1	2.4	4
α-MnO2	nanowire	1	0.5	2.4	4

Figure 4.7 shows the 1st and the 2nd discharge-charge profiles of Li-oxygen cells with various catalysts. For all pyrochlore catalysts, they have a similar discharge capacity around

3000 mAh/g which is a little higher than that from α-MnO_2, 2600 mAh/g. The highest capacity at the first cycle is about 3300 mAh g^{-1}, and comes from **mPRO** catalyst.

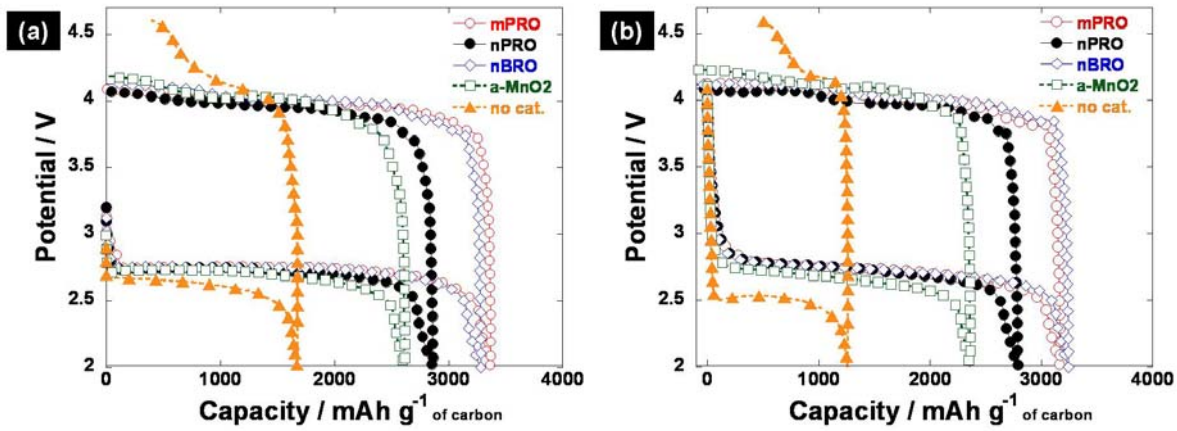

Figure 4.7 Discharge-Charge profiles (a) at the 1st cycle and (b) the 2nd cycle of Li-oxygen cell with various catalysts including pyrochlores and α-MnO_2 and without catalyst in 0.5 M LiBOB in PC electrolyte. The current rate is 70 mA per gram of carbon.

The discharge voltages of catalyzed cells at the 1st cycle are similar with each other around 2.70 ~ 2.75 V and 60 ~ 80 mV higher than the non-catalyzed cell. These observations imply that the discharge processes in the presence of catalysts have different reduction mechanisms from simple carbon or reaction kinetics improved with metal oxide catalyst. In the alkaline aqueous solution, amorphous carbon is actually an oxygen reduction catalyst as many sp^3 dangling bonds on the surface contribute to the destabilization of O=O bonding in the oxygen generating peroxide anions, and it is reasonable to assume that amorphous carbon is also a catalyst for oxygen reduction in aprotic solution. Thus, both pyrochlore oxides and α-MnO_2 are more efficient catalyst for oxygen reduction in this electrolyte than amorphous carbon itself. In addition, slightly higher discharge potential of pyrochlore oxide at the 1st and 2nd cycles proves a better catalytic activity for ORR than α-MnO_2. The theoretical

equilibrium potential for oxygen reduction when the reaction product is Li_2O_2 is 2.959 V [119,120,221]. Thus the overpotential related with oxygen reduction is approximately 0.2 V at 70 mA/g current rate, which is similar with that from the aqueous solution when highly effective catalyst is used on a carbon support.

The pore volume calculated from the DBP amount in the cathode is approximately 4 cm^3 per gram of carbon. If these pores are filled with only ideal product, lithium peroxide, the resulting capacity would be as much as 11,000 mAh/g or even a little bit higher as many other pores are created by quick solvent evaporation, and additional textural porosity also exists. The termination of oxygen reduction reaction on the cathode usually occurs when all the pores are filled with reduction products, and thus no more surface site is available for further ORR. From the total discharge capacity of 3000 mAh/g, we may assume that, at most, approximately one third of the total pore volume is occupied by reaction product, Li_2O_2, which is considered to be too small to initiate a major polarization. Therefore, it does not appear too far to assume that the reaction product from this electrolyte system actually may not be lithium peroxide.

In order to ascertain whether the pore volume on the cathode is a dominating factor to determine the overall capacity of Li-oxygen cell [93], the pore structure of the cathode film was intentionally destroyed by extracting the plasticizer from the film with ethyl ether and pressing the film moderately against aluminum grid. The resulting electrochemical behavior of Li-oxygen cell keeping all the other conditions the same is shown in **Figure 4.8** together with the performance of original film. It shows that the discharge capacity of the pore-destroyed cathode exhibits only 40 % of the original film, which denotes that the porosity of the cathode indeed controls the overall discharge capacity.

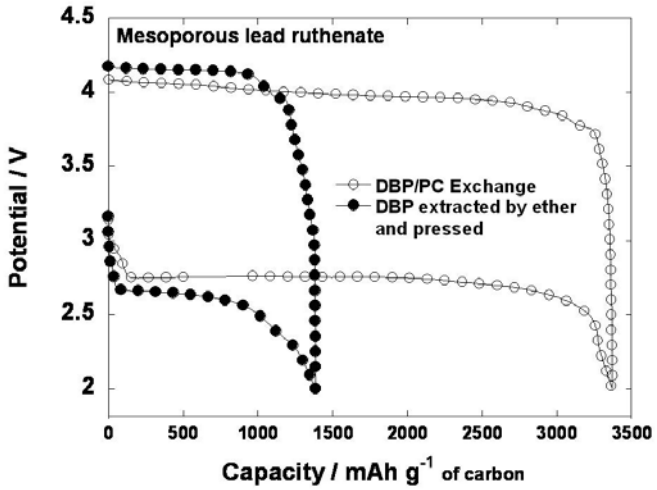

Figure 4.8 Discharge-charge profiles of Li-oxygen cell with mPRO catalyst at the first cycle for the original electrode and for the electrode whose pore is destroyed.

In order to clarify the discharge product from LiBOB in PC electrolyte system, X-ray diffraction patterns and infrared spectra are collected for the discharged electrodes. The Li-oxygen cells containing catalysts were discharged down to 2.0 V and were taken apart inside an argon-filled glove box. The cathode part was washed with plenty of dried THF to remove the electrolyte remnants [92]. After dried in the glove box, the sample was loaded in a gas-tight holder for X-ray diffraction measurement. **Figure 4.9a** shows X-ray diffraction patterns of the discharged electrode with nPRO catalyst and lithium oxalate ($Li_2C_2O_4$) reagent, which shows the discharge product is almost exclusively composed of lithium oxalate. This finding is further confirmed by infrared spectra measured with the same electrode (**Figure 4.9b**). Though there are some minor peaks, most of the prominent peaks can be explained by those from the lithium oxalate [222-224].

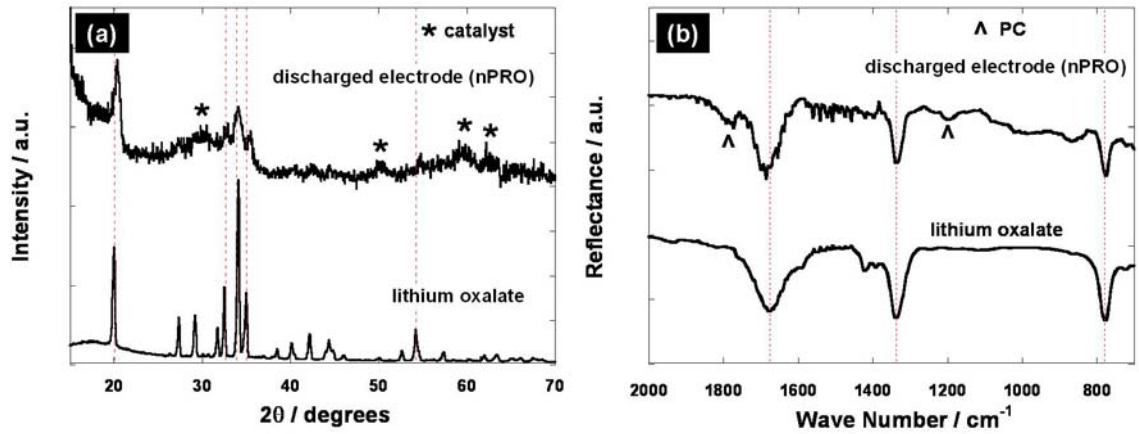

Figure 4.9 Identification of discharge product of Li-oxygen cell with nPRO catalyst by analyzing (a) X-ray diffraction patterns and (b) FT-IR spectra for discharged electrode and lithium oxalate ($Li_2C_2O_4$)

The discharge product from α-MnO_2 catalyst was also analyzed by the same techniques (**Figure 4.10a, b**). Both the X-ray diffraction pattern and infrared spectra indicate that the main discharge product is lithium oxalate, although IR spectra also suggest the existence of lithium carbonate and lithium triborate. Lithium carbonate probably comes from PC decomposition by superoxide attack [113-115]. Therefore, irrespective of catalyst types, the common discharge product is identified as lithium oxalate.

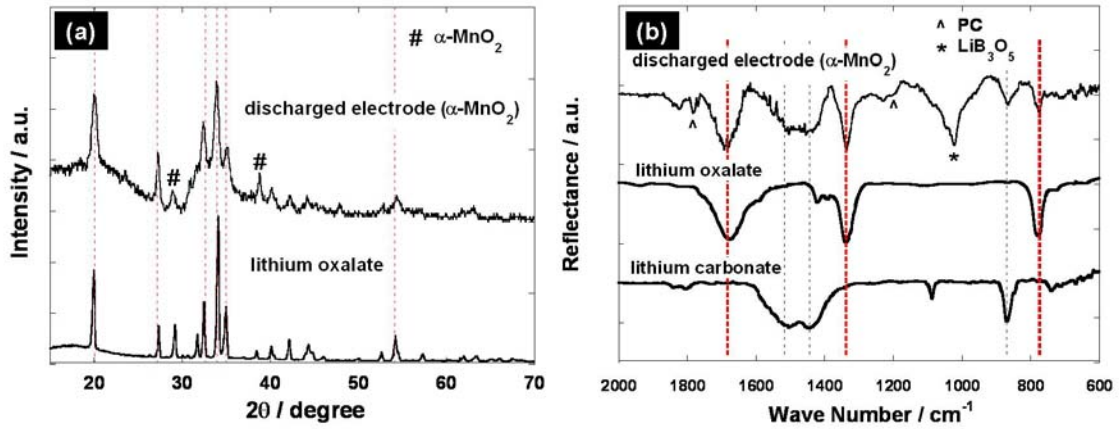

Figure 4.10 Identification of discharge product of Li-oxygen cell with α-MnO_2 catalyst by analyzing (a) X-ray diffraction patterns and (b) FT-IR spectra for discharged electrode and lithium oxalate ($Li_2C_2O_4$). In addition to lithium oxalate, lithium carbonate and lithium triborate were also observed as reaction product.

The existence of lithium oxalate in the discharged electrode unequivocally suggests that this material was born from the decomposition of electrolyte salt, LiBOB [224]. This decomposition can be most reasonably explained by superoxide attack on the boron center and the destabilization of the chelating bond with the neighboring oxygen of the oxalate group in LiBOB. After breakup, the negative charge on the terminal oxygen can be greatly stabilized by the adjacent C=O group. Such a mechanism is proposed in **Figure 4.11** where series of superoxide attacks on the boron center of LiBOB results in CO, CO_2 and O_2 gas evolution. The final insoluble products are made up of lithium oxalate ($Li_2C_2O_4$), boron trioxide (B_2O_3) and lithium oxide (Li_2O) [224]. Among those decomposition products, boron trioxide and lithium oxide are usually found as vitreous form so that they do not appear in the X-ray diffraction pattern.

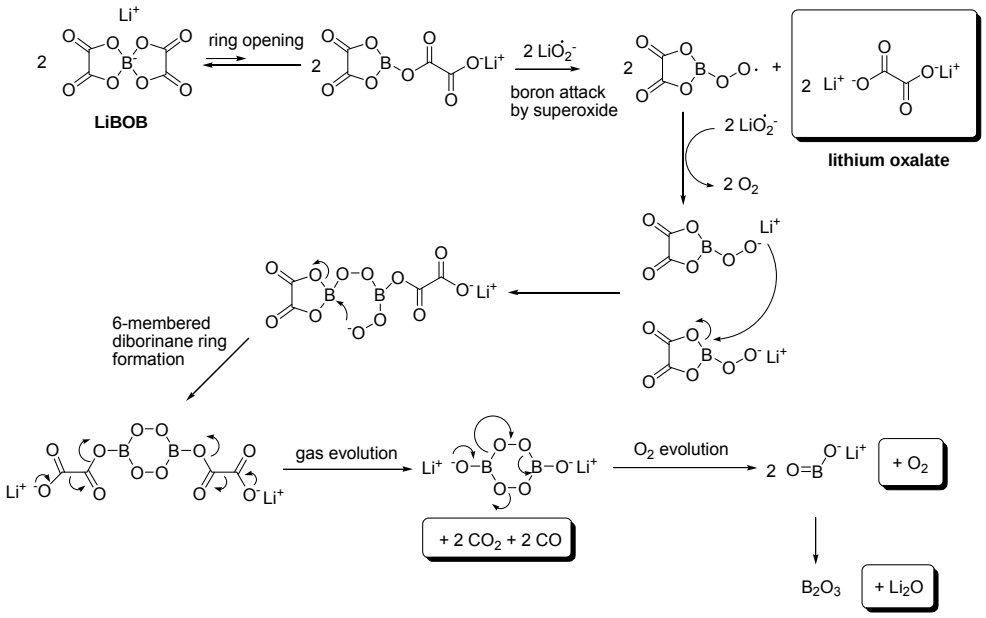

Figure 4.11 Tentative mechanism for LiBOB decomposition by superoxide attack at boron center which results in lithium oxalate, boron trioxide and lithium oxide as decomposition product.

The reactions for each step in **Figure 4.11** are summarized as follows.

$$4O_2 + 4e^- \rightarrow 4O_2^- \quad (4\text{-}3)$$

$$2(LiBC_4O_8) + 2O_2^- + 2Li^+ \rightarrow 2BC_2O_6 + 2Li_2C_2O_4\downarrow(\text{crystalline}) \quad (4\text{-}4)$$

$$2BC_2O_6 + 2O_2^- \rightarrow 2BC_2O_6^{2-} + 2O_2 \quad (4\text{-}5)$$

$$2BC_2O_6^{2-} \rightarrow 2BO_2^- + O_2 \quad (4\text{-}6)$$

$$2BO_2^- + 2Li^+ \rightarrow B_2O_3\downarrow(\text{amorphous}) + Li_2O\downarrow(\text{amorphous}) \quad (4\text{-}7)$$

Because the reduction process involves the formation of lithium oxalate and boron trioxide, the pores on the cathode are to likely be filled with these materials. The pertinent cathodic reaction for overall process can be written as follows.

$$2LiBC_4O_8 + O_2 + 4Li^+ + 4e^- \rightarrow 2Li_2C_2O_4 + 2CO_2 + 2CO + B_2O_3 + Li_2O \quad (4\text{-}8)$$

In terms of lithium oxalate (MW: 101.90), theoretical capacity for the **Reaction 4-8** is calculated to be 526 mAh g^{-1} and its density is 2.121 g cm^{-3} [225]. If we assume that all the pores (4 cm^3 g^{-1}) on the cathode were filled with lithium oxalate, boron trioxide (2.55 g cm^{-3} [225]) and lithium oxide (2.013 g cm^{-3} [225]) with 2:1:1 mole ratio, the Li-oxygen cell capacity would be around 3100 mAh g^{-1}, which is very close to the experimentally measured value for the discharge capacity. This agreement between simple calculation and the experimental data further confirms the main discharge product from this electrolyte system is lithium oxalate with amorphous B_2O_3 and Li_2O phases. The existence of lithium triborate

from IR spectra in the case of α-MnO_2 catalyst probably indicates further reaction of boron trioxide with lithium oxalate occurs to some extent in the presence of this catalyst.

$$Li_2C_2O_4 + 3B_2O_3 \rightarrow 2LiB_3O_5 \text{ (amorphous)} + CO + CO_2 \quad (4\text{-}9)$$

In **Figure 4.7a, b** the charging potentials of Li-oxygen cells with various catalysts are observed around 4.0 V and they are very similar with each other regardless of catalyst type, although catalyst indeed lowers the decomposition potential compared with the non-catalyzed case. From the X-ray diffraction pattern and IR observations, the charging process involves the decomposition of lithium oxalate. Therefore, in this electrolyte system, the true characteristics of catalyst toward OER cannot be evaluated. For the minor amorphous B_2O_3 phase, further oxidation is unlikely to occur. The appropriate anodic electrochemical reaction for this can be written as follows.

$$Li_2C_2O_4 \rightarrow 2Li^+ + 2CO_2 + 2e^- \quad (4\text{-}10)$$

The anodic decomposition of lithium oxalate generates CO_2 gas and lithium ions. Therefore, catalyst in this electrolyte system helps lithium oxalate decomposition reaction to release CO_2 gas. **Figure 4.12** shows the discharge-charge profiles of the first cycle with and without presence of **nPRO** catalyst. The presence of catalyst results in the much larger discharge capacity and substantially lower anodic overpotential. This means that the presence of catalyst actually plays an important role in decomposing LiBOB as well as lithium oxalate efficiently.

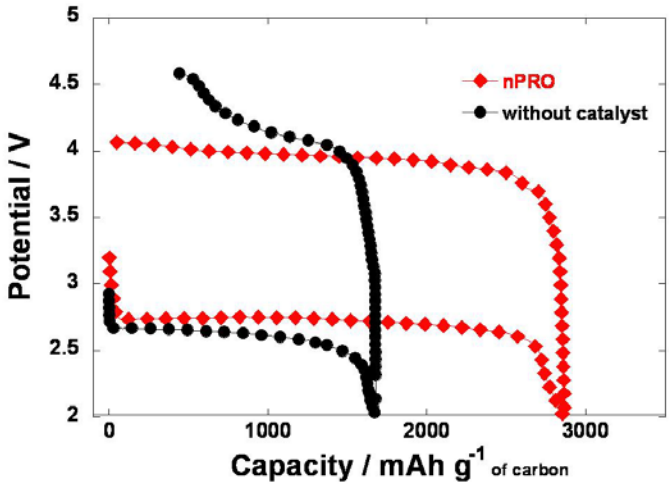

Figure 4.12 Discharge-charge profiles of Li-oxygen cell with nPRO catalyst and without any catalyst. The presence of catalyst accounts for the increased discharge capacity as well as significant lowering of the charge overpotential.

It is important to keep the decomposition potential as low as possible to minimize electrolyte oxidation occurring at high overpotential [150] since oxygen dissolved in electrolyte can accelerate electrolyte decomposition in the presence of catalyst. **Figure 4.13** shows the cycling stability of Li-oxygen cells up to 10 cycles. It shows that all the pyrochlore catalysts decompose lithium oxalate very efficiently with a good cycling stability, where the slow decrease in discharge capacity with cycling is probably caused by the corrosion on the anode side and the accumulation of amorphous Bi_2O_3 phase in the cathode pore structure. For the α-MnO_2 catalyst however, the cell goes into a sudden malfunction after 5th cycle. This is probably caused by manganese dissolution [30,31] into the electrolyte through the disproportionation reaction (**Reaction 4-11**) initiated by the structural instability from Jahn-Teller distortion in Mn^{3+} [226] formed during the discharge process commonly found in other manganese oxides.

$$2Mn^{3+} \rightarrow Mn^{2+} + Mn^{4+} \qquad (4\text{-}11)$$

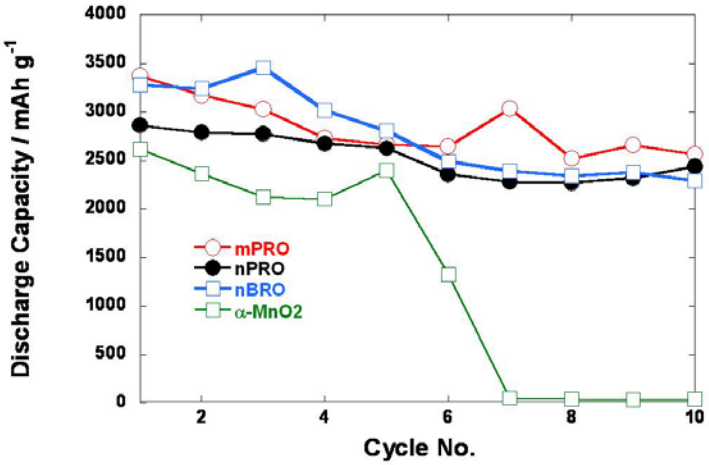

Figure 4.13 Cycling performance of Li-oxygen cell with various catalysts up to 10 cycles with 0.5 M LiBOB in PC electrolyte. Discharge capacity and capacity retention is similar for pyrochlore catalysts. The α-MnO_2 catalyst shows a sharp decline in discharge capacity after initial 5 cycles.

In short, the reactions for Li-oxygen cell with 0.5 M LiBOB electrolyte involve the decomposition of LiBOB by the interaction with superoxide and the formation of lithium oxalate during the discharge process. The charge process involves the decomposition of lithium oxalate to release CO_2 gas. With the help of catalyst, the kinetics for these processes can be enhanced substantially. However, even though a reaction product can be decomposed completely by catalyst, as the continuous reaction of superoxide with electrolyte leads to the depletion of electrolyte after many cycles, the long-term cycling stability is a major problem for cells employing this electrolyte system.

4.3.2 Decomposition of Li_2O_2 with 0.5 M LiBOB in PC electrolyte

The decomposition behavior of the ideal discharge product, Li_2O_2 was investigated by low scan rate (0.02 mV sec^{-1}) potential sweep method in 0.5 M LiBOB in PC electrolyte

system. The electrode containing Li_2O_2 was subject to a slow anodic scan up to just over the decomposition potential to observe an electrochemical response related with Li_2O_2 decomposition [97,114]. As the superoxide anion is not present in anodic (oxidizing) condition, LiBOB salt or PC is regarded to be stable throughout the whole anodic scan, and is suitable for investigating Li_2O_2 decomposition behavior.

The Li_2O_2 electrode was prepared by mixing appropriate amount of Li_2O_2, carbon, catalyst and binder together in acetone thoroughly inside argon-filled glove box using mortar and pestle casting it into a thin film. The detailed composition of each electrode is summarized in **Table 4.2**. The film was dried inside the glove box and cut into a disc. The similar electrochemical cell used in Li-oxygen cell was utilized for investigation, but no oxygen was provided either before or during the measurement.

Table 4.2 Composition of Li_2O_2 electrodes used for the evaluation of catalytic activity of various catalysts toward Li_2O_2 decomposition. Numbers denote wt. ratio used.

Electrode name	catalyst used	carbon	Li_2O_2	catalyst	binder
Li2O2_KB	no catalyst	1	1	0	4
Li2O2_nPRO	nPRO	1	1	1	6
Li2O2_nBRO	nBRO	1	1	1	6
Li2O2_aMnO2	α-MnO_2	1	1	0.5	6
KB	no catalyst	1	0	0	4

Figure 4.14 shows the resulting electrochemical behaviors of Li_2O_2 decomposition with **nPRO** pyrochlore catalyst, α-MnO_2 nanowire and just carbon black in the absence of any catalyst.

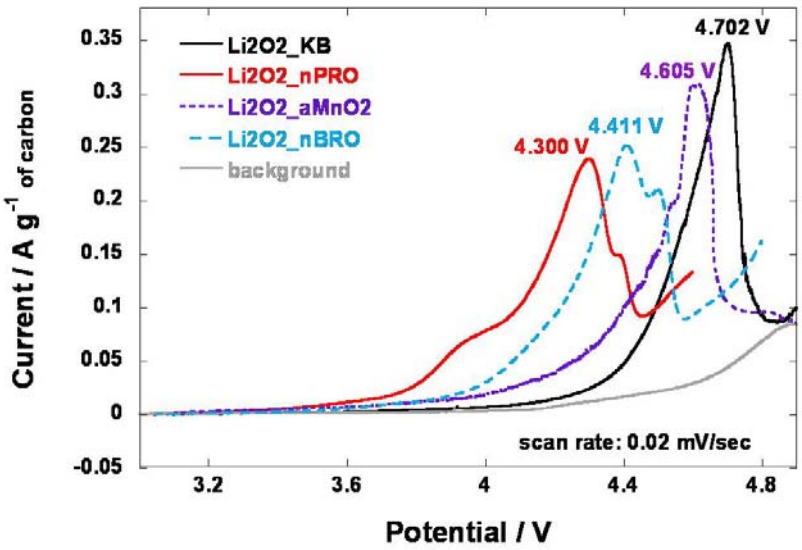

Figure 4.14 Potential sweep measurements of Li_2O_2 electrodes with various catalysts showing an electrochemical decomposition of Li_2O_2 with peak potentials indicated. The electrolyte system is 0.5 M LiBOB in PC and scan rate is 0.02 mV sec^{-1}.

For the **nPRO** catalyst, meaningful decomposition starts as early as at 3.75 V with a small but significant peak centered at 3.95 V, followed by the major decomposition at 4.30 V with a shoulder near 4.40 V. It is speculated that the peak at 3.95V is related with the decomposition of Li_2O_2 existing just adjacent to the catalyst where no diffusion of Li_2O_2 is necessary. The catalytic activity at this potential is probably performed by Ru^{4+}/Ru^{5+} redox couple as described in **Section 1.6**. As the anodic potential goes up, Li_2O_2 located off the catalyst site diffuses to the catalyst and the resulting current increases naturally as the concentration gradient of Li_2O_2 on the catalyst surface becomes larger. However, as the diffusion boundary expands and most Li_2O_2 is used up, the current is controlled by the diffusion flux to the catalyst site and starts to decrease sharply. The little hump at 4.40 V after major decomposition peak corresponds to electrolyte or carbon oxidation by evolving oxygen gas. As the total amount of oxygen releasing from the Li_2O_2 decomposition is limited, the intensity of this peak is not too strong.

The curves for the anodic potential sweep of the Li_2O_2 electrode with α-MnO_2 nanowire catalyst and without any catalyst show a similar behavior where single peaks exist at 4.60 V and 4.70 V, respectively. They do not exhibit a great catalytic behavior for OER, although the decomposition potential for α-MnO_2 nanowire is a little lower. Conventionally, glassy carbon has been used as a catalyst for ORR via peroxide route in the alkaline solution together with a peroxide elimination catalyst. However, it is not recognized as a good catalyst for OER as the surface quickly degrades by the reaction with oxygen. Many transition metal oxides including MnO_2 with different crystal structure have been reported as a good catalyst for chemical decomposition of hydrogen peroxide into water and oxygen [227-230].

$$2H_2O_2 \rightarrow 2H_2O + O_2\uparrow \qquad (4\text{-}12)$$

Recent research indicates that a series of MnO_2 including α-MnO_2 and EMD are good electrochemical Li_2O_2 decomposition catalysts as it is believed that the decomposition of H_2O_2 and Li_2O_2 are very similar in nature and the rate constant for H_2O_2 decomposition is directly related with decomposition overpotential of Li_2O_2 [114]. However, in this thesis, the catalytic activity of α-MnO_2 for Li_2O_2 decomposition turned out to be low. The reason for this discrepancy is not clear, but this may be related with the different electrolyte system employed or the effect of defect structure in manganese oxide [123,124].

To verify that the electrochemical peaks from the anodic potential sweep truly originates from the decomposition of Li_2O_2, X-ray diffraction pattern measurement before and after anodic scan was measured and shown in **Figure 4.15**.

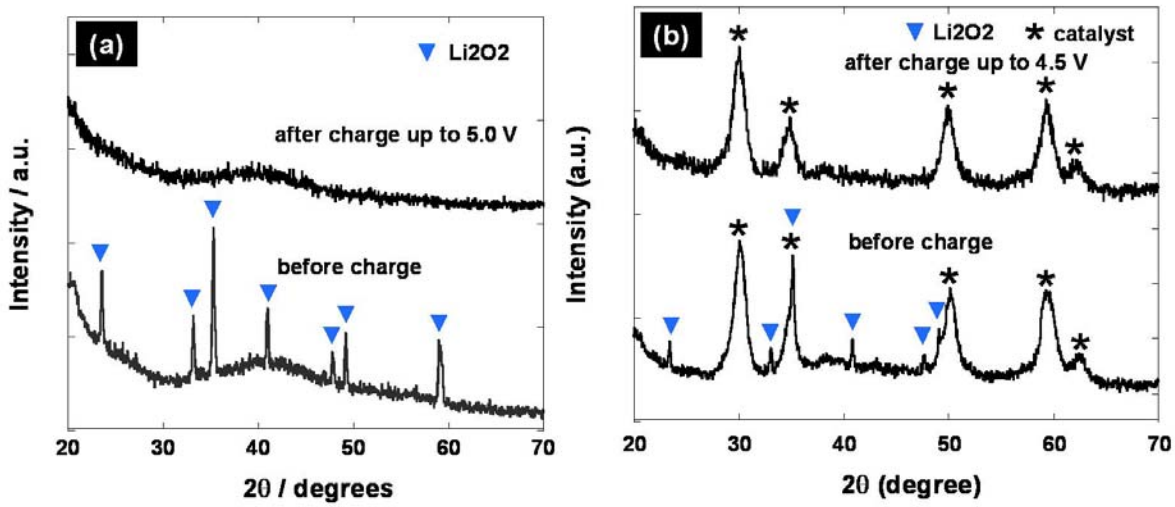

Figure 4.15 X-ray diffraction patterns of Li_2O_2 electrode as prepared and after it is charged until major electrochemical peak passes for (a) Li2O2_KB and (b) Li2O2_nPRO electrodes.

For the Li_2O_2 electrode without catalyst, the original Li_2O_2 pattern of as-prepared electrode disappears completely upon charging up to 5.00 V, which suggests the decomposition of Li_2O_2 is completed. The electrochemical capacity under the peak at 4.70 V is estimated to be 1144 mAh/g of carbon. The oxidative decomposition of Li_2O_2 can be written as follows.

$$Li_2O_2 \rightarrow 2Li^+ + O_2 + 2e^- \qquad (4\text{-}13)$$

The theoretical capacity from the full decomposition of Li_2O_2 when the Li_2O_2 to carbon ratio on the electrode is equal to one is 1168 mAh per gram of carbon, which is very close to the experimental data (98 % of the ideal value). Therefore, the electrochemical data truly corresponds to the decomposition of Li_2O_2. The X-ray diffraction pattern for Li_2O_2 electrode with **nPRO** catalyst shows the combination of broad peaks from nano-crystalline pyrochlore and sharp lines from Li_2O_2. After charging up to 4.50 V, the sharp reflection lines for Li_2O_2 disappear and only broad reflections from pyrochlore catalyst exist, which implies the

decomposition of Li_2O_2 occurred while the pyrochlore catalyst is stable up to 4.50 V. The coulombic capacity calculated from the area under 4.30 V peak is about 1150 mAh per gram of carbon, which is very close to the theoretical capacity of the Li_2O_2 decomposition. Therefore, the electrochemical event during the anodic scan is undoubtedly caused by the Li_2O_2 decomposition [97].

4.4 ORR / OER of Li-oxygen cell with 1 M $LiPF_6$ in TEGDME

As it turns out that LiBOB is not a stable lithium salt in the presence of superoxide radicals, $O_2^{\cdot -}$ during the discharge process of Li-oxygen cell $LiPF_6$ is considered as a replacement although there is a possible concern that PF_5, which is in equilibrium with PF_6^- [150], may react with superoxide radicals and PF_6^- itself or PF_5 causes a lot of harmful side effects in the presence of moisture as discussed in **Section 1.7**. Propylene carbonate is also reported in several previous works to experience ring opening by the superoxide radical attack on CH_2 group near carbonyl moiety [113-115,151]. After several successive reactions with superoxide radicals, lithium propyl dicarbonate, lithium formate, lithium acetate and lithium carbonate are produced as major solid discharge products.

Tetraethylene glycol dimethyl ether (TEGDME) is a viscous (4.05 cP) and non-polar (dielectric constant: 7.79) aprotic solvent. It has a much higher boiling point (275 ^oC) than DME, which has a similar structure with shorter chain (ethylene glycol dimethyl ether, glyme), but shows a much lower boiling point (84 ^oC) and is also much less viscous (0.46 cP). The vapor pressure of TEGDME at room temperature is very low (< 0.001316 kPa), which is suitable for Li-oxygen cell application. It has a slightly higher oxygen solubility of

4.70 μmol cm^{-3} than PC (3.20 μmol cm^{-3}). Ether-based electrolytes are known for their superb property of forming a good morphological development on the lithium surface through SEI formation during the electrochemical cycling [150]; i.e. the formation of dendrite is much suppressed compared to when carbonate-based electrolyte is used. However, it is also well known that it usually undergoes the oxidative decomposition upon exposure to high anodic potential, which results in the poor cycling performance [150,152].

The electrolyte 1 M $LiPF_6$ in TEGDME, which is allegedly more resistant to superoxide radical attack than 0.5 M LiBOB in PC was employed to evaluate the performance of various types of pyrochlore oxides and α-MnO_2 catalysts for ORR / OER in Li-oxygen cells. Cathodes with various catalysts were fabricated, and the electrochemical cells were assembled identically to how they were explained in **Section 4.1**. The galvanostatic discharge-charge experiment was performed at a constant current rate of 70 mA g^{-1} of carbon. **Figure 4.16** shows the discharge-charge curves of the 1st and 2nd cycles of Li-oxygen cells with different catalysts.

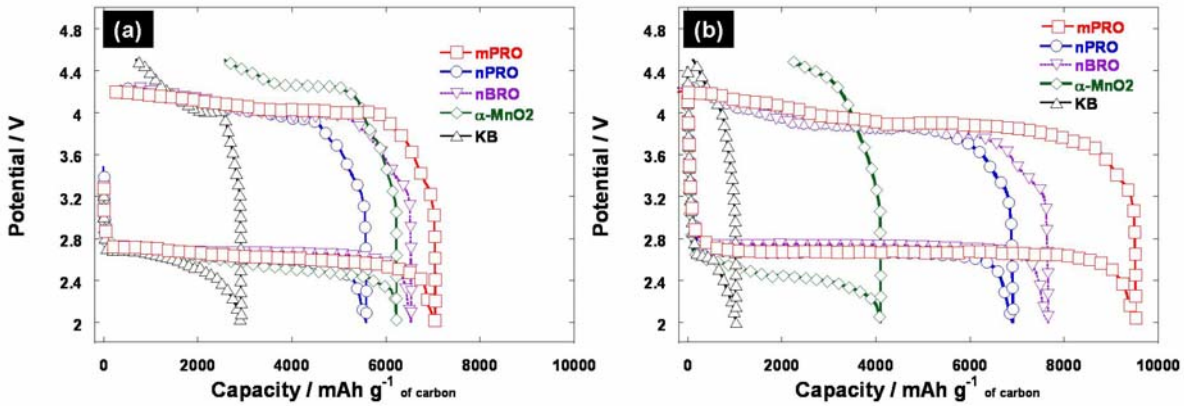

Figure 4.16 Discharge-charge profile of Li-oxygen cell with various catalysts including pyrochlores and α-MnO_2 in 1 M $LiPF_6$ in TEGDME electrolyte for (a) 1st and (b) 2nd cycles. The current rate is 70 mA per gram of carbon.

Generally, the discharge capacities produced from 1 M $LiPF_6$ in TEGDME electrolyte doubled the ones obtained from the 0.5 M LiBOB in PC system as they exhibit a capacity around 5500 ~ 7000 mAh g^{-1} at the first cycle. The discharge capacity of the 2nd cycle in **Figure 4.16b** grows even higher and reaches 7000 ~ 10000 mAh g^{-1}. In case of **mPRO** catalyst, the capacity reaches maximum value of 10300 mAh g^{-1} at the 3rd cycle as shown in **Figure 4.17**. These values are very close to the theoretical value expected from the pore volume of the cathode film (4 cm^3/g of carbon) supposing all the pores are filled with the 'ideal' discharge product, Li_2O_2. This strongly suggests that the main discharge product from this electrolyte system is not disintegrated precipitates of organics, but it is made up of simple lithium oxides like LiO_2, Li_2O or Li_2O_2 [92,119,120] because the organic decomposition products with large molecular masses, and low material density cannot produce such a high capacity from a given limited pore volume as described in **Section 4.3.1**.

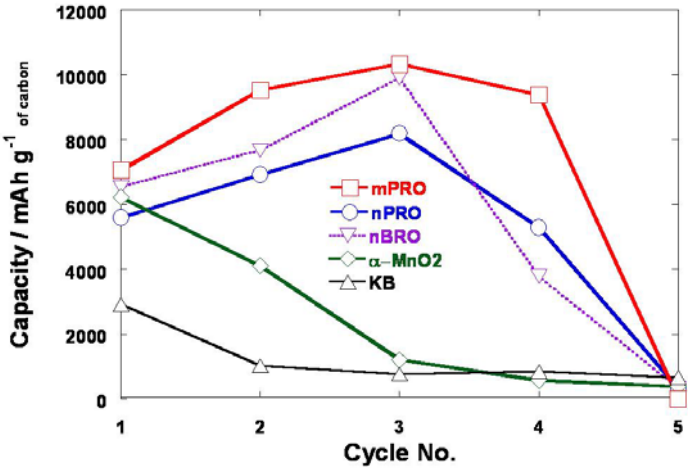

Figure 4.17 Cycling performance of Li-oxygen cell with various catalysts up to 5 cycles in 1 M $LiPF_6$ in TEGDME electrolyte system. Discharge capacity and capacity retention is similar for pyrochlore catalysts with maximum capacity at the 3rd cycle. The α-MnO_2 catalyst shows continuous decline in discharge capacity from the first cycle like electrode without catalyst.

The discharge plateau voltages for ORR with various catalysts in 1 M $LiPF_6$ in TEGDME electrolyte also depend on the existence and type of catalyst, and is in a range of 2.6 ~ 2.7 V, which is generally a little lower than that from PC electrolyte (2.70 ~2.75 V). The highest discharge voltage comes from the cathode with **nBRO** catalyst which exhibits around 2.67 V. The amorphous carbon is a good catalyst for oxygen reduction in aqueous alkaline solution and it involves the formation of peroxide on the surface. It should accompany good peroxide elimination catalysts like MnO_2 otherwise the potential would be much lower than that for four-electron process [88]. In the aprotic solution, it is known that oxygen reduction proceeds with the formation of superoxide at outer Helmholtz plane near glassy carbon surface [88].

$$O_2 + e^- \rightarrow O_2^- \qquad (4\text{-}14)$$

However, when hard Lewis acid like lithium ion is present in the solution, superoxide anion, which is relative soft Lewis base, becomes labile and it quickly decomposes to more stable peroxide form, which makes overall reactions irreversible [88,101-103]. In the presence of the pyrochlore oxide catalyst, the formation of peroxide as well as its decomposition can be catalyzed leading to lowered activation overpotentials for both ORR and OER as they are proposed in **Section 1.6**. In the case of PC electrolyte, superoxide radicals produced from OHP quickly react with electrolyte anions (BOB^-), and the reaction is not influenced much by the character of catalysts [113-115]. The minor variations in the discharge voltage for 1 M $LiPF_6$ electrolyte with various catalysts originate from the contribution from ORR on catalyst sites which will be discussed later in this Section.

Provided that the main discharge step for both PC and TEGDME electrolyte is the formation of superoxide with a reversible one-electron process, the equilibrium voltage is determined by concentrations of superoxide and oxygen near cathode surface.

$$E = E^o - RT/F \ln\left(a_{O_2^-} / f_{O_2}\right) \quad (4\text{-}15)$$

Other than the activation overpotential caused by activation energy for the electron transfer from electrode to oxygen molecules located at OHP, the discharge potential can be influenced by the diffusion characteristics of reacting or produced species; that is, how efficiently superoxide is removed or how fast oxygen is diffused from/to reaction site. In the case of PC electrolyte, the superoxide elimination rate from the electrode surface is considered to be fast because superoxide directly reacts with nearby electrolyte anions [115]. However, the superoxide concentration near the electrode surface in TEGDME may not be negligible because the lithium ion solvated with TEGDME molecules from the bulk solution may form a quasi-stable compound, stabilizing superoxide anion with non-negligible half life [102,103]. Depending on the solvent basicity [128], the firm solvation shell around lithium ion sometimes makes it act like a soft Lewis acid, which leads to the formation of quasi-stable $Li(solvent)_n\text{-}O_2$. This lithium solvent superoxide will decompose to lithium peroxide releasing oxygen by dismutation like **Reaction 4-16** [102].

$$2Li(solvent)_n\text{-}O_2 \rightarrow Li_2O_2 + O_2 + n\ solvent \quad (4\text{-}16)$$

Thus, for TEGDME electrolyte, the concentration of superoxide anions near the electrode surface may not be small enough that it may actually contribute to lowering discharge potential of the Li-oxygen cell.

The discharge product from 1M $LiPF_6$ in TEGDME electrolyte was investigated by analyzing X-ray diffraction patterns (**Figure 4.18a**) and infrared spectra (**Figure 4.18b**) collected for the discharged electrodes with various catalysts down to 2.0 V. The discharged electrode was dismantled inside an argon-filled glove box, and the cathode part was washed with dried THF [92]. After it was dried, the sample was loaded in a gas-tight X-ray holder for measurement. **Figure 4.18a** shows the X-ray diffraction patterns for discharged electrodes without any catalyst and with **nPRO** catalyst. The pattern for the discharged electrodes clearly shows the formation of nano-crystalline Li_2O_2 with hexagonal space group, $P6_3/mmc$ [208,209] regardless of the presence of catalyst. From the broadness of the (110) peak of the X-ray diffraction pattern of the discharged electrode without catalyst, the coherent length along [110] direction is estimated about 16 nm.

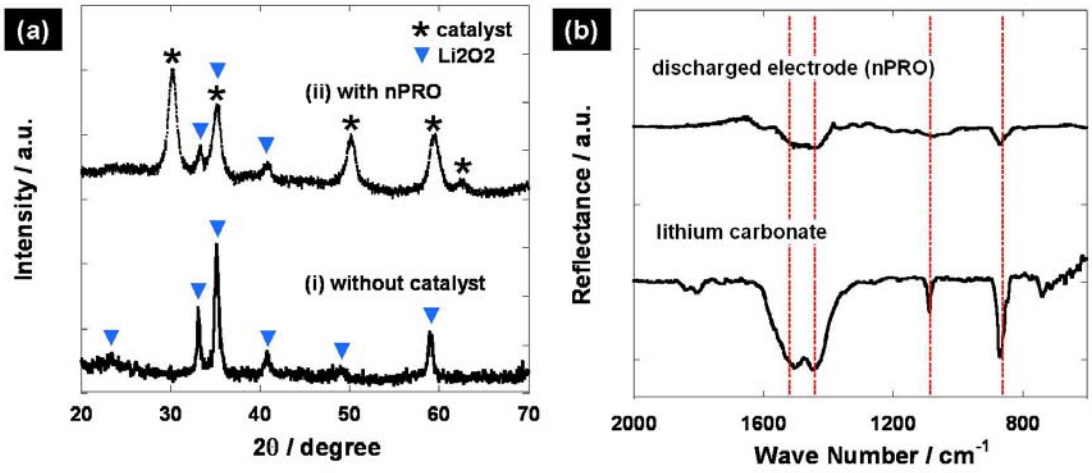

Figure 4.18 Identification of discharge product of Li-oxygen cell with 1 M $LiPF_6$ in TEGDME electrolyte by analyzing (a) X-ray diffraction patterns and (b) FT-IR spectra for discharged electrode and lithium carbonate (Li_2CO_3). The XRD patterns indicate that discharge product is Li_2O_2 regardless of the presence of catalyst. From IR spectra little organic decomposition product is observed.

The XRD patterns for the discharged electrode with **nPRO**, **mPRO** and α-MnO_2 nanowire catalysts also show the formation of Li_2O_2 in common, although there is some variation in their crystallinity or crystallite size (**Figure 4.18a, 19**). In order to check if any organic precipitate from the electrolyte decomposition is deposited on the cathode, which does not appear in X-ray diffraction due to its amorphous character, infrared spectrum for discharged electrode with **nPRO** catalyst is measured (**Figure 4.18b**). From the spectrum, no particular organic functional group is observed except a little hint of lithium carbonate formation, trace amount of which can be formed from Li_2O_2 by absorbing CO_2 from the air during the measurement.

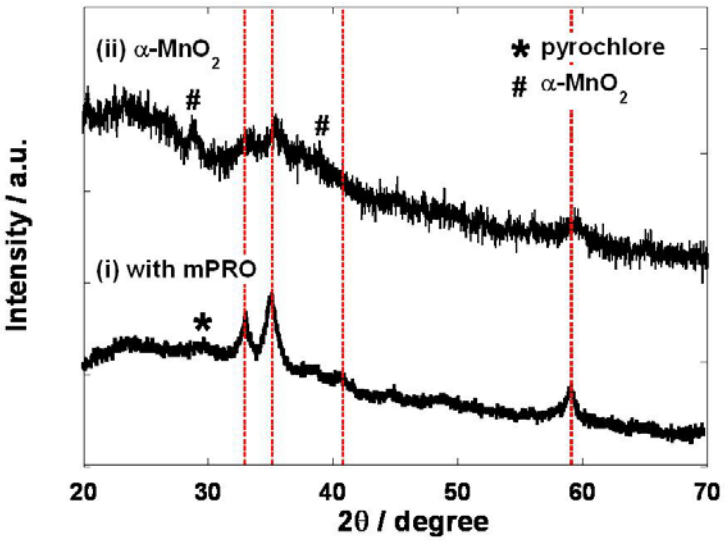

Figure 4.19 X-ray diffraction patterns for the discharged electrode in 1 M $LiPF_6$ in TEGDME electrolyte with catalyst (i) mPRO and (ii) α-MnO_2. The XRD patterns indicate that discharge product is Li_2O_2 for both cases.

Therefore, the discharge product from 1 M $LiPF_6$ in TEGDME is identified as Li_2O_2 regardless of catalyst type or presence of catalyst. This implies that the main parameter to determine the discharge product is not the type of catalyst, but the reactivity of electrolyte

system with the superoxide radicals during the discharge process. Thus, when the electrolyte is free from the reduction by superoxide radicals, the ideal product Li_2O_2 is obtained regardless of existence of type of catalyst.

The much broader X-ray diffraction peaks for Li_2O_2 in the discharged electrode with catalyst may imply that the oxygen reduction process by catalyst may proceed with a different mechanism or reaction kinetics has changed. The activation overpotential by these catalysts must be different from the carbon surface, and this may explain the different reduction potentials. As a result, the physical properties of the discharge product such as product size, morphology or the crystallinity can be different as well as the ORR potential has a minor variations depending on the type of catalysts. In the case of ruthenate pyrochlore, as it is proposed in **Section 1.6**, oxygen is reduced to superoxide anion at OHP and adsorbs quickly on the surface of catalyst. Then, superoxide anion goes into the vacancy site at special oxygen site and further reduced to peroxide. Once the vacancy is nearly saturated with superoxide, the reduction potential is basically governed by superoxide to peroxide reduction process, which has a following equilibrium potential.

$$Pb^{2+}O_2^- + 2Li^+ + e^- \rightarrow Pb^{2+}\square + Li_2O_2 \quad (4\text{-}17)$$

$$E = E^o - \frac{RT}{F}\ln\left(\frac{a_{Pb^{2+}[]}\, a_{Li_2O_2}}{a_{Pb^{2+}O_2^-}\, a_{Li^+}}\right) \quad (4\text{-}18)$$

The equilibrium potential for this reaction is considered to be similar with the electrochemical reduction reaction from LiO_2 to Li_2O_2 [119,120].

$LiO_2 + Li \rightarrow Li_2O_2 \qquad \Delta G^o = -278.074$ kJ/mol $\quad E^o = 2.882$ V (4-19)

According to the work by P. G. Bruce et al., the catalytic activity of α-MnO_2 nanowire is related with its property to intercalate lithium ion and oxygen as well as high surface area from nanowire morphology and homogeneous distribution of catalyst [121]. However, the discharge potential is substantially lower than those pyrochlore catalysts after the initial voltage plateau up to around 1000 mAh g^{-1}, which means the catalytic activity for ORR is lower than the pyrochlore catalyst.

The galvanostatic oxidative decomposition of lithium peroxide shows that all the pyrochlore catalysts show the similar constant decomposition potential around 4.0 V at the first cycle, similar with those for PC electrolyte, which involves decomposition of lithium oxalate. However, the decomposition potential becomes lowered at the 2nd cycle around 3.9 V. The anodic electrochemical reaction for lithium peroxide decomposition in 1 M $LiPF_6$ / TEGDME electrolyte is given as follows.

$Li_2O_2 \rightarrow O_2 + 2Li^+ + 2e^-$ (4-20)

The possible decomposition mechanism of Li_2O_2 by pyrochlore catalyst is briefly addressed in **Section 1.6**, which involves Ru^{4+}/Ru^{5+} redox couple in Ru_2O_6 framework and vacancy at special oxygen position. A more detailed mechanism for pyrochlore catalysts will be discussed in **Section 4.7**. The charging curve for the cathode without any catalyst shows the decomposition of small amount of Li_2O_2 (about 1g of Li_2O_2 per 1g of carbon, ~ 1000 mAh g^{-1}) near 4.0 V. The capacity related with this anodic potential is not considered be from OER,

but it actually involves the carbon corrosion [129-131]. The surface modification of amorphous carbon by hydrogen peroxide is one of the most common methods to produce hydrophilic moiety [131-134]. In a similar way, lithium peroxide can oxidize the amorphous carbon surface, which has a lot of reactive dangling bonds on the surface, producing plenty of oxygen containing functional groups. Once all the surfaces are oxidized, carbon cannot contribute to the decomposition of Li_2O_2 any more. In the case where catalyst is present on the cathode, further decomposition can proceed by the action of the catalyst. The discharge curve for the 2nd cycle for the cathode containing only carbon shows a loss of catalytic activity of carbon surface; i.e. much decreased capacity and lowered discharge potential as cathode is already full of un-decomposed Li_2O_2, and the recovery of the oxidized carbon by reducing process is limited. The decomposition of Li_2O_2 at the 2nd cycle for this electrode is also limited because most of carbon surface is already oxidized, and it no longer functions as a catalyst as shown in **Figure 4.16a, b**. However, for pyrochlore catalysts, the discharge-charge curves at the 2nd cycle exhibits even better performance than the 1st ones. This proves that the high catalytic activity of pyrochlore catalysts really exists because the ORR / OER at the 2nd cycle occur mostly by the action of catalysts.

The charging curves for the Li-oxygen cell with α-MnO_2 nanowire at the 1st and 2nd cycles have similar characteristics as the ones without a catalyst although α-MnO_2 produces much more capacity. Especially, it does not show any catalytic activity at the 2nd cycle where the catalytic activity of α-MnO_2 should play a major role. This implies that α-MnO_2 nanowire does not act as a good catalyst for Li_2O_2 decomposition in this electrolyte. This observation is in the same context with the results that α-MnO_2 does not show a good catalytic activity for Li_2O_2 decomposition in LiBOB/PC electrolyte.

The discharge capacity of Li-oxygen cells with cycling is shown in **Figure 4.17**. For pyrochlore-catalyzed cells, the discharge capacity increases up to the 3rd cycle while fading occurs from the 2nd cycle for cathodes without a catalyst and with α-MnO_2 catalyst. It is believed that the general decrease in the discharge capacity after a few cycles for pyrochlore-catalyzed electrode is due to the oxidation of lithium anode and subsequent impedance development as a thick oxidation layer is found on the anode surface after disassembly after the electrochemical cycling.

4.5 Effect of gold decoration on catalyst

Some amount of gold (roughly 26 wt. %) was deposited on the surface of pyrochlore catalyst by chemical decomposition of $HAuCl_4$, and its effect on the electrochemical performance was evaluated by galvanostatic cycling. Gold is conventionally known as a good oxygen reduction catalyst in the aqueous solution through promoting ORR via the peroxide route [88]. Recent works on the application of gold catalyst to Li-oxygen cell exhibit that gold is an excellent catalyst for ORR even in the aprotic solution [119,120,221,231]. It exhibits higher discharge potential and larger capacity than glassy carbon does. They speculated that the increased discharge capacity comes from the formation of Li_2O in addition to Li_2O_2. As they found that platinum nano-particle is a good catalyst for OER, they combined two metal species to use as a bifunctional catalyst [221]. A similar approach can be made by combining gold with pyrochlore catalysts, as ruthenate pyrochlore shows an excellent catalytic behavior for OER. Gold can promote the ORR reaction together with pyrochlore, but with a different reduction mechanism during the

discharge reaction. For the charging reaction, pyrochlore can act as a good catalyst for OER. As a counterpart for comparison, gold (about 26 wt. %) was also deposited onto the spherical silica nano-particles in the same way, and its electrochemical performance for Li-oxygen cell was measured.

The charge-discharge curves and cycling stability of Li-oxygen cell for **nPRO,** gold-coated nPRO (**Au-nPRO**) and gold-coated silica (**Au-SiO_2**) catalysts together with bare carbon cathode without a catalyst in 0.5 M LiBOB/PC electrolyte are shown in **Figure 4.20a**.

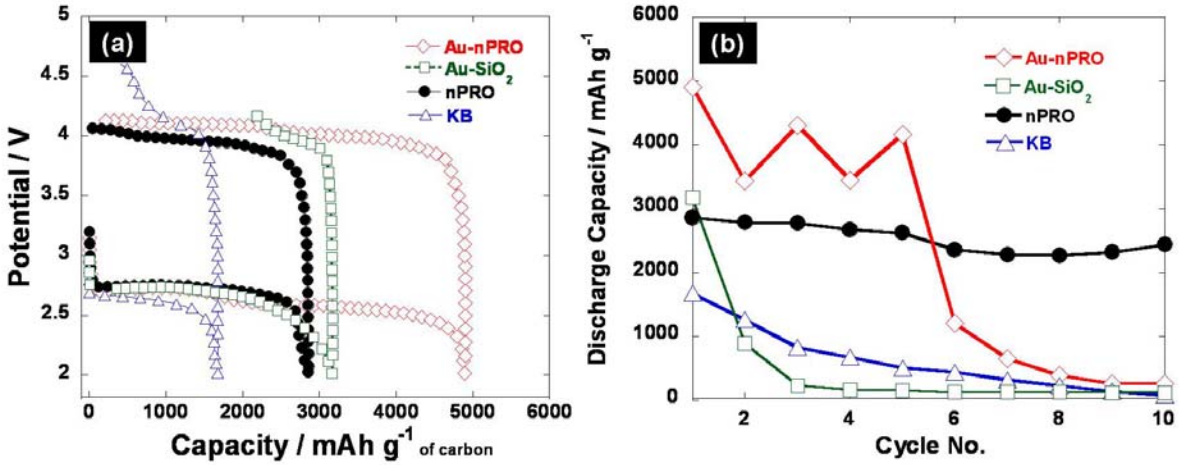

Figure 4.20 (a) Discharge-Charge profiles (the first cycle) of Li-oxygen cells with gold-decorated catalysts (**Au-nPRO**, **Au-SiO_2**) and (b) their cycling performances up to 10 cycles in 0.5 M LiBOB in PC electrolyte. The current rate is 70 mA per gram of carbon.

Both the discharge potential and the capacity of **Au-SiO_2** catalyst are higher than amorphous carbon, and they are comparable to those of **nPRO** catalyst. The similar tendency in the discharge curve was reported for the gold nano-particle-dispersed carbon black [119]. The discharge curve for **Au-nPRO** shows distinctive two-step discharge process. The discharge potential and the capacity from the first plateau are similar from those from either pyrochlore or gold catalyst alone as the first plateau has the same discharge potential ($E_{p1} = E_{p3}$) and

approximately the same discharge capacity (~ 3000 mAh/g) with the cell using pyrochlore catalyst, which is shown in **Fig. 4.20a** and in the differential capacity curves in **Figure 4.21**.

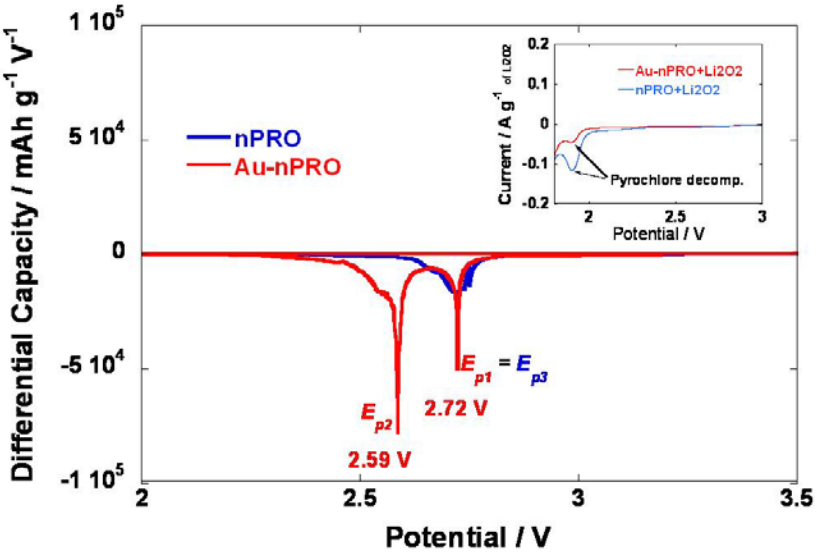

Figure 4.21 Differential capacities (dQ/dV) vs. potential curves for the 1st cycle of Li-oxygen cell with **nPRO** and **Au-nPRO** catalysts in 0.5 M LiBOB in PC electrolyte. E_{p1} and E_{p2} are reduction peaks for Li-oxygen cell with Au-nPRO catalyst and E_{p3} with nPRO catalyst. Inset shows cathodic potential sweep of Li_2O_2 electrode in a scan rate of 0.02 mV s^{-1} with Au-nPRO and nPRO catalyst.

Therefore, the actual reaction for the first peak is regarded to be the formation of superoxide and the subsequent reaction with LiBOB. This conclusion is also supported by the fact that the X-ray diffraction pattern and infrared spectrum for the discharged electrode with **Au-nPRO** catalyst exhibits similar results with those from just **nPRO** catalyst. The electrochemical reaction responsible for the second plateau is not clear, although it accounts for the almost half of the total discharge capacity. This reaction must be caused by a cooperative effect of gold and pyrochlore catalyst because this plateau did not appear in either one catalyst alone. This reaction is unlikely to be the reduction of Li_2O_2 further to Li_2O because Li_2O_2 electrode with **Au-nPRO** catalyst did not show any electrochemical

activity during the cathodic potential sweep down to 2.0 V (**Figure 4.21 inset**). It is possible that the reaction product formed by one catalyst is subject to further reduction by the other. For example, superoxide anions from the pyrochlore catalyst diffuse to gold surface to be further reduced to Li_2O before they meet BOB^- anions because in this potential range, most of the pores are already filled with $Li_2C_2O_4$ and the diffusion of bulky anions like BOB^- is slow and hindered by reaction deposit.

The **Au-SiO_2** catalyst did not show much catalytic activity for the anodic charging reaction as the charging curve shows similar behavior with the one of bare carbon electrode (**Fig. 4.21a**). A similar result for highly divided gold nano-particles on carbon black was also reported previously [119]. However, **Au-nPRO** catalyst exhibits much enhanced catalytic behavior showing comparable anodic overpotential compared with **nPRO** catalyst and complete decomposition of discharge product. This means that during the charge process, **nPRO** catalyst plays a major role in decomposing the reaction product from the discharge reaction. Therefore, the gold deposition on pyrochlore surface is effective way to increase the discharge capacity of Li-oxygen cell while maintaining its bifunctional property. This can be further evidenced by the cycling performance in **Figure 4.20b**, which exhibits the discharge capacity of Au-nPRO catalyst can maintain many cycles while **Au-SiO_2** catalyst does not show any cycling behavior.

The similar experiment was performed with 1 M $LiPF_6$ in TEGDME electrolyte as the main discharge product from this electrolyte is Li_2O_2. **Figure 4.22** shows the discharge-charge curves of the 1st cycle of Li-oxygen cells with **nPRO**, **Au-nPRO** and **Au-SiO_2** catalysts. Similar with the case for LiBOB in PC electrolyte, a Li-oxygen cell with gold coated pyrochlore exhibits a very high capacity about 14,000 mAh g^{-1}, which is more than

twice the discharge capacity of just pyrochlore catalyst. For this electrolyte, however, it shows a single discharge plateau around 2.65 V, which means only a single process, the formation of Li_2O_2 occurs, which is different from LiBOB/PC electrolyte. **Au-SiO_2** catalyst also shows a high discharge capacity of 8000 mAh/g with plateau potential around 2.65V. Therefore, gold is a quite effective catalyst for increasing discharge capacity, and combination with other catalysts results in the even higher discharge capacity.

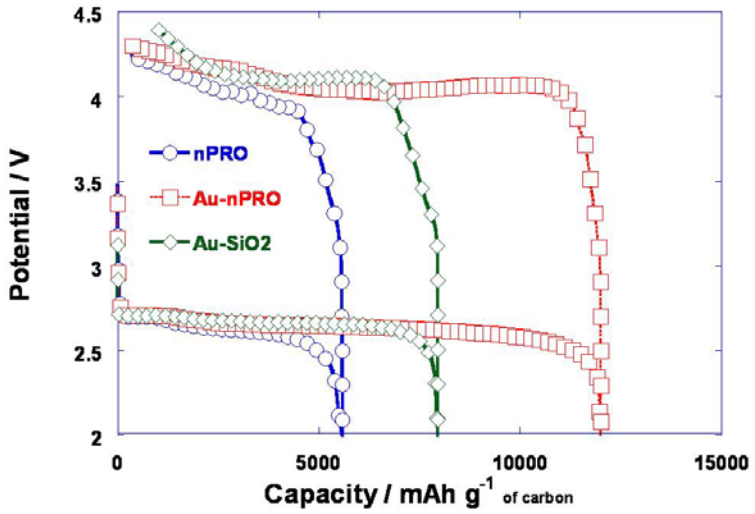

Figure 4.22 Discharge-Charge profiles (the first cycle) of Li-oxygen cells with gold-decorated catalysts (Au-nPRO, Au-SiO_2) in 1 M $LiPF_6$ in TEGDME electrolyte. The current rate is 70 mA per gram of carbon.

The charging curve for **Au-nPRO** shows that the Li_2O_2 decomposition potential is near 4.05V, which is slightly higher than just the pyrochlore catalyst, but its catalytic effect leads to almost full decomposition of the reaction product. In the case of **Au-SiO_2**, the Li_2O_2 decomposition potential is observed around 4.10 V, which is a bit higher than the **Au-nPRO** catalyst, but clearly exhibits catalytic effect. This shows different results from LiBOB/PC electrolyte where **Au-SiO_2** does not show any catalytic effect. This is simply caused by the fact that the reaction products from two electrolyte systems are different from each other.

However, some portion of the anodic charging curve for **Au-SiO_2** catalyst is considered to be contributed to the electrolyte decomposition as its cycling stability degrades considerably right after the 1st cycle and ether-based electrolyte is known to be unstable at high oxidation potential in the presence of certain catalyst [150,152]. On the contrary, the **Au-nPRO** catalyst exhibits a stable discharge capacity for several cycles (**Figure 4.23**), which implies that charge process is mostly involved with lithium peroxide decomposition only. The degradation in cell performance after a few cycles is certainly caused by the lithium corrosion, which results in the subsequent impedance development and the depletion of metallic lithium. The anode can be oxidized slowly chemically or electrochemically during the testing time. Therefore, there must be some protective measure on the lithium surface for improved performance.

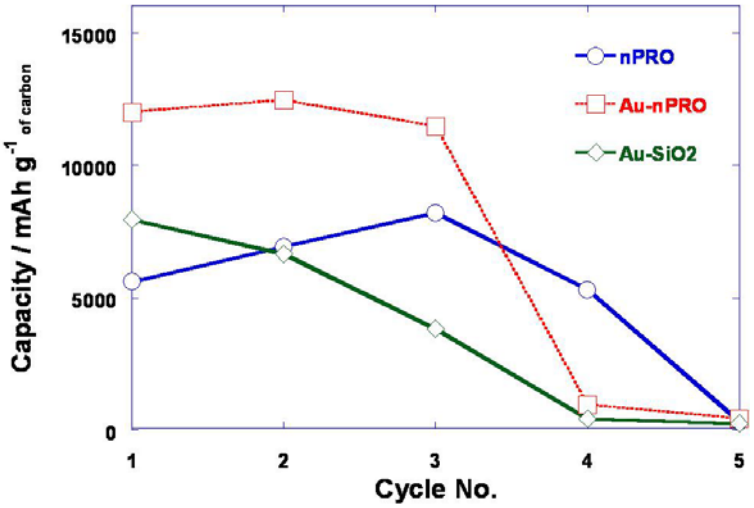

Figure 4.23 Cycling performances of Li-oxygen cells with gold-decorated catalysts (**Au-nPRO**, **Au-SiO_2**) up to 5 cycles in 1 M $LiPF_6$ in TEGDME electrolyte. The current rate is 70 mA per gram of carbon.

4.6 Lead ruthenate / Ketjen Black nano-composite as a catalyst

In the Li-oxygen cell, catalysts on the cathode play a key role, especially in increasing the discharge capacity, and more importantly, in reducing deplorable anodic overpotential for Li_2O_2 decomposition. Therefore, it is good to have as many catalysts as possible in terms of enhancing the cell performance. However, from a practical point of view, the amount of catalyst should be minimized while still maintaining reasonable cell performance because catalysts not only add an additional weight to the electrode, lowering the capacity based on total electrode mass, but increased commercial price [232,233] obviously worsens the economical considerations as well. In the constituent of pyrochlore catalysts, ruthenium belongs to the precious metals, and is actually one of the rarest metals on earth. Currently, ruthenium is found only as a minor component of platinum ores [234]. However, recently it is reported that ruthenium can be economically extracted from spent nuclear fuel in the future [235,236]. Fission product of U^{235} or Pu^{239} is relatively abundant in stable ruthenium isotopes (about 60 g per kg fissile), where Ru^{106} has the longest half life of 373 days (β^- decay to Rh^{106}) among radioactive isotopes [16]. After several decades of storage at the spent fuel repository, radioactivity can be reduced significantly compared with the original and commercial use of ruthenium becomes theoretically possible [235]. Anyway, considering its high commercial stock price (~$5000/kg) currently compared with for example, bismuth (~ $20/kg), its use should be optimized to the minimum amount [232,233].

The fabrication of homogenous nano-particles is one of the most common methods to maximize catalytic effects because the kinetics of most catalytic reactions is surface area dependent. However, the high surface energy created by a large surface area of nano-particles often leads to the agglomeration causing much difficulty in homogenous dispersion

[153]. To elude this problem, a small amount of **nPRO** nano-particles were deposited on the carbon surface (named as **nPRO-KB**) through a wet coating process and used as a catalyst. Because **nPRO-KB** has almost the same morphological features with un-coated carbon serving as Li_2O_2 deposition sites, mixing of two components during the electrode manufacturing process is considered much more effective, and consequently much smaller amount of catalysts were added.

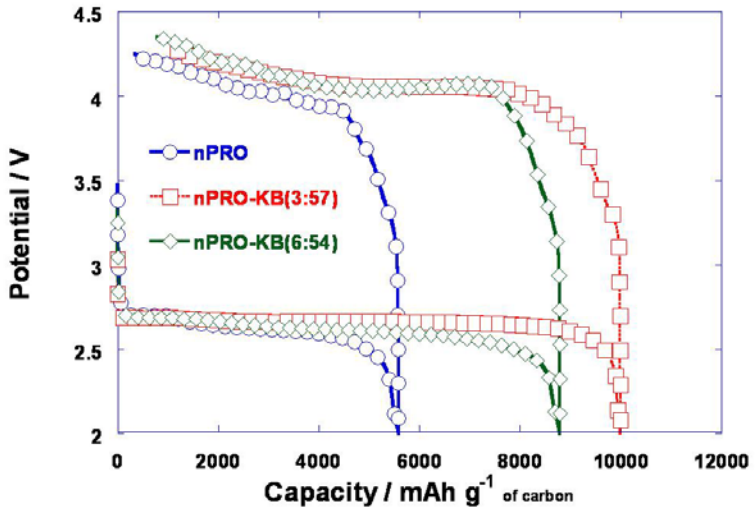

Figure 4.24 Discharge-charge profiles (the first cycle) of Li-oxygen cells with **nPRO** coated carbon as catalysts in 1 M $LiPF_6$ in TEGDME electrolyte. The current rate is 70 mA per gram of carbon. The ratio in the blank represents overall catalyst to carbon ratios.

Figure 4.24 shows the discharge-charge curves for Li-oxygen cells with **nPRO** and **nPRO-KB** catalysts. For **nPRO** catalyst, carbon was mixed with catalysts with 1: 1 wt. ratio and for **nPRO-KB** catalysts, electrodes with two different compositions were manufactured by mixing carbon with **nPRO-KB** catalyst with 5:1 and 4:2 wt. ratios. In other words, the carbon to ruthenate pyrochlore ratios for these electrodes correspond to 57: 3 and 54: 6 as pyrochlore accounts for 30 wt. % of the **nPRO-KB** catalyst. **Figure 4.24** shows that **nPRO-KB** catalyst produces much higher discharge capacity with similar discharge (2.65 V), and

charge (4.05 V) overpotentials than **nPRO** catalyst in two Li-oxygen cell tests with different compositions although they have much smaller amount of catalyst in the cathodes with **nPRO-KB** catalysts. This is probably caused by the fact that much more efficient pore formation is possible by mixing carbon and catalyst with similar size and morphology while maintaining catalytic effect by highly-dispersed nano-particle deposited on the carbon surface. The cycling performance of **nPRO-KB** also shows a similar behavior with bare pyrochlore catalyst and is stable up to the 3rd cycle (**Figure 4.25a**). The calculated discharge capacity based on the total cathode mass including O_2 from the air (**Equation 1-20** with r = 0.32) is shown in **Figure 4.25b**. The **nPRO-KB** catalyst generates over 1000 mAh per gram of total electrode mass whereas pyrochlore catalyst 720 mAh g^{-1} at the first cycle. The fading after the 3rd cycle is believed to be caused by the oxidation of lithium anode. Therefore, the amount of catalyst needed for a high catalytic performance can be greatly reduced by manufacturing nano-particle coating on the carbon. The **nPRO** catalyst with only 5 wt. % of total carbon mass is enough to achieve an efficient catalytic effect for the Li-oxygen cell.

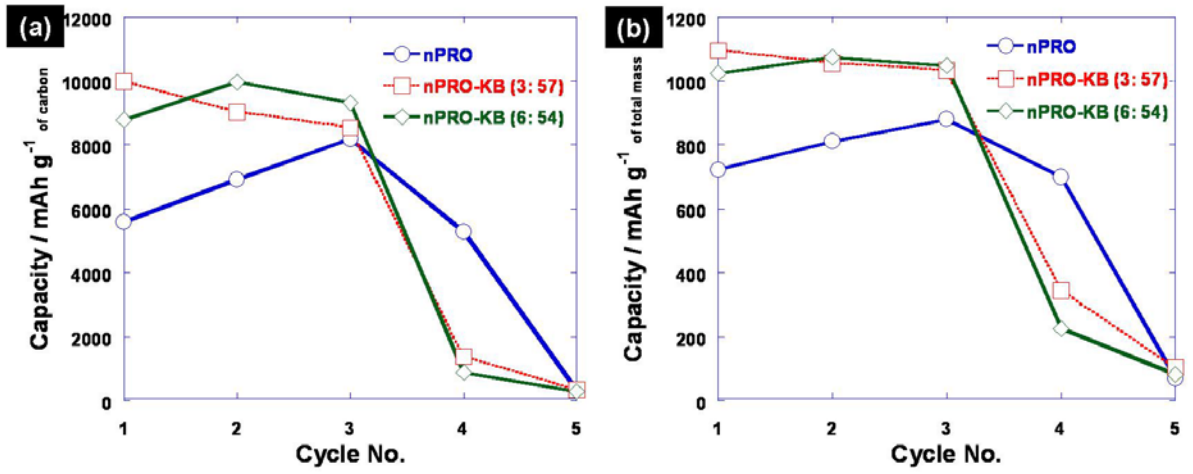

Figure 4.25 Cycling performances of Li-oxygen cells with **nPRO** coated carbon as catalysts in 1 M $LiPF_6$ in TEGDME electrolyte up to 5 cycles in terms of capacity based on (a) carbon amount and (b) total electrode mass. The current rate is 70 mA per gram of carbon.

The discharge capacity with slightly lower rate 60 mA/g (for all the other data, the current rate is set to 70 mA/g) exhibits 25 % increase in the discharge capacity without any significant change in cathodic and anodic overpotentials (**Figure 4.26**). This is probably due to the fact that much efficient packing of Li_2O_2 within pores is possible when lower current is applied.

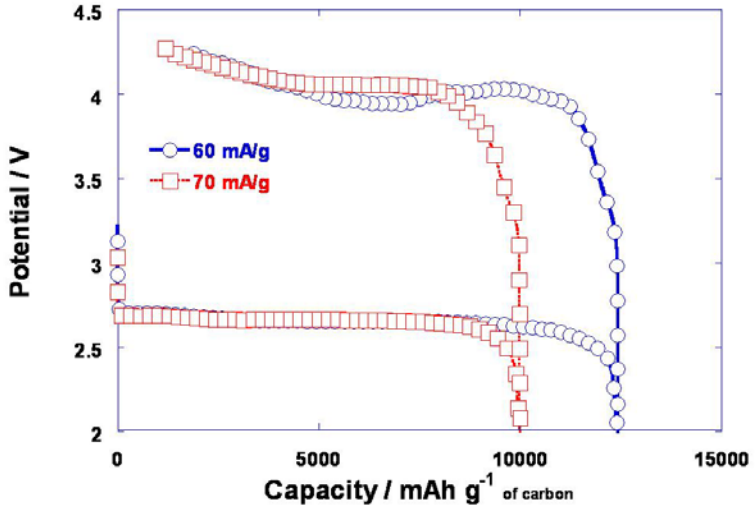

Figure 4.26 Discharge-charge profiles (the first cycle) of Li-oxygen cells with nPRO coated carbon as catalysts in 1 M $LiPF_6$ in TEGDME electrolyte depending on the current rate applied (60 mA/g and 70 mA/g).

4.7 Decomposition mechanism

From the previous results, we observed that the cycling stability and overall energy efficiency of the Li-oxygen cells are critically dependent on the efficient decomposition of the discharge product, Li_2O_2, during charge process, where well-dispersed catalyst plays an important role in overcoming a huge activation barrier posed by the insulating property of discharge product [99,121]. The oxidative decomposition of discharged product Li_2O_2 from

1 M $LiPF_6$ in TEGDME is further investigated by low scan rate (0.02 mV s^{-1}) potential sweep method. The cathode containing Li_2O_2 initially was subject to slow anodic scan until the electrochemical signals from major electrolyte decomposition is observed [97,114]. The Li_2O_2 electrode was manufactured and the electrochemical cells were tested in the same manner with those for 0.5 M LiBOB in PC electrolyte.

Figure 4.27 shows the anodic Li_2O_2 decomposition behavior when no catalyst is present on the cathode. The curves obtained from the anodic scan of the carbon electrode without presence of Li_2O_2 under O_2 or Ar atmosphere are also shown as baseline curves to check the starting potentials for the oxidative decomposition of electrolyte and the carbon corrosion by oxygen molecules. Certainly, in the presence of oxygen, the carbon corrosion starts to occur near 4.30 V vs. Li/Li^+ before major electrolyte decomposition (4.60 V) happens. It seems that the oxidized carbon surface is inefficient even for further electrolyte decomposition.

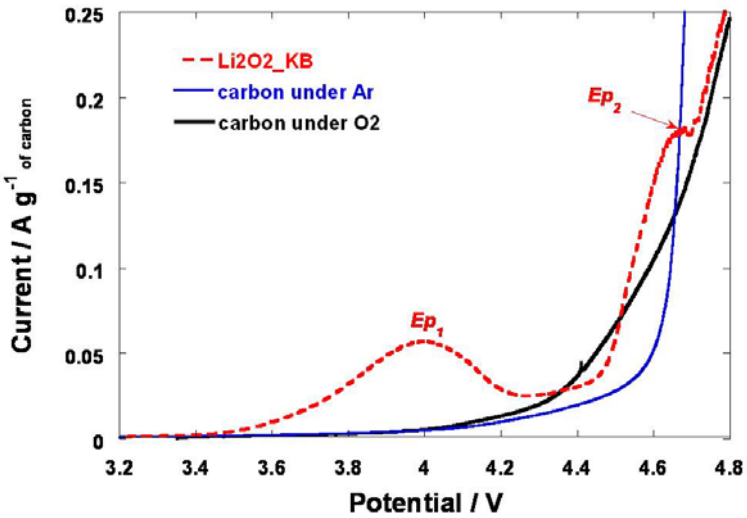

Figure 4.27 Potential sweep measurements of Li_2O_2 electrodes without catalyst in 1M $LiPF_6$ in TEGDME electrolyte in Ar showing an electrochemical decomposition of Li_2O_2 with peak potentials indicated. The scan rate is 0.02 mV sec^{-1}. The **carbon under Ar** and **carbon under O_2** represent two baseline curves to check electrolyte decomposition under argon and oxygen atmosphere, respectively.

The anodic potential sweep of Li_2O_2 electrode shows the electrochemical peak around 4.00 V (***Ep₁***) and 4.65 V (***Ep₂***). The electrochemical peak at 4.00 V must not be related with the electrolyte decomposition because anodic scan of carbon without Li_2O_2 does not show such an electrochemical activity. Therefore, it is certain that this peak is involved with Li_2O_2 decomposition. However, ***Ep₁*** is not considered to be OER, but this peak represents the electrochemical oxidation of carbon surface [129-134] by Li_2O_2 as following reaction is plausible.

$$C_n + Li_2O_2 \rightarrow C_nO_2 + 2Li^+ + 2e^- \quad (4\text{-}21)$$

Similar chemical surface modification of carbon by H_2O_2 in the aqueous solution generates H_2 evolution leaving a lot of hydrophilic surface functional groups [131,134]. The charge capacity for this reaction accounts for 354 mAh g^{-1}, which corresponds to approximately 0.3 gram of Li_2O_2 per 1 gram of carbon. It seems that once it is oxidized, the carbon surface becomes inactive for further Li_2O_2 decomposition, which occurs only at high anodic potential around 4.65 V. At this potential range, direct oxidation of carbon surface by oxygen molecules and electrolyte decomposition occur together. This suggests that for the efficient OER and the protection of carbon surface, catalysts should be present and decompose Li_2O_2 at least before carbon corrosion by oxygen molecules (4.3 V) occurs. It would be even better if catalytic decomposition proceeds before carbon corrosion by Li_2O_2 occurs.

Figure 4.28 shows the curves for the anodic potential sweep of pyrochlore-catalyzed Li_2O_2 electrode with baseline curves for carbon oxidation and electrolyte decomposition.

The background electrochemical result shows that the carbon oxidation and the electrolyte decomposition start much earlier in the presence of pyrochlore catalyst than those without catalyst. It is known that ether-based electrolyte can be decomposed much earlier in the presence of certain catalysts [150]. Both reactions start around 4.00 V and grow significantly after 4.20 V for carbon oxidation (possibly electrolyte decomposition is also included) and 4.50 V for electrolyte decomposition.

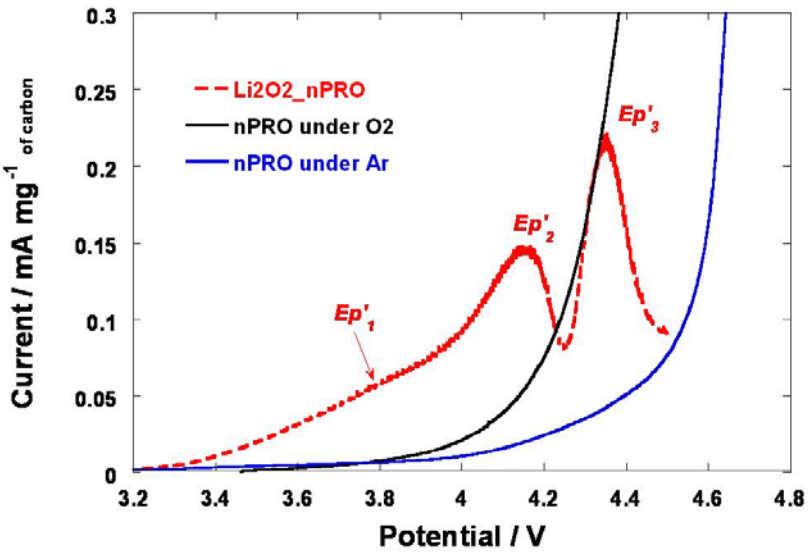

Figure 4.28 Potential sweep measurements of Li_2O_2 electrodes with **nPRO** catalyst in 1M $LiPF_6$ in TEGDME electrolyte showing an electrochemical decomposition of Li_2O_2 with peak potentials indicated. The scan rate is 0.02 mV sec^{-1}. The **nPRO under O_2** and **nPRO under Ar** represent two baseline curves for checking electrolyte decomposition under oxygen and argon atmosphere when pyrochlore catalyst is present.

The electrochemical activity from Li_2O_2 electrode with pyrochlore catalyst is made up of three major peaks, which are located at 3.80 V (***Ep'*$_1$**), 4.15 V (***Ep'*$_2$**), and 4.35 V (***Ep'*$_3$**). The first peak (***Ep'*$_1$**) is related with OER from Li_2O_2 decomposition by the action of Ru^{4+}/Ru^{5+} redox couple in Ru_2O_6 framework of the pyrochlore structure as it is described in **Section 1.6**, and the reaction scheme is reproduced below for the convenient reference. This OER reaction can occur anodic of the potential for Ru^{4+}/Ru^{5+} oxidation, which is observed at 3.30

V from **Figure 4.5**. This potential roughly corresponds to the starting point of Li_2O_2 decomposition in **Figure 4.28**. In this potential range, the Li_2O_2 just near the pyrochlore catalyst decomposes to lithium ion and oxygen molecules.

$$Pb^{2+}\square + Li_2O_2 \rightarrow Pb^{2+}O_2^{2-} + 2Li^{+} \quad (4\text{-}22)$$

$$Ru^{4+}O^{2-} + Pb^{2+}O_2^{2-} \rightarrow Ru^{5+}O_2^{2-} + Pb^{2+}O^{2-} + e^{-} \quad (4\text{-}23)$$

$$Ru^{5+}O_2^{2-} \leftrightarrow Ru^{4+}O_2^{-} \quad (4\text{-}24)$$

$$Ru^{4+}O_2^{-} + Pb^{2+}O^{2-} \rightarrow Ru^{4+}O^{2-} + Pb^{2+}\square + O_2\uparrow + e^{-} \quad (4\text{-}25)$$

The potential for the second step (**Reaction 4-23**) controls the overall charge overpotential and it depends on the removal rate of peroxide in the third step (**Reaction 4-24**) where faster conversion of peroxide to superoxide leads to lower equilibrium potential (and thus lower oxidation potential) for the 2nd step. The rough expression for equilibrium potential for this process can be written as follows.

$$E = E^{o} - \frac{RT}{F}\ln\frac{a_{Ru^{4+}}}{a_{Ru^{5+}}} \quad (4\text{-}26)$$

The second peak (***Ep'₂***) in **Figure 4.28** represents the decomposition of Li_2O_2 where the diffusion of Li_2O_2 to the catalyst site in the first step (**Reaction 4-22**) plays a role in the electrochemical reaction at the second step. The maximum current density is controlled by the diffusion flux of Li_2O_2 to the catalyst site through expanding diffusion boundary, which depends on the concentration gradient and diffusivity of Li_2O_2 on the oxidized carbon surface. However, as the amount of Li_2O_2 on the cathode is limited, the current density starts

to fall at some point as shown in **Figure 4.28**. The diffusion flux is also related with the geometric factors like homogenous distribution of catalyst and Li_2O_2. The anodic capacity up to 4.25 V including Ep'_1 and Ep'_2, accounts for 929 mAh/g which corresponds to 80 % of the full decomposition of Li_2O_2. Therefore, the third peak (Ep'_3) must not be completely related with Li_2O_2 decomposition because the anodic capacity involved with this peak is about 455 mAh/g. The comparison with the baseline curve for anodic scan under O_2 indicates that Ep'_3 actually corresponds to the carbon oxidation or electrolyte decomposition by catalyst. Because the amount of oxygen evolving from the given amount of Li_2O_2 is limited, they show a limit in the amount of carbon oxidation and electrolyte decomposition as shown in **Figure 4.28**. The above explanation is further confirmed by the ex-situ X-ray diffraction measurements for the electrodes charged up to a certain potential during the anodic scan, which is described in **Figure 4.29a, b**.

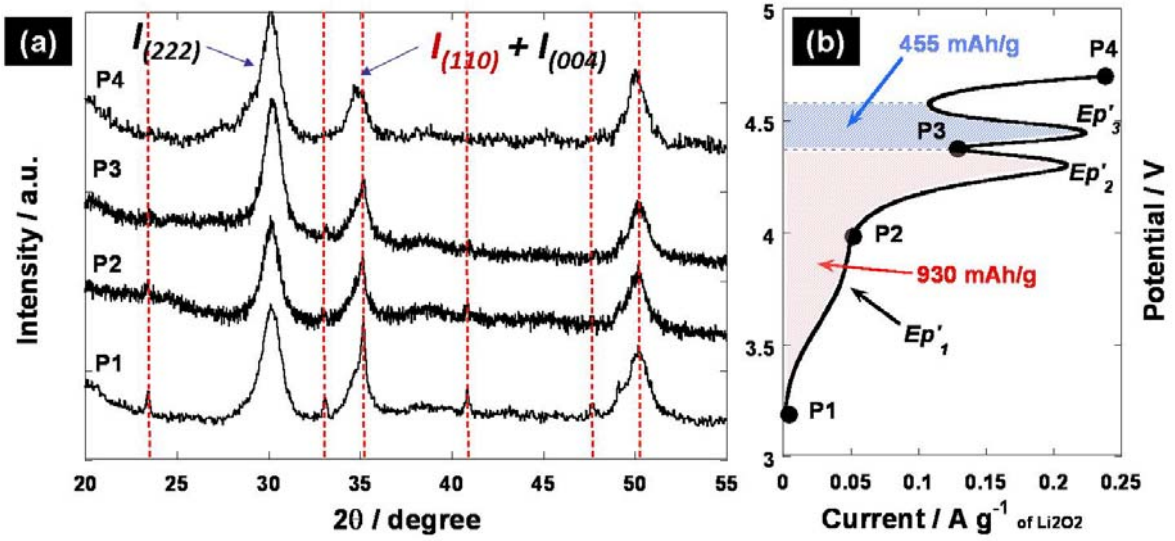

Figure 4.29 (a) Ex-situ X-ray diffraction patterns of Li_2O_2 electrode with nPRO catalyst (Li_2O_2_nPRO) after charging up to particular potentials and (b) one representative result of potential sweep measurement of Li_2O_2_nPRO and the location of cutoff potentials for XRD measurement. The dotted line in (a) represents the XRD peak position of Li_2O_2.

The relative amount of Li_2O_2 in the cathode during the anodic scan compared with the initial amount was estimated from the change in the intensity ratio between (110) reflection of Li_2O_2 and (222) reflection of catalyst (**Table 4.3**). However, as the (004) reflection of catalyst almost coincide with (110) reflection of Li_2O_2, the ratio was corrected by subtracting the contribution from (004) reflection of catalyst from (110) reflection assuming at $\mathbf{P_4}$, virtually no Li_2O_2 is left. At $\mathbf{P_2}$ charged up to 4.00 V, almost 55 % of Li_2O_2 is decomposed and at $\mathbf{P_3}$ (4.25 V) more than 90 % of Li_2O_2 is decomposed, which is in reasonable agreement with the analysis of the electrochemical data. Therefore, $\boldsymbol{Ep'_3}$ represents mostly the carbon oxidation by O_2 gas evolved from OER or electrolyte decomposition.

Table 4.3 The intensity ratio $I_{(110)}$ / $I_{(222)}$ from the ex-situ X-ray diffraction patterns for the electrode charged up to a certain potential. The amount of L_2O_2 is estimated assuming at P_4 no Li_2O_2 is left.

ratio \ position	P1	P2	P3	P4
$(I_{(110)} + I_{(004)}) / I_{(222)}$	0.84	0.61	0.44	0.42
$I_{(110)} / I_{(222)}$	0.42	0.19	0.03	0.00
Li_2O_2 left	100	45	6	0

The electrochemical impedance was measured for the electrode made of carbon black and Li_2O_2 without catalyst (Li_2O_2_KB) while the potential of cathode increases stepwise over Li_2O_2 decomposition potential to investigate if the disintegration of Li_2O_2 near 4.0 V accompanies any impedance growth from the surface modification by carbon oxidation (**Figure 4.30a, b**). The cathodic potential was raised by 130 mV at a time from the open circuit voltage (OCV) vs. Li/Li^+ and maintained for 5h before impedance measurement. Meaningful decomposition starts to occur at 3.7 V and stopped around 4.2 V (**Figure 4.30b**).

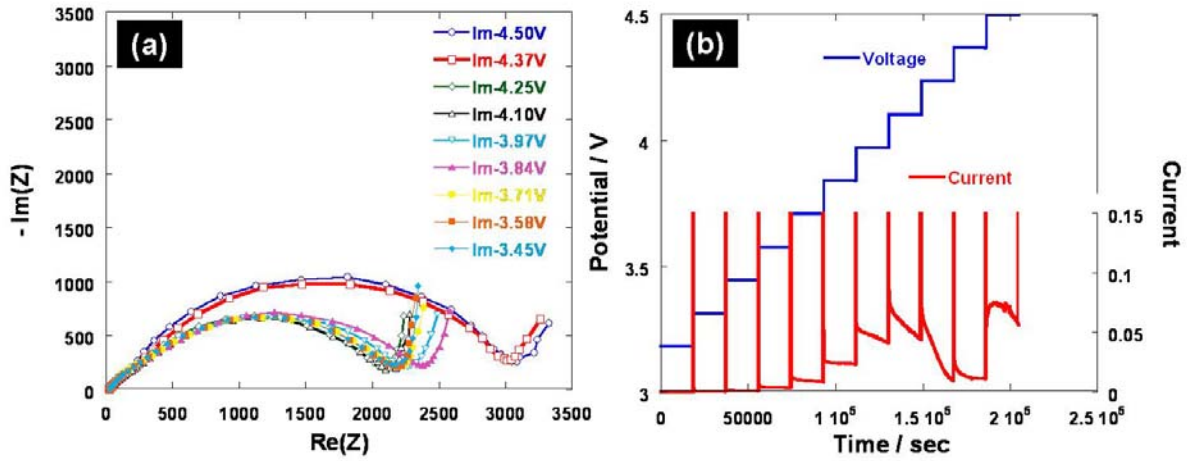

Figure 4.30 (a) Electrochemical impedance measurements at various potential steps of Li_2O_2 electrode without catalyst (Li_2O_2_KB) and (b) step-wise charging of Li_2O_2 electrode. Potential was held at any particular value for 5 h before impedance measurement. Impedance was scanned from 10^5 – 10^{-2} Hz.

The impedance data obtained was analyzed based on the equivalent circuit shown in **Figure 4.31a**, which is mainly composed of charge transfer part and space charge layer part. The experimental data was fitted to the model by ZView™ software. After Li_2O_2 decomposition around 4.0 V, the impedance of the cell rises suddenly over 4.37 V. This increase is mainly contributed by the sharp growth in charge transfer resistance (R_{ct}) as in **Figure 4.31b**. This is probably caused by the fact that the initial Li_2O_2 decomposition makes the carbon surface incapacitated for further reaction (i.e. oxygen evolution reaction, ORR) as all the active sites are covered by an oxide layer. Therefore, without catalyst, the extent of Li_2O_2 decomposition will be severely limited by carbon corrosion process. However, an influence of thin oxide layer on overall electrical resistance is considered to be insignificant because the contribution of the impedance by space charge layer [237] of oxidized carbon surface (included in R_f together with charge transfer resistance on anode) is not large from the impedance data analysis.

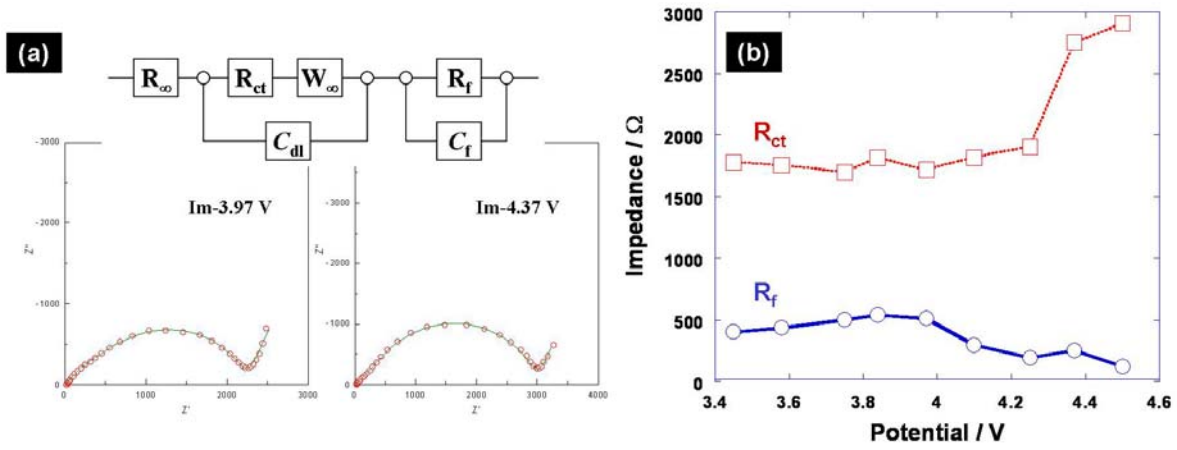

Figure 4.31 (a) Equivalent circuit [238] employed for the analysis of impedance data with curve fitting results (green lines) and (b) development of charge transfer resistance on cathode (R_{ct}) and anode (R_f) during stepwise anodic polarization. R_∞ represents resistance from electrolyte, C_{dl} is double layer capacitance on cathode side, W_∞ denotes Warburg impedance caused by diffusion of Li^+ ion at low frequency region and C_f means double layer capacitance on anode side or capacitance from space charge layer in the oxidized carbon surface on cathode. For the actual curve fitting, CPE elements are used to fit the curve instead of capacitors (C_{dl}, C_f) because of the obvious depression of semi-circles.

4.8. Conclusion

The Li-oxygen cell is an emerging energy storage system which has a great promise in the near future for its high theoretical energy density over 3500 Wh kg^{-1} and use of 'free' oxygen from the air. This energy system produces nine times higher energy density than commercial lithium-ion cells based on intercalation chemistry (~ 400 Wh kg^{-1}).

However, several critical problems are yet to be solved before it could be considered for any practical application. Firstly, the formation of the insulating and insoluble reaction product, lithium peroxide requires the highly porous and electronically well percolated cathode structure for reasonable performance. Secondly, the inherent high activation energy needed for the decomposition of lithium peroxide leads to the huge anodic overpotential, which demands the development of highly efficient catalyst. Thirdly, the electrolyte system

should be resistant to both the superoxide attack during the discharge reaction and the highly oxidizing environment during the charge process where both oxygen radicals and catalysts are present. Lastly, the proper protection of lithium anode is necessary otherwise dissolved oxygen in the solvent will react with lithium metal spontaneously, which increases the impedance, and more importantly depletes lithium metal from the anode.

This thesis is primarily focused on the development of highly efficient catalyst system for oxygen reduction and oxygen evolution reactions for Li-oxygen battery. To this end, highly porous and electrically networked cathode films were manufactured by utilizing common plasticizers as pore forming agents. The Li-oxygen cell test in two different electrolyte systems shows that the reactivity of electrolyte system to superoxide radicals is a key parameter to determine the nature of reaction product. For the LiBOB/PC system, both LIBOB and PC are actively decomposed by superoxide radicals to produce lithium oxalate and lithium carbonate as main discharge products. In the case of $LiPF_6$/TEGDME system, both salt and solvent are stable, and thus, ideal discharge product, lithium peroxide is obtained. The lead ruthenate and bismuth ruthenate with the extended pyrochlore structure show excellent catalytic behavior by increasing discharge capacity and lowering the anodic overpotential considerably during charge process. They reduce the decomposition of electrolyte system and the extent of carbon corrosion, which accounts for more efficient cycling. The excellent catalytic activity of these pyrochlores is due to their intrinsic oxygen vacancies, electronic conductivity and many surface active sites afforded by its morphology. The performance of this catalyst was further increased through gold deposition on the pyrochlore surface resulting in much increased discharge capacity. The pyrochlore coated carbon was proposed as a type of catalyst for an efficient way to reduce the amount of

catalyst and enhancing homogenous mixing with other components. The investigation on the lithium peroxide decomposition mechanism tells that carbon corrosion, which occurs at around 4.0 V by lithium peroxide makes further decomposition difficult without a catalyst. However, in the presence of pyrochlore catalyst, Li_2O_2 decomposition reaction can proceed to completion even though carbon corrosion still occurs. This gives a hint that the generation of nano-porous structure and the homogenous distribution of nano-sized catalyst over these pores are very important as well as use of highly efficient catalysts for low activation overpotential.

V. Ruthenium Dioxide as a Supercapacitor Material

5.1 Mesoporous RuO_2 as a supercapacitor

The synthesis of hexagonally ordered mesoporous silica MCM-41 [180-182] two decades ago introduced a revolutionary new method for preparing various 2-D and 3-D periodic materials. Extension to mesoporous transition metal oxides (MTMOs), however, still remains as a considerable challenge for redox-active metals [189]. MTMOs are of substantial interest because of their characteristic functional properties and ability to adopt a wide range of valence states. They have immense potential for control of catalytic and photocatalytic reactions [239,240]; separation or storage of ions/electrons/molecules for energy conversion and storage [241,242]; as redox active surfaces for electrochemical reactions [212,243]; and as chemical sensors [244]. A relatively crystalline wall structure is often highly desirable for these applications. A good example is metallic RuO_2 which has many functional properties that are highly dependent on its crystalline nature, surface area and accessibility of the redox centers. This metallic oxide is reported to be an excellent catalyst for CO oxidation [245], an interesting lithium-ion battery electrode material [211,215], and is especially regarded as being amongst the most promising electrode materials for supercapacitor applications in the last decade [157,158,162,183,184]. Its high fundamental energy storage capability derives from pseudo-capacitance arising from the surface redox reactions of RuO_2. They involve the simultaneous injections of protons and electrons [246]:

$$RuO_a(OH)_b + x\ H^+ + x\ e^- \leftrightarrow RuO_{a-x}(OH)_{b+x} \quad (5\text{-}1)$$

The capacitive storage and rate capability are greatly enhanced when the electronic and protonic transport are optimized in concert. The key to this is establishing a continuous nanocrystalline network that maintains low-defect metallic conduction pathways, but also possesses a sufficient surface area and hydration for proton access. While it is possible to synthesize high surface area RuO_2 that exhibits a textural porosity by virtue of tiny crystallite dimensions, tailoring a framework to possess long-range structural micro and mesoporosity has proved more demanding. Thus, the direct formation of highly porous hydrated crystalline RuO_2 without collapse of the wall structure and subsequent loss of integrity remains as a major challenge. This is common to most porous transition metal oxides. Their tendency to disintegrate during template removal and/or annealing derives from the thermodynamic forces that drive the formation of a dense crystalline structure favored by TMO's.

Previous research on MTMO's based on high or fixed oxidation state metal oxides shows that they can be prepared by approaches that can generally be divided into two classes. The soft or direct template route is based on a one-pot synthesis of metal oxides using surfactants as structure-directing reagents, as in the case of silica. Although the resulting metal oxides often exhibit fragile amorphous frameworks that undergo the above-mentioned collapse on heating, several fixed oxidation state metal oxides such as zirconia, titania, alumina, niobia and tantala have recently been prepared by this method. The more successful nanocasting route involves a hard-templating approach that relies on an inverse template method. The scaffolds (e.g., mesoporous silica or carbon, and polymer or silica lattices) are

used to nucleate the metal oxide structure, and are then removed via etching or calcination. The nanocasting route is cumbersome, though: the templates must be removed by aqueous leaching in hot NaOH or HF solutions, a process that can result in structural degradation. Nonetheless, many MTMO's have been synthesized by this method, including Fe_2O_3 [247], β-MnO_2 [98], Co_3O_4 [248], NiO [249] and CuO [195]. Mesoporous RuO_2 has also been prepared via nanocasting, but the material was very poorly ordered and displayed low-intermediate surface area [245]. A clever approach to obtain crystalline mesoporous metal oxides uses the high-temperature crystallization of amorphous metal oxides in the presence of glassy phases such as silica [250], phosphorus oxide [250,251], and carbon [187]. The filled amorphous glass phases provide structural support, and inhibit the growth of nanocrystals during the high-temperature treatment, thus reinforcing the mesoporous frameworks. This has resulted in TiO_2 and Nb_2O_5 with highly crystalline frameworks to date [187].

Herein, we describe the first direct low-temperature, liquid crystal surfactant template - crystallization route from aqueous solution to form a quasi-ordered crystalline mesoporous RuO_2•$0.4H_2O$. The high fundamental specific capacitance of RuO_2, along with a long cycle life, electrical conductivity, excellent charge/discharge rates, and good reversibility [183,184] has inspired much effort to elaborate its morphology. Supporting RuO_2 on carbon greatly increases the available surface area, for example, but at the expense of greatly reducing the density. Our method constitutes a novel direct approach to the crystalline oxide, which is constructed of nanosized metal oxide building blocks on the order of several nano-meters in size that are assembled into thin walls. In this approach, cationic surfactants serve as pore-directing agents instead of nonionic surfactants or inverse templates as previously

reported. We selected hexadecyl-trimethylammonium chloride, $C_{16}TMA^+Cl^-$, which can participate in an indirect $S^+X^-I^+$ interaction [181,190,196] mediated by the chloride ion, and thus coordinate a cationic ruthenium nitrosyl precursor. Gentle decomposition of the initially formed mesostructured metal cation−surfactant composite leads to crystallization of the wall structure as NO is released. The metal cations are cross-linked to form M−O−M bonds, and transformed into the nanosized $RuO_2 \bullet xH_2O$ building blocks. The slow oxidative hydrolysis and condensation of the ruthenium oxide precursor are critical to the low-temperature crystallization process necessary to the synthesis. The nanocrystals further form three-dimensional networks during calcination to remove the surfactant. The promising electrochemical properties of our porous $RuO_2 \bullet xH_2O$ result from a more highly ordered structure and almost tripled surface area (190 $m^2\ g^{-1}$) compared to that obtained from the nanocasting method [245]. Crystalline mesoporous $RuO_2 \bullet 0.4H_2O$ exhibits a high capacitance of 410 F g^{-1} and good rate capability, and the amorphous mesoporous $RuO_2 \bullet 1.3H_2O$ reported here displays capacitance of over 700 F g^{-1}. In view of the wide applications of RuO_2 as described above, these new materials may also open up other avenues of research.

5.2 Experimental setup

For the capacitance measurements of $RuO_2 \cdot xH_2O$ with different degree of dehydration , the cyclic voltammetric behavior between 0 – 0.9 V (vs. Ag/AgCl) was examined in a three-electrode electrochemical cell in a 0.5 M H_2SO_4 aqueous solution, using platinum wire as the counter electrode and Ag/AgCl as the reference electrode (0.22249 V vs. NHE at 25 ^oC [83]). The working electrode was fabricated by mixing as-synthesized

mesoporous RuO_2 powder with 3 % polyvinylidene fluoride (PVdF) binder, and pasting the mixture on a stainless steel current collector. The typical loading of active material was calculated by difference and was approximately 2 mg cm^{-2}, and the effective electrode area was 0.6 cm^2. The average capacitance (C_{ave}) is taken from cathodic (q_c) and anodic (q_a) charges, mass (m) and potential span (ΔV) according to the following equations [184].

$$C_{ave} = \frac{\left(q_a + |q_c|\right)}{2m\Delta V} \qquad (5\text{-}2)$$

5.3 Results and discussion

Several mesoporous hydrous ruthenium oxides with different degree of hydration and wall crystallinity were synthesized by following the procedure in **Section 3.1**. To investigate their pseudo-capacitances, the materials were cast from slurries as "thick" conventional electrodes onto stainless steel current collectors, and electrochemically cycled in 0.5 M H_2SO_4 in the voltage range 0 ~ 0.9 V, at a scan rate between 2 and 200 mV s^{-1}. Cyclic voltammetry experiments conducted on the amorphous $RuO_2 \bullet 1.3H_2O$ (**mRO-2**) mesoporous electrodes heat-treated at 200 ºC for 12 h exhibited a high capacitance of 700 F g^{-1}, comparable to that of other hydrous amorphous ruthenium oxides that range from 600 ~ 900 F g^{-1} [157,252,253]. However, some irreversibility at low potential (**Figure 5.1a**), and poor retention of capacitance with increasing sweep rate (200 F g^{-1} at 20 mV s^{-1}) were observed, characteristic of amorphous hydrous RuO_2 [157,252,253]. Whereas the capacitive response benefits from the hydrous content that enables proton transfer, the poor electronic

conductivity of the amorphous framework impedes fast electron transport. The response of the capacitance vs. potential curves of the crystalline RuO_2•$0.4H_2O$ (**mRO-3**), however, displays a close-to-ideal rectangular shape and perfect electrochemical reversibility of the redox reactions. The capacitance of 410 F g^{-1} at 2 mV s^{-1} was only slightly lowered to 400 F g^{-1} on increasing the sweep rate to 20 mV s^{-1}. **Figure 5.1b** shows the variation of specific capacitance with a scan rate, indicating a very good retention. High capacitance (up to 1000 F g^{-1}) has recently reported for RuO_2•xH_2O films (55 nm in thickness) with a very large pore dimension of 15 ~ 30 nm prepared by an evaporation-self assembly (EISA) technique, but comparison is difficult owing to the ultra-thin (55 nm) nature of these films [254]. The capacitance value we report here measures up reasonably well, taking into account the fact that our materials properties are reported for bulk cast electrodes, and that electronic contact to the current collector and transport are enhanced by up to a factor of 5-10 for thin membranes. The values we report are comparable or superior to other "bulk" cast crystalline RuO_2•xH_2O materials at similar sweep rates (e.g. 75 F g^{-1} at 20 mV s^{-1}V;[13]and 350 F g^{-1} at 2 mV s^{-1}V).[31] This performance can be attributed to the 3D interconnected network of pores and framework, which facilitates ion and electron transport. The mesoporous network of RuO_2•xH_2O also reduces the resistance to electrolyte penetration, and the nanoscopic RuO_2•xH_2O crystallites promotes a rapid proton exchange, and electron transfer.

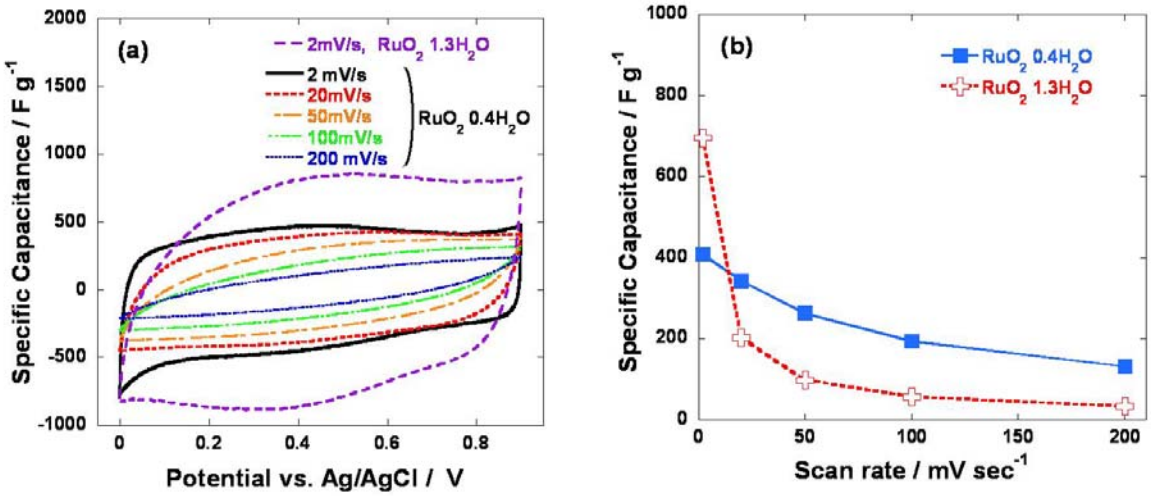

Figure 5.1 (a) Cyclic voltammograms and (b) average specific capacitance obtained for mesoporous crystalline RuO_2•$0.4H_2O$ (**mRO-3**) or amorphous RuO_2•$1.3H_2O$ (**mRO-2**) at different scan rates in 0.5 M sulfuric acid.[179]

VI. Conclusion

Pressing environmental concerns such as clean automotive transport and load leveling for intermittent renewable energy have led to urgent demands for new energy storage system with substantially greater energy densities than ever. The rechargeable Li-oxygen battery is an environment-friendly and highly efficient energy storage system, which can meet such an ever-increasing energy demand since it not only reversibly absorbs and releases oxygen freely available from the air, but it can hold and produce several folds of energy capacity compared with other conventional lithium-ion cells. However, this apparently simple system is now in the early stage of its development and still faces many formidable challenges which should be overcome. Firstly, the formation of the insulating and insoluble reaction product, lithium peroxide requires a highly porous, yet electronically well percolated cathode structure for reasonable performance. Secondly, the inherent high activation energy for the decomposition of lithium peroxide involves the huge anodic overpotential which requires the development of highly efficient catalysts. Thirdly, a proper electrolyte system should be developed which is resistant to both the superoxide attack during the discharge reaction and the highly oxidizing environment during the charge process where both oxygen radicals and catalysts are present. Lastly, the proper protection of the lithium anode is necessary otherwise oxygen radicals in the solvent will react with lithium metal spontaneously, which eventually increases the impedance and more importantly depletes lithium metal from the anode leading to poor cycling performance.

This thesis is primarily focused on the development of highly efficient catalyst systems based on metallic pyrochlore oxide for oxygen reduction and oxygen evolution

reactions for the rechargeable Li-oxygen battery. To this end, highly porous and electrically networked cathode film was manufactured by utilizing common plasticizers (propylene carbonate and dibutyl phthalate) as pore forming agents. The Li-oxygen cell test in two different electrolyte system shows that the reactivity of electrolyte system to superoxide radicals is a key parameter to determine the nature of reaction product. For the LiBOB/PC system, both LIBOB and PC are actively decomposed by superoxide radicals to produce lithium oxalate and lithium carbonate as main discharge products. In the case of the $LiPF_6$/TEGDME system, both salt and solvent are stable, and thus, ideal discharge product, lithium peroxide is obtained. The lead ruthenate and bismuth ruthenate with the extended pyrochlore structure show an excellent catalytic activity by increasing discharge capacity and lowering down the anodic overpotential considerably during charge process in both electrolyte systems. They reduce the decomposition of electrolyte system and the extent of carbon corrosion, which accounts for more efficient cycling. The excellent catalytic activity of these pyrochlores originates from their intrinsic oxygen vacancies, electronic conductivity and many surface active sites afforded by its morphology. The performance of this catalyst was further increased through the gold deposition on the pyrochlore surface resulting in much increased discharge capacity. The pyrochlore coated carbon was proposed as a type of catalyst for the efficient way to reduce the amount of catalyst and enhancing homogenous mixing with other components. The investigation on the lithium peroxide decomposition mechanism indicates that carbon corrosion which occurs at around 4.0 V by lithium peroxide and does not involve oxygen evolution makes further decomposition difficult. However, in the presence of pyrochlore catalyst, Li_2O_2 decomposition reaction by catalyst induces the actual oxygen evolution and can proceed to completion even though carbon corrosion still

occurs. This gives a hint that the generation of nano-porous structure and the homogenous distribution of catalyst over these pores are very important as well as use of highly efficient catalysts for lowering activation overpotentials. Although there are still many obstacles present as listed above for the commercial application of Li-oxygen cell, these hurdles are surmountable in the near future by intensive research and the results shown in this thesis can be a cornerstone for further development. As a future research more rigorous and fundamental research on the identification of the exact oxygen reduction and evolution reaction mechanism will be required to develop better catalyst and electrolyte systems. In addition, protection of the lithium anode will be one of the most important issues for this battery system since it is critically related with long-term cycle life and further application to aqueous systems.

Supercapacitors based on metal oxide are promising energy storage devices for ultrafast charging and discharging with decent energy density over hundreds of thousands of cycles for many commercial electronic devices and power tools. The surface redox nature of these reactions requires the creation of high surface area for better utilization and performance. Hydrous ruthenium dioxide is one of the most attractive supercapacitor materials for its high pseudo-capacitance and metallic character which facilitates fast electron movement. In this thesis, a simple process involving soft liquid crystal templating using cationic surfactant and gentle heat-treatment in the mild temperature was developed to prepare mesoporous ruthenium oxide with a quasi-crystalline wall character, which has a high surface area and controlled water contents in the structure. The electrochemical testing results exhibited a promising performance; high gravimetric capacitance and a good rate capability facilitated by high surface area as well as porous structure. This research can be

further extended to synthesize and explore the characteristics of nano-composite with high surface area carbon (activated carbon, graphene etc.) or other metal oxide to improve the performance, which remains as future research.

References

1 Musson, A. E.; Robinson, E. *Science and Technology in the Industrial Revolution*; University of Manchester at the University Press, 1969.

2 *Understanding and Responding to Climate Change*, United States National Academy of Sciences, 2008.

3 Stirling, I.; Lunn, N. J.; Iacozza, J. *Arctic* **1999**, *52*, 294-306.

4 Hassol, S. J. *Impacts of a Warming Arctic: Artic Climate Impact Assessment, Key Finding 4* **2004**, Cambridge Univeristy Press.

5 Mostafaeipour, A. *Renewable and Sustainable Energy Reviews* **2010**, *14*, 1048-1058.

6 Ouammi, A.; Sacile, R.; Zejli, D.; Mimet, A.; Benchrifa, R. *Energy* **2010**, *35*, 4226-4236.

7 DeCarolis, J. F.; Keith, D. W. *Science* **2001**, *294*, 1000-1003.

8 Roeb, M.; Müller-Steinhagen, H. *Science* **2010**, *329*, 773-774.

9 Shah, A.; Torres, P.; Tscharner, R.; Wyrsch, N.; Keppner, H. *Science* **1999**, *285*, 692-698.

10 Messenger, R. A.; Ventre, J. *Photovoltaic Systems Engineering*; 2nd ed.; CRC Press, 2004.

11 Kennedy, C. E.; Terwilliger, K. *J. Sol. Energy Eng.* **2005**, *127*, 262-269.

12 Fridleifsson, I. B.; Bertani, R.; Huenges, E.; Lund, J. W.; Ragnarsson, A.; Rybach, L. In *IPCC Scoping Meeting on Renewable Energy Sources*; Hohmeyer, O., Trittin, T., Eds. Luebeck, Germany, 2008.

13 Erkan, K.; Holdmann, G.; Benoit, W.; Blackwell, D. *Geothermics* **2008**, *37*, 565-585.

14 Haraden, J. *Energy* **1989**, *14*, 867-873.

15 Bargagli, R.; Cateni, D.; Nelli, L.; Olmastroni, S.; Zagarese, B. *Arch. Environ. Contam. Toxicol.* **1997**, *33*, 172-181.

16 Lamarsh, J. R.; Baratta, A. J. *Introduction to Nuclear Engineering*; 3rd ed.; Prentice Hall, 2001.

17 Prialnik, D. *An Introduction to the Theory of Stellar Structure and Evolution*; Cambridge University, 2000.

18 Enge, H. A.; Wehr, M. R.; Richards, J. A. *Introduction to Atomic Physics*; Addison-Wesley Publishing Company, 1973.

19 Lamarsh, J. R. *Introduction to Nuclear Reactor Theory*; American Nuclear Society, 2002.

20 *Renewable Energy Technology Characterization*, Office of Utility Technologies, Energy Efficiency and Renewable Energy, U.S. Department of Energy and EPRI, 1997.

21 Aricò, A. S.; Bruce, P. G.; Scrosati, B.; Tarascon, J.-M.; Schalkwijk, W. V. *Nature Mater.* **2005**, *4*, 366-377.

22 Bruce, P. G. *Solid State Ion.* **2008**, *179*, 752.

23 Armand, M.; Tarascon, J.-M. *Nature* **2008**, *451*, 652-657.

24 Nagaura, T.; Tozawa, K. *Prog. Batteries Sol. Cells* **1990**, *9*, 209-217.

25 Mizushima, K.; Jones, P. C.; Wiseman, P. J.; Goodenough, J. B. *Mat. Res. Bull.* **1980**, *15*, 783-789.

26 Rao, B. M. L.; Francis, R. W.; Christopher, H. A. *J. Electrochem. Soc.* **1977**, *124*, 1490-1492.

27 Mohri, M.; Yanagisawa, N.; Tajima, Y.; Tanaka, H.; Mitate, T.; Nakajima, S.; Yoshida, M.; Yoshimoto, Y.; Suzuki, T.; Wada, H. *J. Power Sources* **1989**, *26*, 545-551.

28 Tarascon, J.-M.; Guyomard, D. *Electrochimica Acta* **1993**, *38*, 1221-1231.

29 Tarascon, J.-M.; Guyomard, D.; Baker, G. L. *J. Power Sources* **1993**, *44*, 689-700.

30 Jang, D. H.; Shin, Y. J.; Oh, S. M. *J. Electrochem. Soc.* **1996**, *143*, 2204-2211.

31 Jang, D. H.; Oh, S. M. *J. Electrochem. Soc.* **1997**, *144*, 3342-3348.

32 Lu, Z.; MacNeil, D. D.; Dahn, J. R. *Electrochem. Solid State Lett.* **2001**, *4*, A191-A194.

33 Ohzuku, T.; Makimura, Y. *Chem. Lett.* **2001**, 744-745.

34 Ohzuku, T.; Makimura, Y. *Chem. Lett.* **2001**, 642-643.

35 Koyama, Y.; Tanaka, I.; Adachi, H.; Makimura, Y.; Ohzuku, T. *J. Power Sources* **2003**, *119-121*, 644-648.

36 Ohzuku, T.; Takeda, S.; Iwanaga, M. *J. Power Sources* **1999**, *81-82*, 90-94.

37 Gao, Y.; Myrtle, K.; Zhang, M.; Reimers, J. N.; Dahn, J. R. *Phys. Rev. B* **1996**, *54*, 16670-16675.

38 Padhi, A. K.; Nanjundaswamy, K. S.; Goodenough, J. B. *J. Electrochem. Soc.* **1997**, *144*, 1188-1194.

39 Padhi, A. K.; Nanjundaswamy, K. S.; Masquelier, C.; Okada, S.; Goodenough, J. B. *J. Electrochem. Soc.* **1997**, *144*, 1609-1613.

40 Ravet, N.; Chouinard, Y.; Magnan, J. F.; Besner, S.; Gauthier, M.; Armand, M. *J. Power Sources* **2001**, *97-98*, 503-507.

41 Huang, H.; Yin, S.-C.; Kerr, T.; Taylor, N.; Nazar, L. F. *Adv. Mater.* **2002**, *14*, 1525-1528.

42 Herle, P. S.; Ellis, B.; Coombs, N.; Nazar, L. F. *Nature Mater.* **2004**, *3*, 147-152.

43 Barker, J.; Saidi, M. Y.; Swoyer, J. L. *J. Electrochem. Soc.* **2003**, *150*, A1394-A1398.

44 Ramesh, T. N.; Lee, K. T.; Ellis, B.; Nazar, L. F. *Electrochem. Solid State Lett.* **2010**, *13*, A43-A47.

45 Barker, J.; Saidi, M. Y.; Swoyer, J. L. *J. Electrochem. Soc.* **2004**, *151*, A1670-A1677.

46 Nyten, A.; Stjerndahl, M.; Rensmo, H.; Siegbahn, H.; Armand, M.; Gustafsson, T.; Edstroem, K.; Thomas, J. O. *J. Mater. Chem.* **2006**, *16*, 3483-3488.

47 Nyten, A.; Kamali, S.; Haeggstroem, L.; Gustafsson, T.; Thomas, J. O. *J. Mater. Chem.* **2006**, *16*, 2266-2272.

48 Tripathi, R.; Ramesh, T. N.; Ellis, B.; Nazar, L. F. *Angew. Chem. Int. Ed.* **2010**, *49*, 8738-8742.

49 Recham, N.; Chotard, J.-N.; Dupont, L.; Delacourt, C.; Walker, W.; Armand, M.; Tarascon, J.-M. *Nature Mater.* **2010**, *9*, 68-74.

50 Boukamp, B. A.; Lesh, G. C.; Huggins, R. A. *J. Electrochem. Soc.* **1981**, *128*, 725-729.

51 Sharma, R. A.; Seefurth, R. N. *J. Electrochem. Soc.* **1976**, *123*, 1763-1768.

52 Wang, J.; Raistrick, D.; Huggins, R. A. *J. Electrochem. Soc.* **1986**, *133*, 457-460.

53 Ryu, J. H.; Kim, J. W.; Sung, Y.-E.; Oh, S. M. *Electrochem. Solid State Lett.* **2004**, *7*, A306-A309.

54 Beaulieu, L. Y.; Eberman, K. W.; Turner, R. L.; Krause, L. J.; Dahn, J. R. *Electrochem. Solid State Lett.* **2001**, *4*, A137-A140.

55 Graetz, J.; Ahn, C. C.; Yazami, R.; Fultz, B. *Electrochem. Solid State Lett.* **2003**, *6*, A194-A197.

56 Green, M.; Fielder, E.; Scrosati, B.; Wachtler, M.; Moreno, J. S. *Electrochem. Solid State Lett.* **2003**, *6*, A75-A79.

57 Beaulieu, L. Y.; Hewitt, K. C.; Turner, R. L.; Bonakdarpour, A.; Abdo, A. A.; Christensen, L.; Eberman, K. W.; Krause, L. J.; Dahn, J. R. *J. Electrochem. Soc.* **2003**, *150*, A149-A156.

58 Mao, O.; Dahn, J. R. *J. Electrochem. Soc.* **1999**, *146*, 414-422.

59 Mao, O.; Dahn, J. R. *J. Electrochem. Soc.* **1999**, *146*, 423-427.

60 Mao, O.; Dunlap, R. A.; Dahn, J. R. *J. Electrochem. Soc.* **1999**, *146*, 405-413.

61 Yang, J.; Wang, B. F.; Wang, K.; Liu, Y.; Xie, J. Y.; Wen, Z. S. *Electrochem. Solid State Lett.* **2003**, *6*, A154-A156.

62 Kim, I.-S.; Blomgren, G. E.; Kumta, P. N. *Electrochem. Solid State Lett.* **2003**, *6*, A157-A161.

63 Liu, Y.; Hanai, K.; Yang, J.; Imanishi, N.; Hirano, A.; Takeda, Y. *Electrochem. Solid State Lett.* **2004**, *7*, A369-A372.

64 Veeraraghavan, B.; Durairajan, A.; Haran, B.; Popov, B.; Guidotti, R. *J. Electrochem. Soc.* **2002**, *149*, A675-A681.

65 Poizot, P.; Laruelle, S.; Grugeon, S.; Dupont, L.; Tarascon, J.-M. *Nature* **2000**, *407*, 496-499.

66 Jayalakshami, M.; Balasubramanian, K. *Int. J. Electrochem. Sci.* **2008**, *3*, 1196-1217.

67 Zhang, L. L.; Zhou, R.; Zhao, X. S. *J. Mater. Chem.* **2010**, *20*, 5983-5992.

68 Pan, H.; Li, J.; Feng, Y. P. *Nanoscale Res. Lett.* **2010**, *5*, 654-668.

69 Obreja, V. V. N. *Physica E* **2008**, *40*, 2596-2605.

70 Frackowiak, E. *Phys. Chem. Chem. Phys.* **2007**, *9*, 1774-1785.

71 Zhang, S. W.; Chen, G. Z. *Energy Materials* **2008**, *3*, 186-200.

72 Cottineau, T.; Toupin, M.; Delahaye, T.; Brousse, T.; Bélanger, D. *Appl. Phys. A* **2006**, *82*, 599-606.

73 *New Materials and New Configurations for Advanced Electrochemical Capacitors*, The Electrochemical Society, ***Interface***, Spring, 2008.

74 Jones, D. A. *Principles and prevention of corrosion* **1996**, *2nd ed.*, Prentice-Hall, Inc.

75 Allred, A. L. *J. Inorg. Nucl. Chem.* **1961**, *17*, 215-221.

76 Housecroft, C. E.; Sharpe, A. G. *Inorganic Chemistry*; 3rd ed.; Prentice Hall, 2007.

77 Eggert, G. *Gold Bull.* **1995**, *28*, 12-16.

78 Pourbaix, M. *Atlas of Electrochemical Equilibria in Aqueous Solutions* **1974**, *NACE*, Houston.

79 Lynch, S. P. In *The International Conference on Environment-Induced Cracking of Materials*; Shipilov, S. A., Ed. Banff, AB, Canada, 2008; Vol. 1, p 167-177.

80 Shehata, M. T.; Elboujdaini, M.; Revie, R. W. In *The International Symposium on Pipelines for the 21st Century*; Chen, W., Ed. Calgary, AB, Canada, 2005, p 403-417.

81 Hickling, J.; Seifert, H.-P.; Ritter, S. *PowerPlant Chemistry* **2005**, *7*, 4-15.

82 Kondepudi, D.; Prigogine, I. *Modern Thermodynamics: From Heat Engines to Dissipative Structures*; John Wiley & Sons, 1998.

83 Bard, A. J.; Faulkner, L. R. *Electrochemical Methods: Fundamentals and Applications*; John Wiley & Sons, Inc., 2001.

84 Lee, J. S.; Kim, S. T.; Cao, R.; Choi, N. S.; Liu, M.; Lee, K. T.; Cho, J. *Adv. Energy Mater.* **2011**, *1*, 34-50.

85 Neburchilov, V.; Wang, H.; Martin, J. J.; Qu, W. *J. Power Sources* **2010**, *195*, 1271-1291.

86 Blurton, K. F.; Sammells, A. F. *J. Power Sources* **1979**, *4*, 263-279.

87 Li, Q.; Bjerrum, N. J. *J. Power Sources* **2002**, *110*, 1-10.

88 Yeager, E. *J. Mol. Catal.* **1986**, *38*, 5-25.

89 Abraham, K. M. *ECS Transactions* **2008**, *3*, 67-71.

90 Levi, E.; Gofer, Y.; Aurbach, D. *Chem. Mater.* **2010**, *22*, 860-868.

91 Aurbach, D.; Suresh, G. S.; Levi, E.; Mitelman, A.; Mizrahi, O.; Chusid, O.; Brunelli, M. *Adv. Mater.* **2007**, *19*, 4260-4267.

92 Abraham, K. M.; Jiang, Z. *J. Electrochem. Soc.* **1996**, *143*, 1-5.

93 Girishkumar, G.; McCloskey, B.; Luntz, A. C.; Swanson, S.; Wilcke, W. *J. Phys. Chem. Lett.* **2010**, *1*, 2193-2203.

94 Debart, A.; Paterson, A. J.; Bao, J.; Bruce, P. G. *Angew. Chem. Int. Ed.* **2008**, *47*, 4521-4524.

95 Chase_Jr., M. W. *J. Phys. Chem. Ref. Data, Monograph* **1998**, *9*, 1510.

96 Kowalczk, I.; Read, J.; Salomon, M. *Pure & Appl. Chem.* **2007**, *79*, 851-860.

97 Ogasawara, T.; Débart, A.; Holzapfel, M.; Novák, P.; Bruce, P. G. *J. Am. Chem. Soc.* **2006**, *128*, 1390-1393.

98 Jiao, F.; Bruce, P. G. *Adv. Mater.* **2007**, *19*, 657-660.

99 Débart, A.; Bao, J.; Armstrong, G.; Bruce, P. G. *J. Power Sources* **2007**, *174*, 1177-1182.

100 Débart, A.; Bao, J.; Armstrong, G.; Bruce, P. G. *ECS Transactions* **2007**, *3*, 225-232.

101 Laoire, C. O.; Mukerjee, S.; Abraham, K. M. *J. Phys. Chem. C* **2009**, *113*, 20127-20134.

102 Laoire, C. O.; Mukerjee, S.; Abraham, K. M. *J. Phys. Chem. C* **2010**, *114*, 9178-9186.

103 Laoire, C. O.; Mukerjee, S.; Plichta, E. J.; Hendrickson, M. A.; Abraham, K. M. *J. Electrochem. Soc.* **2011**, *158*, A302-A308.

104 Whittingham, M. S. *Science* **1976**, *192*, 1126-1127.

105 He, P.; Wang, Y.; Zhou, H. *Electrochem. Commun.* **2010**, *12*, 1686-1689.

106 Wang, Y.; Zhou, H. *J. Power Sources* **2010**, *195*, 358-361.

107 Knauth, P. *Solid State Ionics* **2009**, *180*, 911-916.

108 Li, H.; Wang, Y.; Na, H.; Liu, H.; Zhou, H. *J. Am. Chem. Soc.* **2009**, *131*, 15098-15099.

109 Zhang, T.; Imanishi, N.; Shimonishi, Y.; Hirano, A.; Takeda, Y.; Yamamoto, O.; Sammes, N. *Chem. Commun.* **2010**, *46*, 1661-1663.

110 Imanishi, N.; Hasegawa, S.; Zhang, T.; Hirano, A.; Takeda, Y.; Yamamoto, O. *J. Power Sources* **2008**, *185*, 1392-1397.

111 Read, J. *J. Electrochem. Soc.* **2002**, *149*, A1190-A1195.

112 Read, J.; Mutolo, K.; Ervin, M.; Behl, W.; Wolfenstine, J.; Driedger, A.; Foster, D. *J. Electrochem. Soc.* **2003**, *150*, A1351-A1356.

113 Mizuno, F.; Nakanishi, S.; Kotani, Y.; Yokoishi, S.; Iba, H. *Electrochemistry* **2010**, *78*, 403-405.

114 Giordani, V.; Freunberger, S. A.; Bruce, P. G.; Tarascon, J.-M.; Larcher, D. *Electrochem. Solid State Lett.* **2010**, *13*, A180-A183.

115 Freunberger, S. A.; Hardwick, L.; Peng, Z.; Giordani, V.; Chen, Y.; Maire, P.; Novák, P.; Tarascon, J.-M.; Bruce, P. G. In *The 15th International Meeting on Lithium Batteries* Montréal, Canada, 2010.

116 Zhang, J.; Xu, W.; Liu, W. *J. Power Sources* **2010**, *195*, 7438-7444.

117 Greenwood, N. N.; Earnshaw, A. *Chemistry of the Elements*; 2nd ed.; A Butterworth-Heinemann, 1997.

118 Jaunsen, J. R. *The Behavior and Capabilities of Lithium Hydroxide Carbon Dioxide Scrubbers in a Deep Sea Environment*, United States Naval Academy, 1989.

119 Lu, Y. C.; Gasteiger, H. A.; Parent, M. C.; Chiloyan, V.; Shao-Horn, Y. *Electrochem. Solid State Lett.* **2010**, *13*, A69-A72.

120 Lu, Y.-C.; Gasteiger, H. A.; Crumlin, E.; McGuire_Jr., R.; Shao-Horn, Y. *J. Electrochem. Soc.* **2010**, *157*, A1016-A1025.

121 Débart, A.; Paterson, A. J.; Bao, J.; Bruce, P. G. *Angew. Chem. Int. Ed.* **2008**, *47*, 4521-4524.

122 Cheng, F.; Shen, J.; Peng, B.; Pan, Y.; Tao, Z.; Chen, J. *Nature Chem.* **2011**, *3*, 79-84.

123 Binotto, G.; Larcher, D.; Prakash, A. S.; Urbina, R. H.; Hegde, M. S.; Tarascon, J.-M. *Chem. Mater.* **2007**, *19*, 3032-3040.

124 Ngala, J. K.; Alia, S.; Dobley, A.; Crisostomo, V. M. B.; Suib, S. L. *Chem. Mater.* **2007**, *19*, 229-234.

125 Pearson, R. G. *J. Am. Chem. Soc.* **1963**, *85*, 3533-3539.

126 Pearson, R. G. *J. Chem. Educ.* **1968**, *45*, 581-587.

127 Pearson, R. G. *J. Chem. Educ.* **1968**, *45*, 643-648.

128 Gutmann, V. *Coord. Chem. Rev.* **1976**, *18*, 225-255.

129 Larminie, J.; Dicks, A. *Fuel Cell Systems Explained*; 2nd ed.; John Wiley & Sons Ltd., 2003.

130 Gasteiger, H. A.; Baker, D. R.; Carter, R. N.; Cu, W.; Liu, Y.; Wagner, F. T.; Yu, P. T. *Electrocatalysis and Catalyst Degradation Challenges in Proton Exchange Membrane Fuel Cells*; Wiley-VCH Verlag GmbH & Co. KGaA, Weinheim.

131 Stein, A.; Wang, Z.; Fierke, M. A. *Adv. Mater.* **2009**, *21*, 265-293.

132 Karousis, N.; Tagmatarchis, N.; Tasis, D. *Chem. Rev.* **2010**, *110*, 5366-5397.

133 Boehm, H. P. *Carbon* **2002**, *40*, 145-149.

134 Fuente, E.; Menéndez, J. A.; Suárez, D.; Montes-Morán, M. A. *Langmuir* **2003**, *19*, 3505-3511.

135 Subramanian, M. A.; Aravamudan, G.; Rao, G. v. S. *Prog. Solid St. Chem.* **1983**, *15*, 55-143.

136 Mindat.org, Pyrochlore Group: Pyrochlore Group mineral information and data, http://www.mindat.org/min-3316.html

137 Goodenough, J. B.; Manoharan, R.; Paranthaman, M. *J. Am. Chem. Soc.* **1990**, *112*, 2076-2082.

138 Horowitz, H. S.; Longo, J. M.; Lewandowski, J. T. *Mat. Res. Bull.* **1981**, *16*, 489-496.

139 Horowitz, H. S.; Longo, J. M.; Horowitz, H. H. *J. Electrochem. Soc.* **1983**, *130*, 1851-1859.

140 Beyerlein, R. A.; Horowitz, H. S.; Longo, J. M.; Leonowicz, M. E. *J. Solid State Chem.* **1984**, *51*, 253-265.

141 Beyerlein, R. A.; Horowitz, H. S.; Longo, J. M. *J. Solid State Chem.* **1988**, *72*, 2-13.

142 Akazawa, T.; Inaguma, Y.; Katsumata, T.; Hiraki, K.; Takahashi, T. *J. Cryst. Growth* **2004**, *271*, 445-449.

143 Bang, H. J.; Lu, W.; Cao, F.; Prakash, J. *Electrochem. Commun.* **2000**, *2*, 653-657.

144 Cao, F.; Prakash, J. *J. Power Sources* **2001**, *92*, 40-44.

145 Takeda, T.; Kanno, R.; Kawamoto, Y.; Takeda, Y. *J. Electrochem. Soc.* **2000**, *147*, 1730-1733.

146 Esposito, V.; Traversa, E.; Wachsman, E. D. *J. Electrochem. Soc.* **2005**, *152*, A200-.

147 Raghuveer, V.; Viswanathan, B. *J. Mater. Sci.* **2005**, *40*, 6249-6255.

148 Prakash, J.; Tryk, D.; Yeager, E. *J. Power Sources* **1990**, *29*, 413-422.

149 Fang, Y.-H.; Liu, Z.-P. *J. Am. Chem. Soc.* **2010**, *2010*, 18214-18222.

150 Xu, K. *Chem. Rev.* **2004**, *104*, 4303-4417.

151 Freunberger, S. A.; Chen, Y.; Peng, Z.; Griffin, J. M.; Hardwick, L. J.; Bardé, F.; Novák, P.; Bruce, P. G. *J. Am. Chem. Soc.* **2011**, *133*, 8040-8047.

152 Campbell, S. A.; Bowes, C.; McMillan, R. S. *J. Electroanal. Chem.* **1990**, *284*, 195-204.

153 Castellan, G. W. *Physical Chemistry*; 3rd Ed. ed.; Addison Wesley Publishing Company, 1983.

154 McQuarrie, D. A.; Simon, J. D. *Physical Chemistry: A Molecular Approach*; University Science Books, 1997.

155 Halliday, D.; Resnick, R.; Walker, J. *Fundamentals of Physics*; 8th ed.; Wiley, 2007.

156 Simon, P.; Gogotsi, Y. *Nature Mater.* **2008**, *7*, 845-854.

157 Zheng, J. P.; Jow, T. R. *J. Electrochem. Soc.* **1995**, *142*, L6-L8.

158 Zheng, J. P.; Cygan, P. J.; Jow, T. R. *J. Electrochem. Soc.* **1995**, *142*, 2699-2703.

159 Choi, D.; Blomgren, G. E.; Kumta, P. N. *Adv. Mater.* **2006**, *18*, 1178-1182.

160 Bi, R.-R.; Wu, X.-L.; Cao, F.-F.; Jiang, L.-Y.; Guo, Y.-G.; Wan, L.-J. *J. Phys. Chem. C* **2010**, *114*.

161 Fan, L.-Z.; Hu, Y.-S.; Maier, J.; Adelheim, P.; Smarsly, B.; Antonietti, M. *Adv. Func. Mater.* **2007**, *17*, 3083-3087.

162 Naoi, K.; Ishimoto, S.; Ogihara, N.; Nakagawa, Y.; Hatta, S. *J. Electrochem. Soc.* **2009**, *156*, A52-A59.

163 Jenkins, R.; Snyder, R. L. *Introduction to X-ray Powder Diffractometry*; John Wiley & Sons, Inc., 1996; Vol. 138.

164 Bragg, W. L. *Proceedings of the Cambridge Philosophical Society* **1913**, *17*, 43-57.

165 West, A. R. *Basic Solid State Chemistry*; John Wiley & Sons Ltd., 1999.

166 Klug, H. P.; Alexander, L. E. *X-ray Diffraction Procedures for Polycrystalline and Amorphous Materials*; 2nd ed.; John Wiley & Sons, Inc., 1974.

167 Warren, B. E. *X-Ray Diffraction*; General Publishing Company, Ltd.: North York, ON, 1990.

168 Broglie, L. d. Recherches sur la théorie des quanta, Thesis, Paris, 1924.

169 Sing, K. S. W.; Everett, D. H.; Haul, R. A. W.; Moscou, L.; Pierotti, R. A.; Rouquerol, J.; Siemieniewska, T. *Pure & Appl. Chem.* **1985**, *57*, 603-919.

170 Langmuir, I. *J. Am. Chem. Soc.* **1918**, *40*, 1361-1403.

171 Brunauer, S.; Emmett, P. H.; Teller, E. *J. Am. Chem. Soc.* **1938**, *60*, 309-319.

172 Rouquerol, J.; Avnir, D.; Fairbridge, C. W.; Everett, D. H.; Haynes, J. H.; Pernicone, N.; Ramsay, J. D. F.; Sing, K. S. W.; Unger, K. K. *Pure & Appl. Chem.* **1994**, *66*, 1739-1758.

173 deBoer, J. H.; Lippens, B. C.; Linsen, B. G.; Broekhoff, J. C. P.; Heuvel, A. v. d.; Osinga, T. V. *J. Colloid Interface Sci.* **1966**, *21*, 405-414.

174 Halsey, G. *J. Chem. Phys.* **1948**, *16*, 931-937.

175 Barrett, E. P.; Joyner, L. G.; Halenda, P. P. *J. Am. Chem. Soc.* **1951**, *73*, 373-380.

176 Thommes, M. *Physical Adsorption Characterization of Ordered and Amorphous Materials*; Imperial College Press, 2004.

177 Bonanos, N.; Macdonald, J. R.; Butler, E. P.; McKubre, M. C. H.; Franceschetti, D. R.; Raistrick, I. D.; Johnson, W. B.; Steele, B. C. H.; Macdonald, D. D.; Worrell, W. L.; Barsoukov, E.; Bonanos, N.; Conway, B.; Goossens, A.; Niklasson, G. A.; Sayers, B.; Wagner, N. *Impedance Spectroscopy: Theory, Experiment, and Applications*; 2nd ed.; John Wiley & Sons, Inc., 2005.

178 Macdonald, D. D.; Sikora, E.; Engelhardt, G. *Electrochimica Acta* **1998**, *43*, 87-107.

179 Oh, S. H.; Nazar, L. F. *J. Mater. Chem.* **2010**, *20*, 3834-3839.

180 Kresge, C. T.; Leonowicz, M. E.; Roth, W. J.; Vartuli, J. C.; Beck, J. S. *Nature* **1992**, *139*, 710-712.

181 Huo, Q.; Margolese, D. I.; Ciesla, U.; Feng, P.; Gier, T. E.; Sieger, P.; Leon, R.; Petroff, P. M.; Schüth, F.; Stucky, G. D. *Nature* **1994**, *368*, 317-321.

182 Beck, J. S.; Vartuli, J. C.; Roth, W. J.; Leonowicz, M. E.; Kresge, C. T.; Schmitt, K. D.; Chu, C. T.-W.; Olson, D. H.; Sheppard, E. W.; McCullen, S. B.; Higgins, J. B.; Schienker, J. L. *J. Am. Chem. Soc.* **1992**, *114*, 10834-10843.

183 Kim, I.-H.; Kim, K.-B. *J. Electrochem. Soc.* **2004**, *151*, E7-E13.

184 Kim, I.-H.; Kim, K.-B. *J. Electrochem. Soc.* **2006**, *153*, A383-A389.

185 Bagshaw, S. A.; Prouzet, E.; Pinnavaia, T. J. *Science* **1995**, *269*, 1242-1244.

186 Kim, S.-S.; Pauly, T. R.; Pinnavaia, T. J. *Chem. Commun.* **2000**, 835-836.

187 Lee, J.; Orilall, M. C.; Warren, S. C.; Kamperman, M.; Disalvo, F. J.; Wiesner, U. *Nature Mater.* **2008**, *7*, 222-228.

188 Park, I.; Pinnavaia, T. J. *Micropor. Mesopor. Mater.* **2009**, *118*, 239-244.

189 Behrens, P. *Angew. Chem. Int. Ed.* **1996**, *35*, 515-518.

190 Sayari, A.; Liu, P. *Micropor. Mesopor. Mater.* **1997**, *12*, 149-177.

191 Emel'yanov, V. A.; Kabin, E. V.; Baidina, I. A. *J. Struct. Chem.* **2009**, *50*, 577-581.

192 Drouet, C.; Alphonse, P.; Rousset, A. *Phys. Chem. Chem. Phys.* **2001**, *3*, 3826-3830.

193 Choi, M.; Cho, H. S.; Srivastava, R.; Venkatesan, C.; Choi, D.-H.; Ryoo, R. *Nature Mater.* **2006**, *5*, 718-723.

194 Fan, W.; Snyder, M. A.; Kumar, S.; Lee, P.; Yoo, W. C.; McCormick, A. V.; Penn, R. L.; Stein, A.; Tsapatsis, M. *Nature Mater.* **2008**, *7*, 984-991.

195 Lai, X.; Li, X.; Geng, W.; Tu, J.; Li, J.; Qiu, S. *Angew. Chem. Int. Ed.* **2007**, *46*, 738-741.

196 Boissière, C.; Grosso, D.; Prouzet, E. *Inorganic Nanomaterials Synthesis Using Liquid Crystals*; Wiley, 2008.

197 Cao, M.; Hu, C.; Peng, G.; Qi, Y.; Wang, E. *J. Am. Chem. Soc.* **2003**, *125*, 4982-4983.

198 Emons, T. T.; Li, J.; Nazar, L. F. *J. Am. Chem. Soc.* **2002**, *124*, 8516-8517.

199 Aprile, C.; Teruel, L.; Alvaro, M.; Garcia, H. *J. Am. Chem. Soc.* **2009**, *131*, 1342-1343.

200 Vinke, P.; Euk, M. v. d.; Verbree, M.; Voskamp, A. F. *Carbon* **1994**, *32*, 675-686.

201 Boaro, M.; Vicario, M.; Llorca, J.; Leitenburg, C. d.; Dolcetti, G. *Appl. Catal. B* **2009**, *88*, 272-282.

202 Gao, Y.; Wang, Z.; Wan, J.; Zou, G.; Qian, Y. *J. Cryst. Growth* **2005**, *279*, 415-419.

203 Webmineral.com, Cryptomelane Mineral Data, http://webmineral.com/data/Cryptomelane.shtml

204 Richard, M. N.; Koetschau, I.; Dahn, J. R. *J. Electrochem. Soc.* **1997**, *144*, 554-557.

205 Tarascon, J.-M.; Gozdz, A. S.; Schmutz, C.; Shokoohi, F.; Warren, P. C. *Solid State Ionics* **1996**, *86-88*, 49-54.

206 Amatucci, G. G.; Tarascon, J.-M.; Klein, L. C. *J. Electrochem. Soc.* **1996**, *143*, 1114-1123.

207 Gozdz, A. S.; Schmutz, C. N.; Tarascon, J.-M.; Warren, P. C. U.S. Pat. 5,478,668 **1995**

208 Föppl, V. H. *Zeitschrift für anorganische und allgemeine Chemie* **1957**, *291*, 12-50.

209 Cota, L. G.; Mora, P. d. l. *Acta Crystallogr. B* **2005**, *61*, 133.

210 Wu, H. Y.; Zhang, H.; Cheng, X. L.; Cai, L. C. *Physics Letters A* **2006**, *360*, 352-356.

211 Delmer, O.; Balaya, P.; Kienle, L.; Maier, J. *Adv. Mater.* **2008**, *20*, 501-505.

212 Hu, Y.-S.; Guo, Y.-G.; Sigle, W.; Hore, S.; Balaya, P.; Maier, J. *Nature Mater.* **2006**, *5*, 713-717.

213 Martos, M.; Morales, J.; Sánchez, L. *Electrochimica Acta* **2003**, *48*, 615-621.

214 Chelali, N.; Zerroual, L.; Hammouche, A.; Kahoul, A.; Guitton, J. *Solid State Ion.* **1996**, *91*, 289-294.

215 Murphy, D. W.; Salvo, F. J. D.; Carides, J. N.; Waszczak, J. V. *Mat. Res. Bull.* **1978**, *13*, 1395-1402.

216 Aurbach, D.; Zinigrad, E.; Cohen, Y.; Teller, H. *Solid State Ion.* **2002**, *148*, 405-416.

217 Winter, M.; Besenhard, J. O.; Spahr, M. E.; Novák, P. *Adv. Mater.* **1998**, *10*, 725-763.

218 Nasirzadeh, K.; Neueder, R.; Kunz, W. *J. Chem. Eng. Data* **2005**, *50*, 26-28.

219 Xu, K.; Zhang, S. S.; Lee, U.; Allen, J. L.; Jow, T. R. *J. Power Sources* **2005**, *146*, 79-85.

220 Xu, K.; Zhang, S.; Poese, B. A.; Jow, T. R. *Electrochem. Solid State Lett.* **2002**, *5*, A259-A262.

221 Lu, Y. C.; Xu, Z.; Gasteiger, H. A.; Chen, S.; Hamad-Schifferli, K.; Shao-Horn, Y. *J. Am. Chem. Soc.* **2010**, *132*, 12170-12171.

222 Gal, O.; Baugh, P. J.; Phillips, G. O. *Int.J. Radiat. Phys. Chem* **1972**, *4*, 159-169.

223 Shippey, T. A. *J. Mol. Struct.* **1980**, *67*, 223-233.

224 Zinigrad, E.; Larush-Asraf, L.; Salitra, G.; Sprecher, M.; Aurbach, D. *Thermochimica Acta* **2007**, *457*, 64-69.

225 *CRC Handbook of Chemistry and Physics*; 87th ed.; Taylor and Francis: Boca Raton. FL., 2007.

226 Thackeray, M. M.; Shao-Horn, Y.; Kahaian, A. J.; Kepler, K. D.; Skinner, E.; Vaughey, J. T.; Hackney, S. A. *Electrochem. Solid State Lett.* **1998**, *1*, 7-9.

227 Rophael, M. W.; Petro, N. S.; Khalil, L. B. *J. Power Sources* **1988**, *22*, 149-161.

228 Zhou, H.; Shen, Y. E.; Wang, J. Y.; Chen, X.; O'Young, C.-L.; Suib, S. L. *J. Catal.* **1998**, *176*, 321-328.

229 Roy, C. B. *J. Catal.* **1968**, *12*, 129-133.

230 Cahill, A. E.; Allen, E.; Taube, H. *J. Am. Chem. Soc.* **1952**, *74*, 2312-2318.

231 Imagawa, H.; Nakano, H.; Azuma, H. U.S. Pat Pub. No. 2008/0176124 A1 **2008**

232 Thebulliondesk.com, http://www.thebulliondesk.com/?Tab=1&site=1&lang=EN

233 Minormetals.com, http://www.minormetals.com/

234 George, M. W. *2006 Minerals Yearbook: Platinum-Group Metals*, United States Geological Survey USGS, 2006.

235 Bush, R. P. *Platinum Metals Rev.* **1991**, *35*, 202-208.

236 Kolarik, Z.; Renard, E. V. *Platinum Metals Rev.* **2003**, *47*, 74-87.

237 Morrison, S. R. *Electrochemistry at semiconductor and oxidized metal electrodes*; Plenum Press, 1980.

238 Eswaran, M.; Munichandraiah, N.; Scanlon, L. G. *Electrochem. Solid State Lett.* **2010**, *13*, A121-A124.

239 Shibata, H.; Ogura, T.; Mukai, T.; Ohkubo, T.; Sakai, H.; Abe, M. *J. Am. Chem. Soc.* **2005**, *127*, 16396-16397.

240 Deng, J.; Zhang, L.; Dai, H.; Au, C.-T. *Appl. Catal. A* **2009**, *352*, 43-49.

241 Luo, J.-Y.; Wang, Y.-G.; H. -M. Xiong, Y.-Y. X. *Chem. Mater.* **2007**, *19*, 4791-4795.

242 Wang, D.; Choi, D.; Yang, Z.; Viswanathan, V. V.; Nie, Z.; Wang, C.; Song, Y.; Zhang, J.-G.; Liu, J. *Chem. Mater.* **2008**, *20*, 3435-3442.

243 Cui, X.; He, Q.; Cui, F.; Zhao, J.; Li, L.; Chen, H.; Shi, J. *Dalton Trans.* **2009**, 3395-3402.

244 Wang, L.; Li, D.; Wang, R.; He, Y.; Qi, Q.; Wang, Y.; Zhang, T. *Sen. Actuator B* **2008**, *B133*, 622-627.

245 Shen, W.; Shi, J.; Chen, H.; Gu, J.; Zhu, Y.; Dong, X. *Chem. Lett.* **2005**, *34*, 390-391.

246 Osaka, T.; Datta, M. *Energy Storage Systems for Electronics*; Gordon and Breach Science Publisher, 2000.

247 Jiao, F.; Harrison, A.; Junmas, J.; Chadwick, A. V.; Kockelmann, W.; Bruce, P. G. *J. Am. Chem. Soc.* **2006**, *128*, 5468-5474.

248 Shaju, K. M.; Jiao, F.; Débart, A.; bruce, P. G. *Phys. Chem. Chem. Phys.* **2007**, *9*, 1837-1842.

249 Jiao, F.; Hill, A. H.; Harrison, A.; Berko, A.; Chadwick, A. V.; Bruce, P. G. *J. Am. Chem. Soc.* **2008**, *130*, 5262-5266.

250 Yun, H.-S.; Zhou, H.; Homma, I. *Chem. Commun.* **2004**, 2836-2837.

251 Li, D.; Zhou, H.; Honma, I. *Nature Mater.* **2004**, *3*, 65-72.

252 Lee, W.; Mane, R. S.; Todkar, V. V.; Lee, S.; Egorava, O.; Chae, W.-S.; Han, S.-H. *Electrochem. Solid State Lett.* **2007**, *10*, A225-A227.

253 Long, J.; Swider, K.; Merzbacher, C.; Rolison, D. *Langmuir* **1999**, *15*, 780-785.

254 Sassoye, C.; Laberty, C.; Khanh, H. L.; Cassaignon, S.; Boissière, C.; Antonietti, M.; Sanchez, C. *Adv. Func. Mater.* **2009**, *19*, 1922-1929.